Kinetic Effects of Heat Stress on Olfaction: A Thermodynamic Evaluation of Electrical Responses to Odorants in Olfactory Epithelia

by

Samantha Lynne Hagerty

A dissertation submitted to the Graduate Faculty of
Auburn University
in partial fulfillment of
the requirements for the Degree of
Doctor of Philosophy

Auburn, Alabama
May 08, 2018

Key words: olfaction, electroolfactogram, heat stress, olfactory receptors

Approved by:

Vitaly J. Vodyanoy, Chair, Alumni Professor of Anatomy, Physiology, & Pharmacology
Edward E. Morrison, Department Head, Professor of Anatomy, Physiology, & Pharmacology
Iryna B. Sorokulova, Professor of Anatomy, Physiology, & Pharmacology
Robert L. Judd, Professor of Anatomy, Physiology, & Pharmacology

Abstract

Detection dogs are exposed to some of the most extreme environmental conditions in the world while simultaneously expected to maintain maximal olfactory function. Sometimes these conditions exceed their thermoregulatory capabilities and cause permanent damage, or even death. Extreme heat stress has been shown to adversely affect the gastrointestinal tract, causing damage to the mucosa protecting the internal environment of the body from harmful bacteria and endotoxins. Dysfunction of this protective barrier increases intestinal permeability and diffusion of toxic bacterial components from the gut lumen into the blood. Growing evidence of olfactory receptor expression in various non-sensory organs has expanded our scope of olfactory system involvement beyond the nasal cavity. Additionally, these ectopic olfactory receptors have been shown to interact with microbial by-products, even playing important regulatory roles other than simply the sense of smell. Given the extensive interactions between the GI tract and central nervous system function, as well as the direct exposure of olfactory sensory neurons to the external environment, the adverse effects of heat stress on intestinal physiology may also occur within the olfactory system. Olfaction may be one of the many physiological functions affected by heat stress. Our goal is to investigate the effects of heat stress on olfactory function, including the effects of temperature on zinc nanoparticles, which we previously demonstrated to have strong enhancement of

olfactory neuronal responses to odorant stimulation and are thought to play an important role in the initial events of olfaction.

In this work, we examine the effects of both environmental and metabolic heat stress on the kinetic properties of rat olfactory sensory neurons *ex vivo* using electroolfactogram (EOG) recordings from dissected olfactory epithelium (OE). The electrical activity of olfactory epithelia in response to odorant stimulation was assessed. Exposing rats to heat stress conditions resulted in a kinetic shift in signal activation and deactivation, showing faster rise and decay response times. Exposing olfactory epithelia dissected from non-stressed rats to various temperatures resulted in a change in EOG response stability, amplitude, and calculated thermodynamic parameters with increasing temperatures. Additionally, zinc nanoparticle preparations exposed to high temperatures and long-term storage showed increased levels of oxidization, which inhibited their ability to enhance olfactory responses. A preservation technique using a polyethylene glycol coating (PEGylated) nanoparticles resulted in a resistance to temperature-induced oxidation and conserved the enhancement effects on olfactory function.

Several conclusions were drawn regarding thermal challenge to olfactory epithelium. Thermodynamic properties at the epithelial surface were extrapolated from kinetic calculations, and processes associated with EOG responses are entropy driven. The large entropy values calculated from these experiments indicated a decrease in molecular rotational and translational degrees of freedom of the olfactory receptor binding pocket – potentially allowing easier access for ligand binding. Secondly,

activation energy and enthalpy were found to be small with respect to entropy contribution and free energy. This suggests that the transition barrier is lowered through entropic and enthalpic contributions, referred to as “activation-less” binding of odorants to the olfactory receptor.

Acknowledgements

The author would like to thank all advisors, colleagues, friends, and family who made this work possible through their direct involvement within the laboratory and classroom, as well as through advice, support, and guidance. Specifically, Dr. Vitaly Vodyanoy, Dr. Edward E. Morrison, Dr. Iryna B. Sorokulova, Dr. Robert Judd, Mr. Oleg Pustovyy, and Ms. Ludmila Globa, Dr. Melissa Singletary, Mr. Alex Giblot Ducray.

Table of Contents

List of Tables

List of Figures

Chapter 1 – Introduction

Physiological stressors are conditions, presented internally or externally, that challenge the overall homeostatic environment of an organism. Stressors can be psychological, metabolic, or physical in nature. Environmental conditions such as temperature, humidity, pollutant exposure, ultraviolet exposure, etc. are examples of physical stressors. Temperature-related stress is a significant challenge to both human and animal health. Thermoregulatory mechanisms allow humans to withstand significant variations in environmental temperatures, but relatively small increases in internal temperature can lead to central nervous system dysfunction, heatstroke, and even death (Leon and Helwig 2010). There are approximately 200 heat stress-related deaths per year in the United States. Severe or chronic heat exposure can be life-threatening even to young, physically fit individuals, especially when coupled with strenuous exercise. The majority of human heat stroke cases, however, involve very young children or elderly adults. The ultimate cause of mortality is multi-organ system failure due to systemic inflammatory responses.

Thermoregulatory challenges are not unique to humans. Working dogs, especially in the military and police force, are exposed to some of the most extreme environmental conditions in the world. Sometimes these conditions exceed their thermoregulatory capabilities and cause permanent damage or death. Increasing efforts are directed towards preventing heat stroke related complications (Yokota, Berglund et al. 2014) by designing temperature-controlled kennels for the animals to be housed and limiting their exposure to extreme environmental temperatures. The coupling of strenuous metabolic activity and

extreme temperatures present a unique problem. Detection dogs hold tremendously valued jobs, using their specialized olfactory machinery to seek out dangerous substances. While preventative measures and utmost care is taken to protect the physical health of dogs in the workforce (Toffoli and Rolfe 2006), the question is also raised regarding whether exposure to chronically high temperatures can impact their ability to do what they are trained to do.

While thermal stress has been shown to result in inflammatory responses that impact gastrointestinal function and dysregulation, we ask whether these complications extend to olfactory function. Environmental conditions such as temperature and humidity can affect the physical nature of odorants, their concentration in the inspired air, and their ability to interact with olfactory receptors (Nagappan, Subramaniam et al. 2017). Moreover, given the extensive bidirectional interactions between the gut and central nervous system, and the fact that olfactory sensory neurons are subsets of the central nervous system, it is possible that systemic interactions related to heat stress responses could affect the olfactory system. This work aims to evaluate the effects of environmental and metabolic heat stress on olfactory function. Using a rat model and varying models of thermal change, we will analyze electrical responses of olfactory epithelia to odorant stimulation.

Chapter 2 – Literature Review

2.1. Anatomy of the Vertebrate Olfactory System

Olfaction is the most evolutionarily conserved sensory system among higher eukaryotic organisms. From anatomical structure and organization to signal pathways, there is little divergence between vertebrate species other than respective proportions of the genomic repertoire dedicated to certain olfactory cellular machinery (Hildebrand and Shepherd 1997). In most animals, two functionally separate olfactory systems have developed. **Figure 1** is a depiction of the spatial organization of these two distinct systems in rats. The first, or primary, olfactory region is called the main olfactory system. The specialized main olfactory epithelia (MOE) is responsible for the detection of volatile chemical odorants within the environment for the purposes of food acquisition, detection of dangers and predators, and general smell perception.

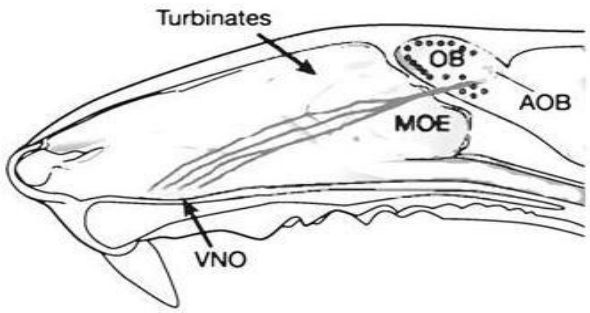

Figure 1. Anatomical Organization. *A schematic of the sagittal view of the rat head showing the spatial organization of the main and accessory olfactory systems (Firestein 2001).*

An accessory olfactory system has also developed in many species dedicated to interactions related to reproduction. This accessory olfactory system is collectively called the vomeronasal organ (VNO), which consists of its own specialized epithelium and sensory neurons that project to the accessory olfactory bulb (AOB) and is responsible for the detection and processing of

pheromone molecules in the environment that carry information about reproductive state and availability between opposite sexes (Firestein 2001). Both main and accessory olfactory systems consist of similar chemical odor processing and signal transduction machinery. The focus of this work will be on the main olfactory system in vertebrate species.

2.1.1. Olfactory Epithelium

The nasal cavity houses both respiratory and main olfactory epithelia, which are morphologically, spatially, and functionally distinct from one another. Olfactory epithelium, classified as ciliated pseudostratified columnar shaped, is a sensory neuroepithelium covering the caudal region of the nasal septum, responsible for the detection and processing of chemical odorants (Morrison and Costanzo 1990). There are three major cell types and a few glandular characteristics unique to the olfactory epithelia of vertebrate species, shown in **figure 2**. Bowman's glands are specific to the olfactory epithelium and produce the mucus layer that lines the surface. Volatile odorants entering the airway from inspired air are trapped within the mucus layer, and odorant binding proteins (OBP) are responsible for directing these odorants to the receptors for recognition and signal transduction. Along with the capture of odorants, this mucus layer plays a protective role by trapping and destroying potentially harmful foreign material, as it houses a number of different

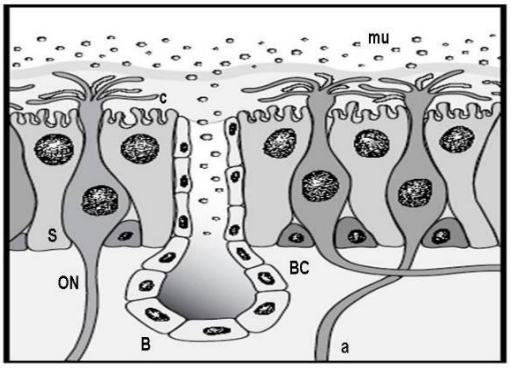

Figure 2. Olfactory Epithelium. *ON-olfactory neuron, S-supporting cell, BC-basal stem cell, B-Bowman's gland, MU-mucus layer, A-axon. (Drawing courtesy of Dr. Vodyanoy).*

antimicrobial immune peptides. The three main cell types include olfactory sensory neurons (OSN), supporting cells, and basal cells. Basal cells are relatively simple structures, histologically. They are characteristically small and round to cuboidal-shaped cells that sit just along the basement membrane of the epithelium (Morrison and Costanzo 1990). Their role is very important, as they are responsible for the cyclic regeneration of olfactory sensory neurons, the primary sensing cells, that are damaged or dead. OSNs are bipolar neurons with a single axonal end extending basally, and a dendritic end that extends apically towards the nasal cavity airway. Axons from OSNs extend through the basement membrane and cribiform plate of the ethmoid bone, which is a bony barrier separating the nasal cavity from the cranium. There are small openings throughout the cribiform plate where axonal processes from many olfactory neurons form fascicle groupings, transmitting sensory information collected at the epithelium to the secondary neurons in the olfactory bulb and further into cortical regions of the brain (Morrison and Costanzo 1990). The single dendritic pole of OSNs extends through the epithelial surface, ending in a knob-like swelling which consists of many ciliary projections. Embedded in the membrane of these cilia are the functional unit of olfactory signal transduction, olfactory receptors (**figure 3**), which will later be discussed in more detail. Each olfactory sensory neuron expresses only one of about 1000 olfactory receptors on the ciliary

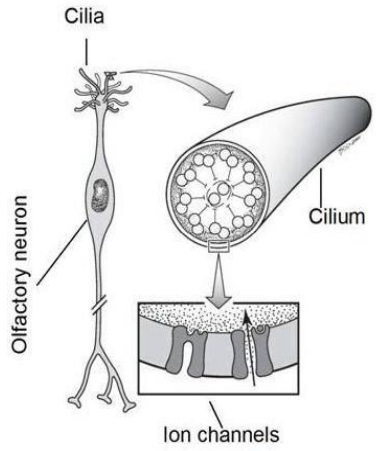

Figure 3. Bipolar Olfactory Sensory Neuron. *A single dendrite ending in a ciliary knob extends apically to the surface of epithelium. Olfactory receptors embedded in the cilia are the site of odorant contact and signal transduction cascade. A single axon extends through the epithelial basement to the olfactory bulb (Illustration courtesy of Dr. Vodyanoy)*

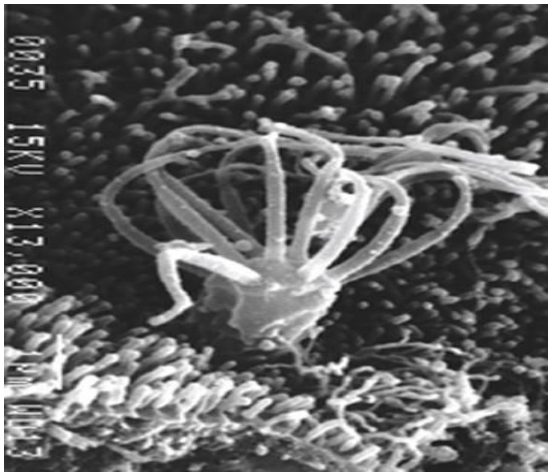

Figure 4. Cilia Extending from Dendritic Knob of Olfactory Neuron. *OSN ciliary projections above epithelial surface, surrounded by supporting cells. (Electron Micrograph courtesy of Dr. Morrison – Morrison & Costanzo 1990).*

processes (Buck and Axel 1991; Mombaerts 2004). Surrounding OSNs in epithelium depicted in the electron micrograph in **figure 4** are supporting cells, which are tall columnar shaped cells spanning the length of the epithelium that are mainly responsible for structural integrity and providing insulation to the sensory neurons. Olfactory neurons are also defined as "true neurons", meaning they are a direct connection between the external environment and the central nervous system, as they sit just above the epithelial surface and project directly to the brain. Given their external exposure to many environmental conditions, pathogens, and physical trauma, olfactory neurons are subject damage. Similarly, since these neurons extend directly to the brain, there is high potential for the entrance of dangerous or foreign material across the blood brain barrier that could cause serious damage and disease. For that reason, there must be sufficient regenerative properties for damaged neurons as well as defense mechanisms in place to protect the brain and body. As mentioned previously, the basal cells are regenerative in nature, and increase mitotic activity to replace damaged olfactory sensory neurons. In one study, experimental lesion of axonal projections to the olfactory bulb in rats resulted in an initial decrease in olfactory neurons present and a subsequent upregulation of mitotic figures in the basal region in the olfactory epithelium (Morrison and Costanzo 1989). Olfactory marker protein (OMP) is a molecular marker of mature

and fully differentiated olfactory neurons. Though its specific role and mechanism of action is not entirely clear, animals lacking OMP through genetic manipulation have demonstrated slower odorant response kinetics and reduced odorant sensitivity (Buiakova, Baker et al. 1996; Youngentob, Margolis et al. 2001; Lee, He et al. 2011). Later work demonstrated that OMP plays a key role in olfactory sensory neuron physiology by controlling enzymatic (cAMP) levels along the signal transduction cascade that influence the speed at which signaling takes place (Dibattista and Reisert 2016). The specific molecular steps along the olfactory transduction pathway that influence signaling speed will be revisited in subsequent sections.

2.1.2. Olfactory Bulb

Moving along the olfactory pathway, OSN axons project through the cribiform plate to secondary neurons found in the olfactory bulb. The spherical conglomerations where these axons project to are called glomeruli, and they are about 50-100μm in diameter. OSN axons form a synapse with secondary neurons, mainly mitral cells and periglomerular cells (Fletcher, Masurkar et al. 2009). Neurons throughout the epithelial layer that express a particular receptor all converge onto a single glomerulus (Mombaerts, Wang et al. 1996). It has been demonstrated that axons of thousands of OSN with the same receptors converge in only 2-4 glomeruli (Ressler, Sullivan et al. 1994; Buck 1996; Firestein 2001). This is shown in **figure 5**.

Figure 5. Convergence of OSN Projections on Olfactory Bulb Glomeruli. *Schematic representation of the combinatorial coding of olfactory receptors in the olfactory bulb (Linda Buck Nobel Lecture 2004 - adapted from Ressler et al. 1993; Sullivan et al.1996).*

2.1.3. Olfactory Cortex

Following the initial events of olfaction occurring at the epithelial level and projection to the olfactory bulb where synapses between OSN axons and dendrites of secondary neurons occur, the olfactory signal is then transmitted to cortical regions in the brain for further processing (**figure 6**). At this point along the olfactory pathway is where cognitive perception of smell takes place. Signals from the olfactory bulb are transmitted to the anterior olfactory nucleus, piriform cortex, periamygdaloid cortex, and entorhinal cortex (Jia, Pustovyy et al. 2016). Signals at the piriform cortex and periamygdaloid cortex project to the thalamus and frontal cortex, where recognition and perception are thought to occur (Shepherd 1994; Anderson, Christoff et al. 2003). Entorhinal cortex information projects to the

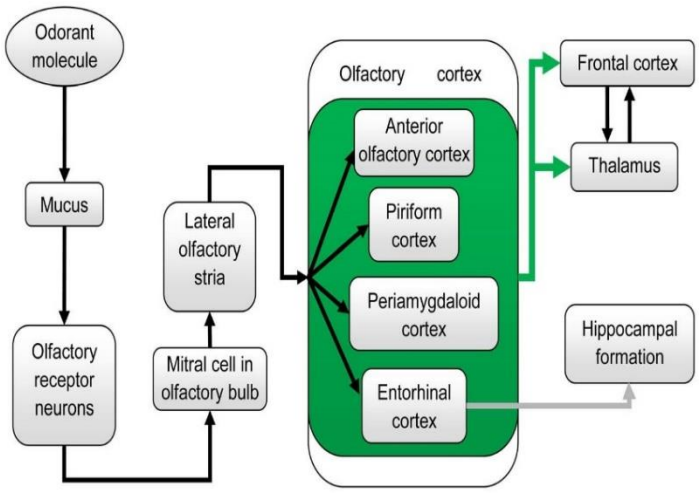

Figure 6. Schematic of Olfactory Cortical Projections. *Odorant ligands are transduced into electrical signals by olfactory receptor neurons. The electrical signals are propagated through the OSN axons to the olfactory bulb, synapsing with secondary neurons that project signals to four main olfactory regions within the brain responsible for perception and odor memory encoding. Bidirectional communication occurs between these regions (Jia et al. 2016).*

hippocampus, where odor memories may be processed (Haberly 2001; Kadohisa and Wilson 2006). Olfactory mapping and correlations are associated with frontal, entorhinal, and periamygdaloid areas (Haberly 2001). Reports suggest periamygdaloid area involvement in processing emotional information related to olfactory stimuli (Anderson, Christoff et al. 2003), while the entorhinal cortex distributes information about olfactory memory (Chapuis, Cohen et al. 2013). An fMRI study in humans demonstrated that medial and orbital parts of the frontal cortex were involved in cognitive integration of sensory stimuli related to prior experiences (Mackay-Sim, Grant et al. 2004). This complex and not-yet fully understood pathway, as well as the interactions between cortical regions related to olfactory processing are shown in **figure 6**.

2.2. Physiology of Olfaction

2.2.1. Organization & Flow of Information

Olfaction begins with the action of sniffing, which transports odorant molecules into the nose and delivers them to the mucus layer covering the olfactory epithelium. The initial events of olfactory transduction take place in the olfactory neuroepithelium situated in the posterior nasal cavity. Olfactory sensory neurons have hair-like cellular structures, called olfactory cilia. Cilia harbor the sensory apparatus, including the olfactory receptor proteins, heterotrimeric G-proteins, and downstream second messenger components involved in the GPCR cascade. These molecules are responsible for converting and amplifying the physical-chemical signal of the odorant into an electrical

current that is then propagated through the higher order olfactory regions in in the brain to be perceived.

The binding of the odorant by a receptor protein initiates an intracellular cascade of signal transduction events, including the G-protein dependent production of second messenger molecules, leading to the opening of ion channels that allow generation of currents. This process triggers an action potential in the axon of the olfactory receptor cell that projects directly to the olfactory bulb and communicates with the synaptic connections with mitral and other secondary neurons at the glomeruli. The olfactory receptor neurons direct their single unbranched axons to the olfactory bulb, passing through the cribiform plate.

Within the olfactory bulb, the axons contact secondary neurons that form spherical glomeruli. The unique wiring of the olfactory system allows discrimination of an enormous number of volatile odorants, where one single sensory neuron expresses a particular olfactory receptor, and each neuron with this receptor type sends their axons to the same glomerulus in the olfactory bulb. From the olfactory bulb the information is projected further to the olfactory cortical regions responsible for higher-order processing and recognition of the signal. At the epithelial level, the odorant is quickly cleared from the mucus, signal deactivation occurs, and the processes may begin again. This chapter will discuss the physiological significance and mechanisms involving the transduction from chemical (analog) signals to electrical (digital) signals. This transition of signals is depicted in **figure 7**.

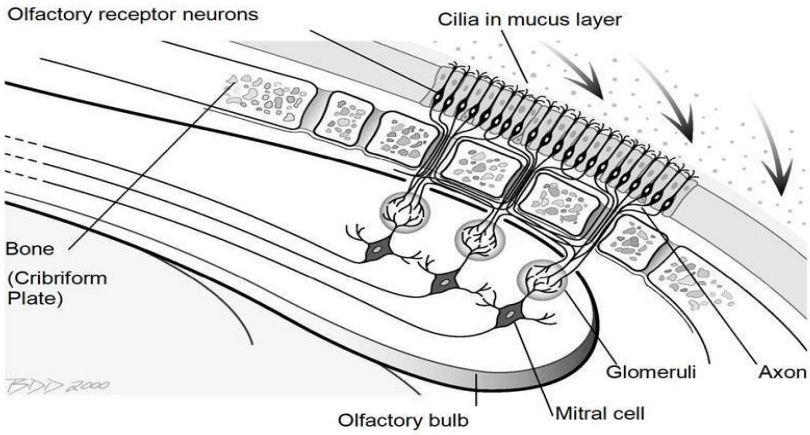

Figure 7. Flow of Olfactory information. *Schematic representation of the flow of olfactory information from initial recognition of chemical odorants at the receptor sites to the generation of electrical signals that are then sent throughout the rest of the olfactory pathway (Illustration courtesy of Vitaly Vodyanoy).*

2.2.2. Olfactory Signal Transduction

Olfactory transduction occurs in the cilia of olfactory sensory neurons. Olfactory receptors are G-protein coupled receptors (GPCR), and they make up the largest family of GPCRs within the mammalian genome (Buck and Axel 1991). This discovery opened the door for olfactory genomic research, and ultimately allowed for a much clearer understanding of olfactory receptor types and transduction cascade mechanisms. Olfactory receptors are 7-transmembrane proteins, consisting of a-helical regions connected by intracellular and extracellular loops (Buck 1993; Firestein 2001). Amino acid sequence comparisons across receptors show that there are conserved regions as well as distinctly variable regions, likely related to the diverse array of odorants that are perceived within the environment (Horowitz, Saraiva et al. 2014). The hypervariable region between receptors is thought the be the specific portion of this protein where odorants interact with and are recognized. In Linda Buck's Nobel Prize lecture (2004),

she discusses how the hypervariability in amino acid residues within the 3rd, 4th, and 5th, transmembrane region is consistent with the ability of receptors to interact with odorants with different molecular shapes.

The binding of an odorant molecule to an olfactory receptor embedded within the ciliary membrane induces a conformational change of the receptor (Lancet and Pace 1987; Buck and Axel 1991), causing a cascade of events initiating the transformation of chemical energy of binding into a neural signal (Paysan and Breer 2001). The overall GPCR cascade is shown in **figure 8**. The ligand-bound receptor activates an olfactory-specific subtype of G-proteins, called G_{olf} (Jones, Masters et al. 1990). In turn, the G-protein stimulates the enzymatic activity of an adenylyl cyclase type III (ACIII) generating an increase in the concentration of cyclic AMP (cAMP) and further downstream events to unfold (Breer 2003; Breer 2003). Cyclic nucleotide-gated (CNG) channels located in the ciliary membrane are directly activated by cAMP, causing a depolarizing influx of Na^+ and Ca^{2+}-ions (Zufall, Firestein et al. 1991; Zufall, Hatt et al. 1993). The intracellular increase of Ca^{2+} concentration directly gates Ca^{2+}-activated Cl^- channels. The opening of Ca^{2+}-activated Cl^- channels causes an efflux of Cl^- ions from the cilia, corresponding to an inward current that further contributes to the depolarization of OSNs (Pifferi, Boccaccio et al. 2006; Kleene 2008). Inactive OSNs generally maintain a resting membrane voltage of about -65mV with respect to the external cellular space. When the CNG channels open and positive ions rush in, this causes the inside of the cell to become less negative. If enough channels are open to cause the membrane potential to reach a certain level of depolarization, the generator potential reaches threshold and an

action potential is generated that is propagated along the axon (Restrepo, Teeter et al. 1996).

The second messenger cascade allows amplification of the chemical signal being transduced (Lamb and Pugh 1992). One membrane receptor activated by an odor ligand has the potential to activate many G-proteins, each of which activate a ACIII molecule capable of producing thousands of molecules of cAMP (Firestein and Zufall 1993; Firestein 2001). The presence of three cAMP molecules open a CNG channel, through which hundreds of thousands of ions can cross the membrane (Firestein 2001).

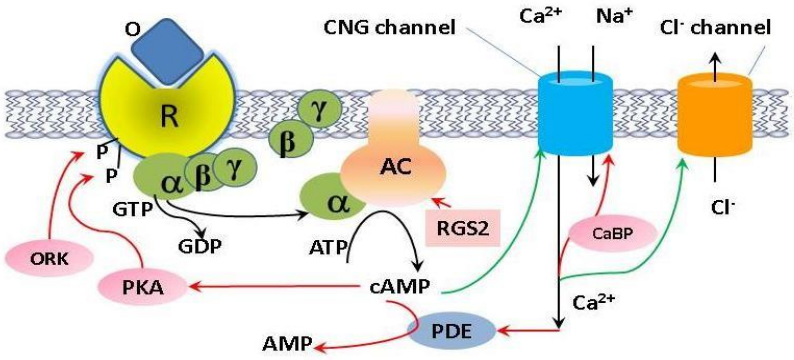

Figure 8. Olfactory GPCR Cascade. *Schematic representation of the signal transduction cascade occurring within olfactory neuron cilia. O-odorant, R-receptor, a-alpha unit, b-beta unit, y-gamma unit of Golf-protein, GTP-guanine triphosphate, GDP-guanine diphosphate, AC-adenylyl cyclase, CNG-calcium nucleotide gated channel, CaBP-calcium binding protein (calmodulin), RGS2-regulator of G proteins, PDE-phosphodiesterase (Dennis, Aono, Morrison 2015)*

Several Ca^{2+}-dependent negative feedback mechanisms contribute to response adaptation and termination of signal. The cilia contain a phosphodiesterase that, after being activated by the complex Ca^{2+}-Calmodulin (CaCaM), hydrolyzes cAMP (Borisy, Ronnett et al. 1992). However, there are some conflicting views of signal transduction, and other mechanisms of adaptation to odor stimulus are suggested (Gold 1999;

Boccaccio, Lagostena et al. 2006). The complex CaCaM and possibly other Ca^{2+}-binding proteins decrease the sensitivity of the CNG channel to cAMP (Chen and Yau 1994; Jaworsky, Matsuzaki et al. 1995; Balasubramanian, Lynch et al. 1996; Mizutani, Sahara et al. 2000; Bradley 2005). The activation of CaCaM-dependent protein kinase II (CaMK) inhibits AC activity (Yang, Cho et al. 2008). Protein kinase A activity was also found to terminate AC activity via phosphorylation reactions (Boekhoff and Breer 1992). Finally, the intracellular Ca^{2+} concentration is reduced by Ca^{2+}-extrusion through a Na^{+}/Ca^{2+} exchanger (Matthews and Reisert 2003).

2.3. Methods of Studying Olfaction

Chemical odorants throughout the environment are inspired through the nasal cavity, where they contact olfactory receptors and induce a conformational change that initiates a cascade of molecular events. Throughout the pathway of olfaction, there are multiple locations where chemical signals are transduced into electrical signals. Chemical odorants, if sufficiently stimulatory to an olfactory sensory neuron, produce a generator potential that reaches a threshold great enough for an action potential to be generated. Once an electrical action potential is generated, this current is propagated through the axon where it reaches the synapse at the olfactory bulb glomeruli. At this point of synaptic contact, the electrical current transforms into a chemical signal that can be detected by secondary neurons within the olfactory bulb. Transmission of olfactory information is then entirely electrical throughout the rest of the pathways within the brain. **Figure 9** depicts this olfactory pathway, and the points of contact that allow insight

into function. Olfactory function is studied in a variety of ways, owing to this transmission of electrical activity.

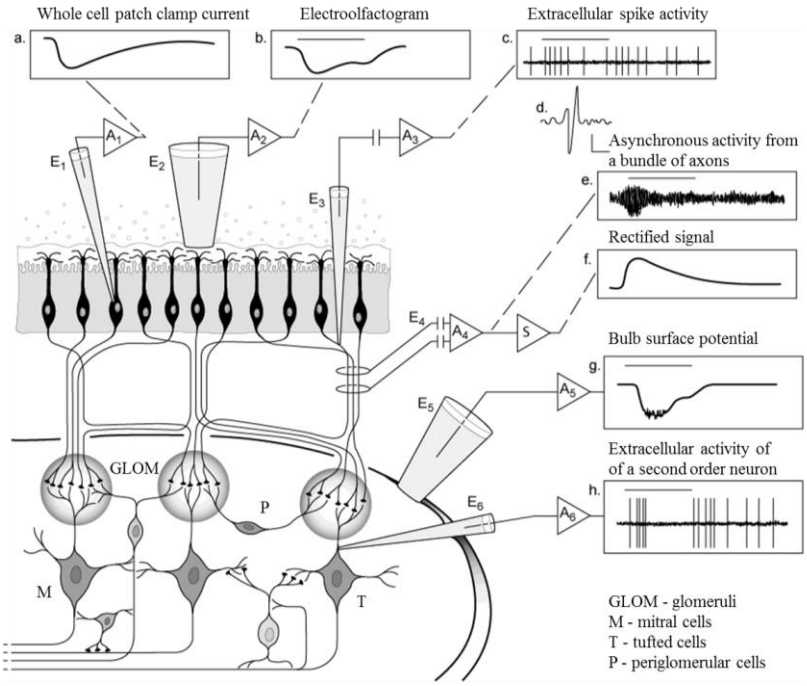

Figure 9. Points of Electrophysiological Points Throughout Olfactory Pathway. ***(A)*** *Measurement of current within the cell body of OSN;* ***(B)*** *Measurement of sum of generator potentials at epithelial surface;* ***(C)*** *Measurement of current within axon extending from OSN;* ***(D, E, F)*** *Measurement of currents from a bundle of axons extending through cribiform plate;* ***(G)*** *Measurement of generator potential at olfactory bulb surface;* ***(H)*** *Measurement of current from secondary neurons at OB glomeruli*

2.3.1. Electroolfactogram (EOG)

A classic method of measuring olfactory function is the electroolfactogram (Hummel, Knecht et al. 1996; Lapid and Hummel 2013). The equipment specific to this method will be further discussed, but the physiological concepts will be discussed here. An EOG readout is the electrical potential recorded at the surface of olfactory epithelium in response to odorant stimulation. Rather than measuring direct current from the axon

extending from a single cell, the EOG measures the sum of generator potentials of olfactory receptor neurons within the vicinity of the pipette making contact with the surface. The amplitude of the EOG is proportional to the logarithm of odorant concentration. It has been suggested that the amplitude of EOG recordings is representative of the percentage of olfactory sensory neurons generating electrical responses, and in turn representative of odorant perception at the cognitive level. **Figure 10** shows the array of instruments that make up a full EOG apparatus conducted on *ex vivo* rodent epithelia.

Figure 10. Electroolfactogram (EOG) Apparatus. ***(1)*** *perfusion chamber: a. epithelium, b. glass microelectrode, c. ag/cl electrode, d. electrode holder, e. head stage, f. ground wire, g. odorant delivery applicator, h. odor plume;* ***(2)*** *Faraday box* ***(3)*** *pressure equilibration table* ***(4)*** *odorant valves and delivery system* ***(5)*** *odor vapor mixing chamber* ***(6)*** *pneumatic pico-pump* ***(7)*** *Patch-clamp amplifier* ***(8)*** *Oscilloscope* ***(9)*** *Analog-digital converter* ***(10)*** *VCR* ***(11)*** *Digidata 1200A* ***(12)*** *Computer hard drive* ***(13)*** *Monitor* ***(14)*** *3D printer*

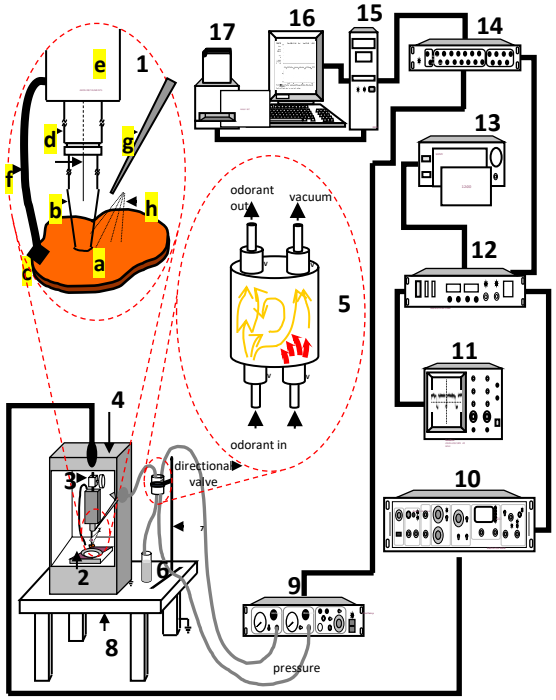

2.3.2. Functional Magnetic Resonance Imaging

Another validated method of olfactory evaluation is functional magnetic resonance imaging. This method does not measure electrical activity by making direct contact with points along the olfactory pathway, but rather reveals the areas within the

brain that show increased activity in response to certain stimuli (Abolmaali, Hummel et al. 2009; Kyathanahally, Jia et al. 2015). Research at Auburn has successfully utilized this method of studying the olfactory system in canines (Jia, Pustovyy et al. 2014; Jia, Pustovyy et al. 2016). The set-up of the functional magnetic resonance imaging apparatus is shown in **figure 11**.

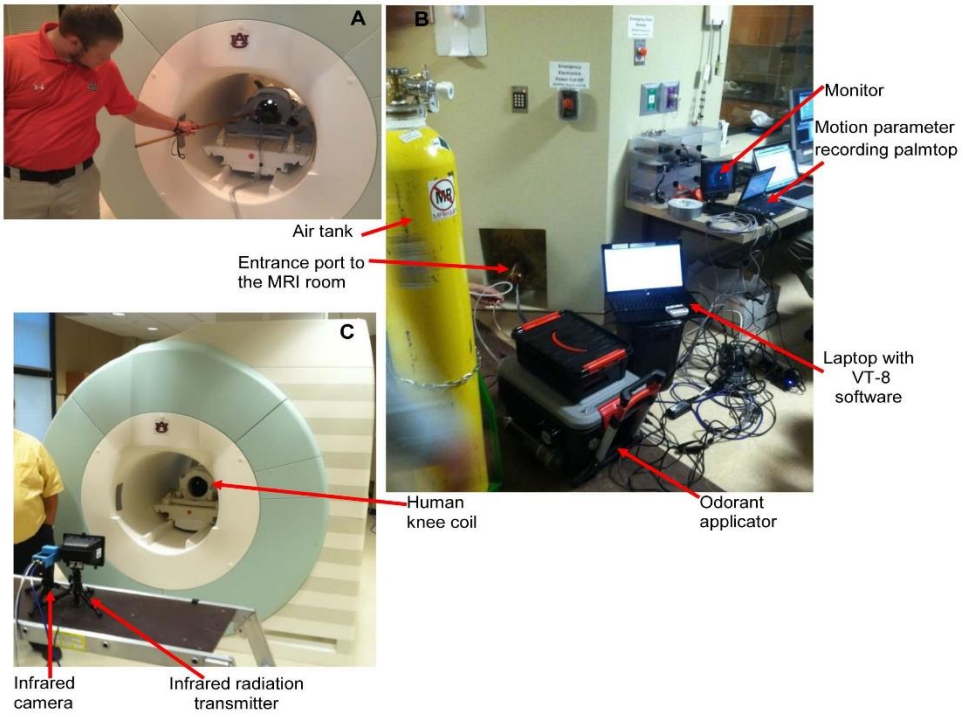

Figure 11. Components of the dog fMRI olfactory imaging system. ***(A)*** *dog training to insert and keep their heads as still as possible inside the human knee coil using positive reinforcement learning (a black dog can be seen inside the coil);* ***(B)*** *components of imaging system outside the MRI room showing odorant applicator, air tank, motion parameter recording palmtop, video monitor, laptop with VT-8 software;* ***(C)*** *Components of imaging system inside the MRI room.*

2.4. Zinc Nanoparticles

2.4.1. Role of Metals in Physiology

Some inorganic elements, including many metals, are essential for normal physiological functioning (Banci and Bertini 2013). While calcium, potassium, and sodium are present in very large quantities and their physiological role in cellular signaling is well understood, some are found in much smaller amounts. Iron, copper, zinc, manganese, chromium, selenium, molybdenum, and cobalt, are all are examples of trace biometals that are considered essential for optimal metabolic function in humans (Aggett 1985). These inorganic elements serve a variety of catalytic, structural, and regulatory functions, in which they interact with proteins, enzymes, and hormones. Many proteins present in living organisms require metal ion cofactors. Other proteins, including hormones, contain metal ions in their structure.

Zinc plays a significant role in neurobiology and is present in many regions of the CNS. The majority of literature concerning zinc activity in the brain involved methods that could not discriminate between zinc ions and zinc metal nanoparticles (Takeda et al. 1997; Takeda 2001). There are reportedly high concentrations of zinc within the olfactory bulb (Donaldson et al. 1973). The measured zinc content in rat blood is ~100 µmole/L (Fugono, et al. 2002), yet the ionic Zn^{2+} concentrations in neuronal extracellular fluid are estimated to be ~0.15 µmole/L (Takeda 2000). Intracellular Zn^{2+} ion concentration in neurons, on the other hand, fluctuates within a narrow picomolar range (Bozym et al. 2006; Li et al. 2009). The physiological role of the endogenous Zn^{2+} ions in the olfactory sensory neurons is not fully clear, due to the previous inability to distinguish between

ionic and non-ionic forms of zinc. However, addition of zinc ions has demonstrated inhibition of the stimulatory GTP-binding protein to adenylyl cyclase (Gao et al. 2005), an essential step in the initial events of olfactory signal transduction. The physiological role of endogenous Zn^{2+} ions in olfactory bulb neuronal activity has also been investigated. Zinc ions can be released by membrane depolarization at synaptic terminals and reach extracellular synaptic concentrations of 100–300 μmole/L. The released zinc modulates neuronal excitability (Horning et al. 2000; Horning and Trombley 2001). Deficiencies in such fundamental elements can result in dysfunction ranging from misfolded proteins to inhibition of metabolic pathways. Loss of sufficient zinc concentrations demonstrated neurological dysfunctions such as cerebellar dysfunction, anorexia, and taste and smell dysfunction (Henkin, Patten et al. 1975).

However, certain metals at higher concentrations can also have toxic or adverse effects. It has been reported that zinc ions delivered through intranasal sprays can cause anosmia in humans (Alexander and Davidson 2006). Zinc sulfate also demonstrated an anosmic or hyposmic effect in mice (McBride, Slotnick et al. 2003). Embryonic cadmium and other metal exposure resulted in the induction of systemic stress response and cell death during development, followed by long-term olfactory deficits (Blechinger, Kusch et al. 2007). Biometals can have stimulatory or inhibitory effects depending on the transductory pathway. For that reason, the specific mechanistic roles and full understanding of beneficial effects versus toxicity for most trace elements are incomplete and sometimes contradictory between investigators.

Metal ions likely play a role specifically in GPCR activation and molecular interactions along the transduction cascade. Cations Mg^{2+} and Mn^{2+} were shown to

modulate ligand-binding of opioid receptor subtypes (Standifer, Murthy et al. 1991). Cu^{2+}, Zn^{2+}, and Ni^{2+} were found to increase the affinity of a ligand to CXCR4 chemokine receptors (Gerlach, Jakobsen et al. 2003). Zn^{2+} was found to bind and activate melanocortin MC1 and MC4 receptors (Holst, Elling et al. 2002). Copper and zinc cations showed modulation of neuronal excitability (Delgado, Vergara et al. 2006). Zinc ions induced a significant and reversible attenuation of electrical response signals, even with the excitatory activity of adenylyl cyclase stimulator (forskolin) and phosphodiesterase inhibitor (IBMX) (Ishimaru 2000). It was suggested that the zinc ions induced this attenuation via blockage of cyclic nucleotide ion channels. Furthermore, copper and zinc ions demonstrated inhibition of the alpha (α) subunit of G_{olf} (Gao, Du et al. 2005). Zinc ions may influence conformation changes of adenylyl cyclase, reducing its proper enzymatic activity (Klein, Sunahara et al. 2002; Klein, Heyduk et al. 2004).

2.4.2. Zinc Nanoparticle Discovery and Role in Olfaction

Luca Turin proposed an inelastic electron tunneling mechanism in support of the vibrational theory of olfaction. In this suggested mechanism, the receptor receives electrons from a donor that are then passed to G_{olf} following activation from an odor ligand binding event. The plausibility of this model was examined and found to be consistent with the underlying physical parameters and molecular activity observed throughout the initial events of transduction (Brookes 2007). In this model, the introduction of an electron donor/acceptor acting as a reducing/oxidizing agent in the intracellular fluid is necessary. One suggestion was that zinc could be a potential candidate. It was thought that zinc binding sites may be present on both the odorant

receptor and the G-protein, and that they could assist the signal transfer from receptor to G-protein

In 2005, there was a novel discovery of metallic clusters in human, rabbit, and dog blood when micrometer and submicrometer particles termed proteons were isolated from freshly drawn samples (Samoylov, Samoylova et al. 2005). Analyses of the particle clusters confirmed the presence of 40-300 atoms, including copper, zinc, and iron. Given the proposed electron tunneling mechanism and the natural presence of metal nanoclusters (possible electron donors) within the systemic circulation, it was hypothesized that these nanoparticles could be involved in the signal transduction between olfactory receptors and G_{olf} proteins. In 2009, our colleagues demonstrated that a very small concentration of zinc metal nanoparticles, specifically, enhance electrical responses to odorant stimulation (Viswaprakash, Dennis et al. 2009; Vodyanoy 2010).

Zinc ions and zinc nanoparticles are distinct from one another, as ions are single charged atoms and nanoparticles are clusters of uncharged atoms (Viswaprakash, Dennis et al. 2009). The structural and catalytic properties of metal nanoparticles differ from ions (Thomas 1988; Aiken and Finke 1999; Viswaprakash, Dennis et al. 2009; Viswaprakash, Josephson et al. 2010; Vodyanoy 2010). Though the ionic form of zinc has been reported to have inhibitory effects on olfactory function, zinc nanoparticles demonstrated a starkly contrasting effect. A stoichiometric model of the interaction between metal nanoparticles and olfactory receptors was proposed in 2010, based on experimental results and binding reaction calculations (Vodyanoy 2010). This model suggests that one zinc metal nanoparticle binds two receptor molecules to create a

dimer. This homodimer formation is thought necessary to initiate activation and downstream events of the signal transduction cascade.

Subsequent work further supported the role of zinc nanoparticles in olfaction. In 2011, it was shown that the addition of zinc nanoparticles to standard odorant solution enhanced EOG responses to explosive related odorants (Moore, Pustovyy et al. 2011). That work demonstrated the potential use of zinc nanoparticle administration to canine olfactory epithelia for the purpose of enhancing explosive detection for transportation and military security. Olfactory enhancement of zinc nanoparticles at the cognitive level was assessed using functional magnetic resonance imaging of canine brains (Jia, Pustovyy et al. 2016) and it was found that the enhancement of olfactory receptor responses by zinc nanoparticles leads to increased activity in olfactory-related and higher order regions of the brain. This further demonstrated the potential of zinc nanoparticles to enhance canine olfactory sensitivity for the detection of target substances. The next major steps in the zinc nanoparticle investigation were then to confirm their endogenous presence at the olfactory epithelial surface and compare their efficacy to our laboratory engineered preparations, and finally to evaluate the stability of such zinc nanoparticle preparations for long term use under variable environmental conditions. We have physically characterized our nanoparticle preparations and assessed their susceptibility to temperature stress and age, and this work will be presented in chapter 5, section 5.6 (Hagerty, Daniels et al. 2016; Singletary, Hagerty et al. 2017).

2.5. Microbial Influence on Systemic Interactions

2.5.1. Gut-Brain Axis

The community of microorganisms residing in the human body, collectively termed the microbiota, have major influences on overall physiological homeostasis. The microorganisms play metabolic, protective, and trophic roles within the gastrointestinal tract. The gut microbiome, collectively considered an organ, has significant regulatory functions including energy extraction during digestion, barrier fortification, and immune modulation (Chen, Li et al. 2015). Normal microbiota composition is crucial for proper physiological functioning, and dysbiosis is implicated in a wide array of disease states. Microbiota composition is highly specific to a single individual, described as a "fingerprint". For that reason, there is not one blueprint for the healthy microbiota composition is. Many animal and clinical studies have investigated this question in attempts to find which species are most predominantly associated with health and those with disease. The association of microbiota with intestinal diseases such as irritable bowel syndrome and inflammatory bowel diseases is strongly supported (Bienenstock, Kunze et al. 2015). There are many links between the inflammatory symptoms of GI disorders and dysbiosis. A strongly supported relationship is that between gut microbiota composition and neurophysiological functions in the brain, influencing behavior and other sensory functions (Bravo, Julio-Pieper et al. 2012; Forsythe, Kunze et al. 2012; Yang and Chiu 2017)

The gut is highly innervated, housing its own branch of the nervous system called the Enteric Nervous System, which communicates with the central nervous system

through vagas nerve pathways (Forsythe, Bienenstock et al. 2014). There is a growing body of evidence suggesting a strong association between the gut microbiota and brain, called the gut-brain axis. Mechanisms underlying the regulation of energy and body fat mass are thought to involve energy balance circuitries in the hypothalamus and brainstem (Schele, Grahnemo et al. 2015). Microbiota produce neuro-active substances such as catecholamines, histamine, and other compounds that can stimulate hose neurophysiology and modulate motility functions in the intestine (Villanueva-Millan, Perez-Matute et al. 2015). The microbiota-gut-brain axis provides the very close relationship between microbial communities and nervous system health. There is a two-way communication pathways between the brain and gut, with afferent and efferent fibers transmitting sensory information (Konturek, Konturek et al. 2004). Along with the physiological role in the gut, microbiota is believed to be a strong effector of cognitive functioning and behavior.

The brain and gut communicate bidirectionally in a top-down and bottom-up manner. The ability of microbiota to impact nervous function has been a recent area of research interest, as common GI diseases are commonly comorbid with psychiatric disorders. Additionally, it has be reported that induction of stressful events are often linked with initiation, duration, and severity of symptom flares in IBS patients (O'Malley 2015). There are various afferent and efferent pathways involved in the gut-brain communication, including neural, humoral, immune, and metabolic pathways (Burokas, Moloney et al. 2015). The brain and gut develop simultaneously into the central and enteric nervous systems during gestation. These remain connected via the vagal nerve throughout life, through which the brain sends signals to the gut and vice versa.

The gut, and how what we ingest influences it, can in turn influence our brain and sensory system functions. Antibiotics, environmental and infectious agents, intestinal neurotransmitters, sensory vagal fibers, cytokines, and metabolites all convey information to the CNS about the intestinal state (O'Malley 2015). The brain to gut communication involves circuitries including the hypothalamic-pituitary-adrenal axis, CNS regulatory areas of satiety, and neuropeptides released from sensory nerves, which affect gut microbiota composition (Petra, Panagiotidou et al. 2015). Investigating the interactions between gut microflora and the CNS involves research using germ-free animals, fecal transplants, probiotics, and antibiotics. Understanding the molecular underpinnings of how microbiota composition impacts brain function and behavior has not been fully developed. Immune mediators such as pro-inflammatory cytokines are characteristic of most intestinal diseases and may directly affect neural signaling. While both animal and clinical studies show that diet, stress, administration of probiotics, and antibiotics can impact gut microorganism communities, further investigations are needed to determine specific pathways with more certainty. Variations of microbe composition may provide methods of modulating mood, sleep patterns, eating behaviors, and sensory function.

The relationship between microorganisms and olfaction, specifically, is an area in increasing interest. As anosmia is an early symptom common to several neurodegenerative diseases (Berstad and Berstad 2017), this suggests that degradation of the central nervous system function directly effects olfactory sensory neurons and their transduction pathways. The microbiome specific to the nasal cavity may also shape olfactory function (Koskinen, Reichert et al. 2018) (Herbert, Harris et al. 2012).

2.5.2. Microbiome and Olfaction

There is a significant amount of evidence supporting the notion that the microbial species associated with an organism plays an important role in olfactory-related behaviors, such as food acquisition, social interactions, and mate preference. Bacterial species have been shown to influence social behaviors such as swarming in desert locusts (Dillon, Vennard et al. 2002), aggregation in cockroaches (Wada-Katsumata, Zurek et al. 2015), and speciation in *Drosophila melanogaster* (Sharon, Segal et al. 2010). In agreement with the evidence suggesting that microbial composition influences these papers, it was found in several studies that antibiotic treatment abolished these behavioral patterns, and were restored following reintroduction of a single bacterial strain (*Lactobacillus plantarum*) (Sharon, Segal et al. 2010). It may seem implausible to think that microbial species found throughout the body would have interactions with olfactory receptors in the nasal cavity that could influence such a wide variety of behaviors.

However, growing evidence has surfaced which demonstrates the presence of olfactory receptors among a variety of non-sensory systemic tissues in both humans and rodent models (Feldmesser, Olender et al. 2006; Ichimura, Kadowaki et al. 2008; Kang and Koo 2012). The presence of olfactory receptors and olfactory receptor gene expression has been shown in the GI tract (Cui, Tsolakis et al. 2013), skin (Busse, Kudella et al. 2014), testis (Spehr, Gisselmann et al. 2003; Fukuda, Yomogida et al. 2004), muscle cells (Griffin, Kafadar et al. 2009), pancreas (Kang, Bahk et al. 2015), heart (Kim, Yoon et al. 2015), liver (Wu, Jia et al. 2015), and kidneys (Shepard and Pluznick 2016). Though olfactory receptor expression may be highest within the olfactory epithelium, their presence throughout various tissues that do not have specific

functional roles related to olfactory transduction suggests potential roles as mediators of complex interactions between organs. **Figure 12** shows a schematic of ectopic olfactory receptor distribution. It is likely that olfactory receptors play important roles in whole-body physiology. Each of the studies referenced above investigated the potential roles of olfactory receptors within each of the tissues they were found. OR2AT4 was found to be involved in wound-healing processes in human keratinocytes (Busse 2014). Mouse OR23 demonstrated a role in promoting muscle regeneration (Griffin 2009). Mouse OR544 was found to play a key role in the regulation of glucagon secretion in alpha-cells of pancreatic islets (Kang 2015). Human OR10J5 was found to play a functional role in angiogenesis within heart aorta, coronary artery, and endothelial cells (Kim 2015). Odorant receptors found in both human and mouse testis have also demonstrated a role in sperm chemotaxis (Speher 2003; Fukuda 2004).

Piecing together the potential roles that olfactory receptors play to regulate whole-body physiology is still a relatively new area of investigation and the complexity is not fully understood. A unique challenge specific to olfactory receptor studies is the difficulty of experimentally expressing olfactory receptor proteins to the cellular surface. For this reason, less is known about the specific mechanisms of olfactory receptors and their vast roles throughout the body, relative to other receptor types. Efforts have been directed towards developing new antibodies against molecular components of the olfactory GPCR cascade that are functional in providing insight into the mechanism, which have been critical in understanding the major steps of signal transduction.

Olfaction is the earliest and most evolutionarily conserved sensory function across vertebrate and invertebrate species. Adding to the physiological relevance of olfactory

receptors, specifically, is that they comprise the largest family of mammalian GPCRs (Buck and Axel 1991; Buck 1992). The sense of smell is crucial for the purposes of mate selection, social behaviors, food acquisition, protection from harmful stimuli, and threats to survival. It seems logical, evolutionally speaking, that olfactory receptors would not be localized to one sensory region of the body, but instead encompass multi-organ regulatory roles. Similarly, the microbiome across eukaryotic species plays a vastly diverse role in overall systemic health across species. The diverse, yet holistically interconnected systems suggest that investigation of any one function in an organism requires consideration of the whole genome that it encompasses, including microorganisms which are often referred to as an organ itself. The microbiome associated with an organism is considered part of its systemic organs that may influence its overall functioning and behavior (Bienenstock, Kunze et al. 2017). The microbiome has been reported to modulate olfactory function, particularly odorant stimulation (Francois, Grebert et al. 2016). Bacterial by-products, including short chain fatty acids (SCFA), β-phenylethylamine (PEA), and trimethylamine (TMA) can act as odorants that may act on ectopic olfactory receptors throughout the body. It is currently unclear whether non-sensory olfactory receptors throughout various tissues signal to the same cortical areas of the brain as in the classical olfactory pathway.

The microbiome is often thought to be localized mainly in the gut. While the vast majority of bacterial species resides in the intestinal organs, there is also a fair amount of bacteria present throughout other tissues of the body, including the skin and nasal cavity, which are both in direct contact with the external environment. For this reason, it is very logical to assume that the bacterial composition present at the olfactory epithelial surface

within the nasal cavity could strongly influence olfactory sensory neuron activity. **Figure 12** shows a schematic representing the proposed mixture of microbes and odorants at the olfactory epithelial surface. Characterization of nasal cavity bacteria composition and potential effects this has on olfaction is new area of investigation that is in recent development. A very recent publication (Koskinen, Reichert et al. 2018) explored the relationship between olfactory function and nasal microbiome in human subjects. Their overall conclusions were that butyric acid-producing microorganisms were associated with hyposmia, or olfactory deficits. It seems evident that microorganisms found throughout body and within the nasal cavity may influence and strongly shape olfactory function, potentially by the production of odor compounds that interact with olfactory receptor neurons. Given the beneficial effects of probiotic species in treating gastrointestinal diseases, alteration of the nasal microbiome using probiotics could be a plausible therapeutic for anosmia and anosmia-associated diseases.

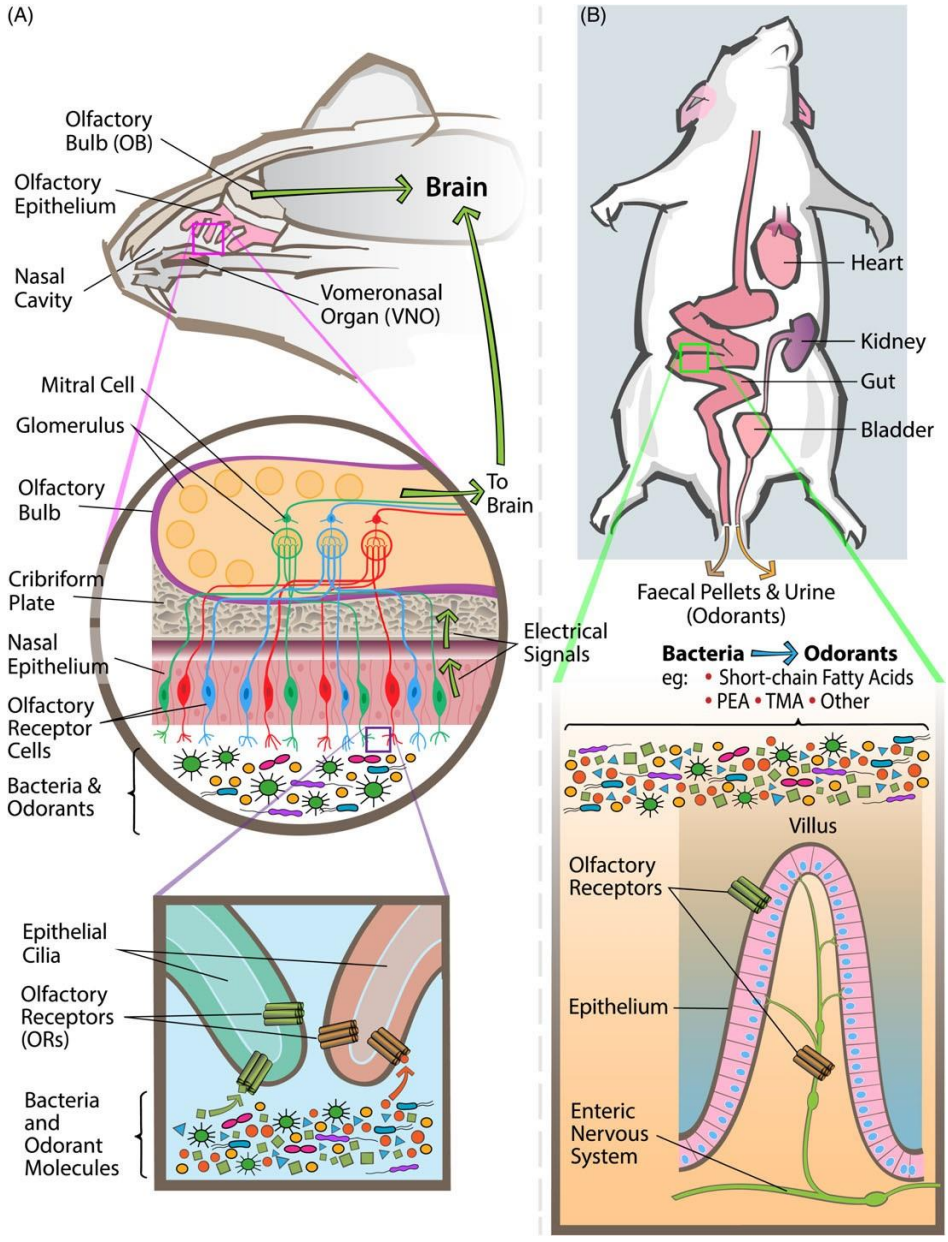

<u>Figure 12.</u> Schematic Diagram of the Mammalian Olfactory System and Distribution of Olfactory Receptors Throughout Sensory and Non-Sensory Tissues. ***(A)*** *Flow of olfactory information, including both Main Olfactory System (OE) and Accessory Olfactory System (Vomeronasal Organ VNO), which project sensory information from volatile odorants and pheromones to olfactory cortical regions in the brain. The epithelial surface consists of inspired odorants, bacterial species, and their odorant by-products.* ***(B)*** *Olfactory receptors have been found throughout non-sensory tissues and are referred to as ectopic ORs* (Bienenstock 2017; figure adapted from Rinaldi et al. 2007).

2.6. Heat Stress

2.6.1. Physiological Stressors

Any disruption of homeostasis is considered a physiological stressor. Stress can be psychological or physical and can occur in acute or chronic time frames. The duration of stress exposure can elicit different systemic responses (Baumann, Urmantscheeva et al. 1977). Acute stress induces a direct redistribution of energy to re-achieve homeostasis. In contrast, chronic stress results in the adaptation of neural pathways to cope with the long-term changes to the host physiological balance. Extreme and chronic challenges to homeostasis can adversely affect systemic functions and result in multi-organ failure.

2.6.2. Environmental and Exercise-Induced Heat Stress

Temperature related stress is a major challenge to both human and animal health. Thermoregulatory mechanisms allow organisms to withstand large variations in environmental temperatures, but relatively small increases in internal temperature can lead to central nervous system dysfunction, heatstroke, and even death. There are approximately 200 heat stress-related human deaths per year in the United States (Leon and Helwig 2010). The ultimate cause of mortality is multi-organ system failure due to systemic inflammatory responses. Heat shock proteins and other regulatory molecular signals are upregulated in times of temperature stress and can modulate various physiological functions (Horowitz and Kodesh 2010). If stressful conditions persist, these responses are no longer beneficial and rather are problematic to overall health. Leon et al. investigated metabolic and behavioral responses to heatstroke in a conscious mouse

model and found that thermoregulatory dysfunction as a result of brain damage caused a typical hypothermic core temperature followed by hyperthermic core temperature during recovery (Leon, Gordon et al. 2010). Working dogs, especially in the military and police force, are exposed to some of the most extreme environmental conditions in the world. Sometimes these conditions exceed their thermoregulatory capabilities and cause permanent damage or death. Increasing efforts are directed towards preventing heat stroke related complications (Yokota, Berglund et al. 2014) by designing temperature-controlled kennels for the animals to be housed and limiting their exposure to extreme environmental temperatures. Heatstroke is prominent in military working dogs compared to cases presented to hospitals from the general dog population (Bruchim, Aroch et al. 1985). This group aimed to evaluate the training conditions and adaptive responses to environmental factors in order to create appropriate prevention and treatment to military working dog exposure to heat stress.

Similar to passive exposure to extreme temperatures, exercise-induced heat stress presents adversity to mammalian physiology (Horowitz and Kodesh 2010; Diverio, Guelfi et al. 2015). Athletes, racing animals, and working dogs that undergo strenuous exercise for extended periods of time are subject to inflammatory responses and overall health challenges (figure 12). Moderate exercise training was found to cause hypertrophy, hyperplasia, upregulation of heat shock protein HSP70i, and an increase in oxidative stress markers in two types of skeletal muscle (Abruzzo, Esposito et al. 2013). The coupling of strenuous metabolic activity and extreme temperatures presents unique adversity, with increased inflammatory and immune modulators (Bruchim, Aroch et al.

1985; Horowitz and Kodesh 2010). **Figure 13** depicts the systemic interactions and effects of environmental and exercise-induced heat stress.

2.6.3. Heat Stress Complications in the Gastrointestinal Tract

Heat stress causes significant morphological and physiological changes in the gastrointestinal tract (Moore, Globa et al. 2014; Giblot Ducray, Globa et al. 2016; Sorokulova, Globa et al. 2016). Heat exposure has been shown to cause damage and morphological shortening of intestinal villi, inducing epithelial cell shedding and exposure of the lamina propria submucosal area (Yu, Yin et al. 2010). The loss of epithelial integrity reduces the protective barrier responsible for defense against bacterial translocation. Lipopolysaccharides (LPS) are bacterial toxins that have been shown to diffuse from the intestinal lumen and enter the systemic circulation following exposure to heat stress (Moore, Globa et al. 2014). When LPS is not sufficiently cleared from the circulation a systemic inflammatory response can occur, leading to disseminated intravascular coagulation, necrosis of organ cells, and multi-organ failure (Giblot Ducray, Globa et al. 2016). It was shown that elevated body temperature causes increased erythrocyte shedding, or programmed red blood cell death, resulting in the formation of echinocytes (Moore, Globa et al. 2014). Additional reported adverse effects of heat stress

include increased levels of pro-inflammatory cytokines such as IL-1, IL-6, TNF-α, and TNF-γ (Staton, Dench et al. 1995; Leon and Helwig 2010).

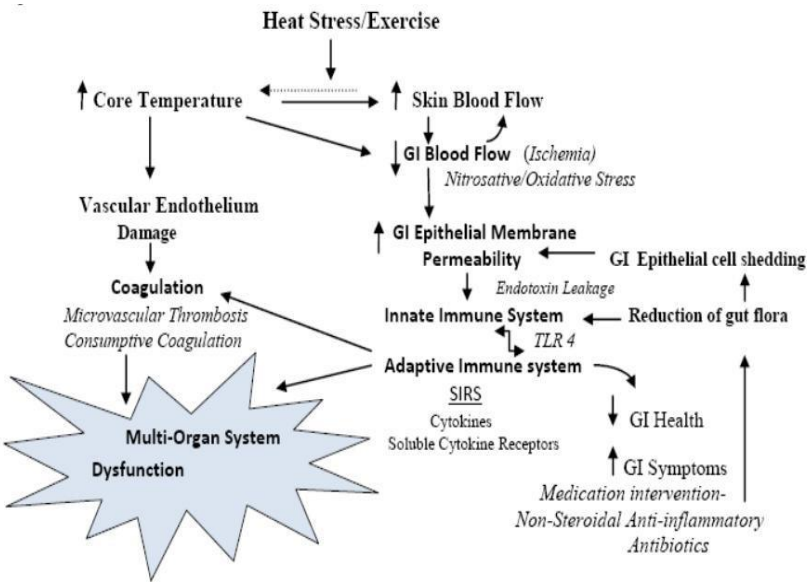

Figure 13. Multi-Organ Dysfunction Induced by Heat Stress and Over Exertion. *Increased core temperature increases blood flow to the skin, reduces intestinal blood flow leading to possible ischemia, increases intestinal permeability leading to diffusion of endotoxins into the circulation and subsequent immune responses and inflammation.*

2.6.4. Probiotics Mitigate Adverse Effects of Heat Stress

The beneficial effects of probiotics in intestinal and systemic physiology have been heavily reported and strongly supported. Administration of probiotics have shown to be effective in reducing adverse symptoms associated with microbial dysbiosis and stress conditions. Oral treatment with *Lactobacillus rhamnosus* attenuates deficits and immune changes associated with chronic stress (Bharwani, Mian et al. 2017). Chronic stress-induced brain abnormalities have also been prevented with beneficial probiotic administration (Ait-Belgnaoui, Colom et al. 2014). The beneficial effects on overall

health stem from the enhancement of barrier function and dampening of inflammation. Mechanisms of probiotic action include restoration of microbial homeostasis, interference with pathogenic bacteria via resource competition, modulation of local and systemic immune responses, and stabilization of epithelial components to increase barrier integrity (Moore, Globa et al. 2014). The following figures are presented by Sorokulova (2016) demonstrating the preventative actions of *Bacillus subtilis*. **Figure 14** is an assessment of morphological changes in the small intestines associated with heat stress. Groups that were pretreated with probiotics showed significant reduction in the adverse effects that heat stress had on villi height and mucosal thickness**. Figure 15** shows the biochemical analyses of blood collected from stress and control animals that were either treated with probiotics or PBS. Pretreatment with probiotics significantly reduced bacterial translocation and toxic LPS components in the circulation.

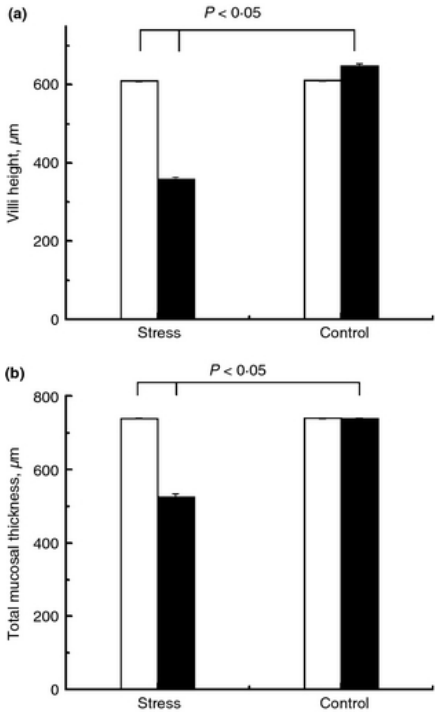

Figure 14. Measurement of intestinal villi height and mucosal thickness. *Rats pre-treated with PBS (black columns) or Bacillus subtilis probiotic (white columns) were exposed to heat stress (45°C) or control room temperature (25°C).* ***(A)*** *Stressed animals treated with PBS had significantly reduced height of intestinal villi (375μm) compared to stressed animals that were pretreated with probiotics (600μm);* ***(B)*** *Stressed animals pretreated with PBS had significantly reduced thickness of intestinal mucosa (500μm) compared to stressed animals pretreated with probiotics (700μm) (Sorokulova et al. 2016).*

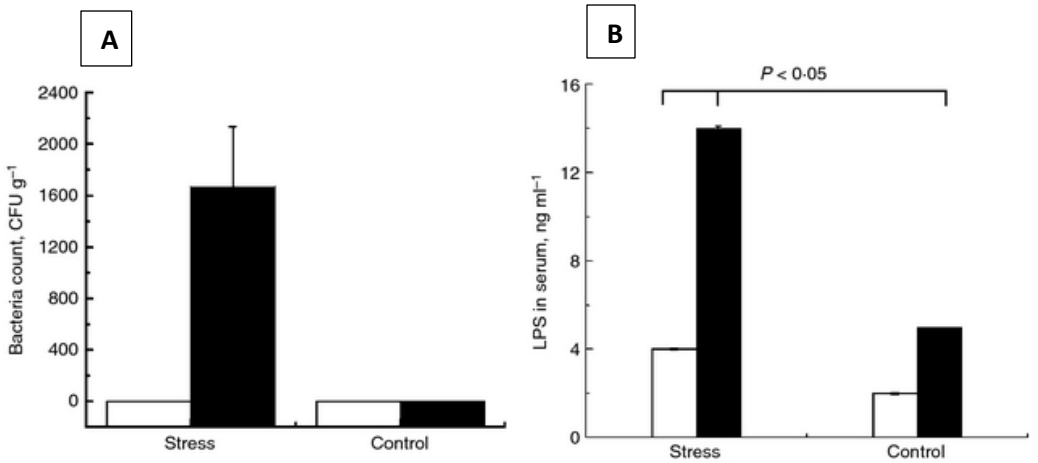

Figure 15. Biochemical Analyses. *Rats pre-treated with PBS (black columns) or Bacillus subtilis probiotic (white columns) were exposed to heat stress (45°C) or control room temperature (25°C).* ***(A)*** *Total bacterial count outside of the intestines measured in the liver, spleen, and lymph nodes – stressed animals pretreated with PBS had significantly greater bacterial translocation from intestinal lumen (~1600 CFU/g) compared to stressed animals pretreated with probiotic (~0 CFU/g);* ***(B)*** *LPS concentration in blood serum – stressed animals pretreated with PBS had significantly greater LPS endotoxin in blood serium (~13 ng/ml) compared to stressed animals pretreated with probiotic (~4 ng/ml) (Sorokulova et al. 2016).*

2.6.5. Temperature Effects on Olfaction

A relatively small number of groups have investigated the direct effects that temperature has on the olfactory system. Early in the olfactory literature, following the discovery that olfactory receptors were members of a vast and diverse family of GPCRs, Hanada et al. considered the potential impact that temperature changes may have on the membrane fluidity of olfactory receptors cells. They examined the effects of temperature changes on odor-discriminating ability of turtle olfactory receptors *in vivo* by cross examining the epithelial membrane fluidity and olfactory bulb responses at increased temperature. Results showed that membrane fluidity of cells isolated from olfactory epithelia changed in a similar temperature range as the decrease of odor-discriminating ability (Hanada, Kashiwayanagi et al. 1994). Temperature has been described as a

stimulus for sensory neurons of the Grueneberg ganglion located at the entrance of the nose (Mamasuew, Breer et al. 2008), and Kludt et al. investigated the effect of temperature stimulation on chemosensory signal processing (Kludt, Okom et al. 2015). They specifically assessed neuronal responses in the glomeruli and mitral cells within the olfactory bulb using calcium imaging and fast line-scanning microscopy and showed that olfactory bulb glomeruli receiving input of olfactory sensory neurons was sensitive to temperature drops (Kludt, Okom et al. 2015). The temperature-sensing transduction mechanisms in neurons at the epithelial and higher-order olfactory bulb regions have been characterized in mice and rats (Mamasuew, Hofmann et al. ; Fleischer, Mamasuew et al. 2009) but further investigation is required to understand the molecular changes occurring at the epithelial surface and systemic biochemical interactions.

Nagappan et al. (2017) published a recent paper which discussed the importance of olfactory sensory functioning in military combat zones. In this review, they discussed the impact that varying environmental conditions likely have on olfaction mainly through alteration of the chemical composition of volatile odorants and the soluble mucus layer lining the epithelium (Nagappan, Subramaniam et al. 2017). Olfactory function relies on the concentration of odorous vapor in the inspired air as well as the ability for volatile compounds to dissolve into the mucous lining where they contact receptors. Temperature, humidity, atmospheric pressure, and airflow are all environmental conditions which can affect the earliest events of the olfactory pathway(Nagappan, Subramaniam et al. 2017). First and foremost, airflow influences the direction in which odorants travel and what frequency that will enter the nasal cavity. Temperature and humidity affects molecular movement and odorant concentration within the vapor being inspired. Furthermore,

increased heat or dry conditions effects evaporation rate of the mucous lining, therefore affecting the activity of odorants traveling into the airways. Increased heat and mucus evaporation could mean increased clearance of the odorants that made their way into the nasal cavity and reduce the overall range of volatile compounds that are able to activate receptors.

2.6.6. Thermodynamics of Cellular Signal Transduction

Cellular signaling through G-protein coupled receptor cascades, across various pathways, involve a plethora of molecular interactions and rate-limiting steps. Ligand-binding events induce receptor activation, enzymatic activity, and ion channel opening to induce cellular depolarization resulting from charge influx/efflux across the cellular membrane. If depolarization of a single cell reaches activation threshold, an action potential is generated in that cell. Depolarization follows an action potential, as the cell returns to its baseline resting membrane potential, and subsequent activation cannot occur during this refractory period until repolarization is complete. Many factors including ligand concentration, rate of stimulation, and temperature, can affect steps along the GPCR cascade, in turn influencing the speed at which a given cell can activate and deactivate a signal response (Reisert and Zhao 2011).

Different odorants have been found to result in different rates of activation and second messenger activity (Boekhoff, Tareilus et al. 1990). Kinetic models have been used to predict the instantaneous spike rate of olfactory neuronal responses based on the quality and concentration of odor stimulus (Getz 1999). A major influence on rate of activation is ion channel activity. Insight into the physical nature of ion channel

activation can be obtained by studying currents at different temperatures because the rates of different conformational changes underlying the activation process can depend on thermal properties.

The second law of thermodynamics carries that energy of all kinds disperse if not hindered. Each form of energy, including kinetic, potential, thermal, electrical, etc., that we experience in every physical aspect of life follows this law. The thermodynamic properties of a system or reaction can be quantitatively measured and determine the overall energetic efficiency. These major quantitative measures of a system include reaction rate, activation energy, entropy, enthalpy, entropy contribution, and free energy. The speed of a given reaction is characterized by reaction rate, or variable "k". Activation energy "Ea" is the barrier threshold required to initiate a reaction. Enough energy must be present or added to the system for the reaction to carry out. Entropy "S" is the dispersal of energy and is generally described as an increase in "disorder" of molecules within the system. Entropy is usually measured as the change from initial to final molecular order, or "ΔS". Enthalpy "H" is the total heat content of a system, including both internal and added heat. Similar to entropy, it is usually referred to as a change from beginning to end,

or “ΔH”. Free energy “ΔG” is essentially described as the amount of energy left over after a process is complete that has the capacity to do work or reverse the reaction.

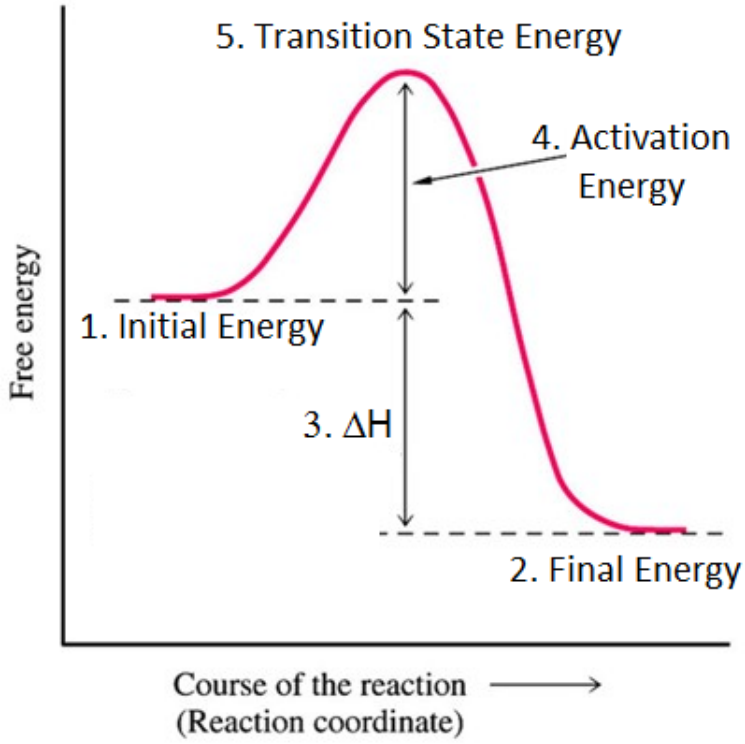

Figure 16. Energy of Transition State Reactions. *An activation energy (Ea) barrier is the minimum amount of energy required to reach molecular transition state of a reaction.*

A Swedish chemist named Svante Arrhenius is known for his contribution to the development of a mathematical expression in 1889, which describes the effect of temperature on the rate of a chemical reaction. The “Arrhenius equation”, which will be specifically written out in later chapters, is often used to show the effect of a change of temperature on the rate constant. This relationship is applicable to most kinds of reactions, though later scientists have developed similar theories that may be more specific to molecular reactions, such as that of olfactory receptor and odorant protein-

protein binding. Most important, Arrhenius showed that even a small increase in temperature to the reaction could produce a marked increase in the reaction-rate constant. In addition to reaction rate, activation energy of a reaction can be calculated using the Arrhenius equation.

Another commonly used method of calculating reaction rate constants is the Eyring equation. Developed by Henry Eyring in 1935, this equation is similar in nature to Arrhenius, but more specifically related to bimolecular reactions as it is derived from the transition state theory. Using this equation, one can calculate other thermodynamic properties of a system including enthalpy, entropy, and free energy. Relating the Arrhenius and Eyring equations allows

Nache et al. (2008) performed a thermodynamic analysis of the activation gating in cyclic nucleotide gated (CNG) channels using the Eyring rate theory, which simplifies the activation kinetics to a model consisting of an open and closed state to estimate enthalpic and entropic energy contributions associated with total activation gating. They found that lowering the temperature shifted the concentration-response relationship to lower concentrations, resulting in a decrease of both enthalpy and entropy during channel opening (Nache, Kusch et al. 2008). Similar estimations have been conducted for voltage-gated K^+ channels (Tsien, Noble 1969; Meyer and Heinemann 1997), voltage-gated Na^+ channels (Benndorg and Koopmann 1993), and K_{ATP} channels (McLarnon and Hamman 1993).

Conformational entropy changes occur in molecular recognition, owing to protein interactions (Frederick, Marlow et al. 2007). Standard free energy, enthalpy, and entropy of the binding equilibrium of adensosine A1 receptor ligands were calculated by affinity

measurements carried out at different temperatures, and affinity was found to increase with temperature (Dalpiaz, Scatturin et al. 2000). This group concluded that binding of full and partial agonists is entropy-driven. There is an interconversion between inactive and active protein states that is typically described by two static structures. However, Pontiggia et al. (2015) suggest that functional states are defined by kinetics rather than structural terms. They conclude that the transition between active and inactive states occurs through multiple pathways, facilitated by a number of bonds, which lowers the transition barrier through entropic and enthalpic contributions (Pontiggia, Pachov et al. 2015). Yao et al. showed that activation by temperature involves large compensatory enthalpy and entropy changes with little free energy change (Yao, Liu et al. 2010). The Arrhenius model of kinetics can evaluate thermal damage and cell death processes for single-step, irreversible reactions (Pearce 2015).

Chapter 3 – Hypothesis and Goals of Present Work

3.1. Hypotheses

We hypothesize that, given the extensive bidirectional interactions between the gastrointestinal (GI) tract and central nervous system, significant changes resulting from heat stress on GI function demonstrated by our previous work will similarly manifest in olfactory sensory neurons. Additionally, previous work showed that pretreatment with probiotic species (*Bacillus subtilis*) prevented the adverse effects in the GI tract. Therefore, we hypothesize that pretreatment with this probiotic species may have similar protective effects on olfactory function.

3.2. Objective and Specific Aims

The objective of the work at present is to investigate the effects of temperature stress on olfactory function.

3.2.1. Specific Aim I

Determine whether olfactory epithelia extracted from animals exposed to heat stress for an extended period respond differently to odorant stimuli than that of control animals.

3.2.2. Specific Aim II

Extract olfactory epithelia from non-stressed animals under normal conditions and determine whether exposing the tissue itself to temperature changes has any effect on responses to odorant stimuli.

3.2.3. Specific Aim III

Determine whether pretreatment of animals with probiotics before undergoing heat stress affects olfactory function.

Chapter 4 – Materials and Methods

4.1. Materials

Male Sprague Dawley rats purchased from Harlan Laboratories weighing 250-300 grams were our research models. Animals were housed in the Veterinary Research Building in pairs under specific pathogen free conditions and allowed to acclimatize for two days prior to experiments at a temperature of 21±1°C, humidity of 50±5°C, and a 12-hour light/dark cycle with free access to water and standard food. Animals of this project were cared for by the Division of Laboratory Animal Health at Auburn University (DLAH), assuring compliance with all applicable regulations. The primary regulations governing the care and use of animals used in research and teaching include the following: Animal Welfare Act, the NIH-PHS Policy, the Guide for the Care and Use of Laboratory Animals, and the Guide for the Care and Use of Agricultural Animals in Agricultural Research and Teaching. Animal care technicians under the supervision of the animal research facility, DLAH, and College of Veterinary Medicine provided daily care and maintenance of the animals. Accountability for all animals and facilities used for teaching and research is evaluated annually via an unannounced inspection by the USDA, APHIS, and Animal Care Inspector. The following is a list of materials used for procedures carried out through the duration of our heat stress experiments.

4.1.1. Surgical Tools

The following tools and materials were used for the preparation of rat olfactory epithelia, along with proper protective equipment that meet laboratory safety guidelines. A 1-gallon plastic container with sealable lid, Isoflurane anesthetic, laboratory guillotine, surgical microscope, scalpel, scissors, fine scissors, rongeurs, and forceps were used for olfactory epithelial surgery.

4.1.2. Odorants

All odorants were purchased from Sigma-Aldrich. A stock standard odorant solution (SOS) containing ethyl butyrate, eugenol, and (+) and (-) carvone in water was prepared for use in each EOG experiment. During each EOG session, a 0.25s pulse of the odorant mixture was generated by a computer-controlled Pneumatic PicoPump PV800 (World Precision Instruments, Sarasota, FL). A pulse of positive pressure pushed the odorant into a glass nozzle toward the epithelial tissue at 20s intervals for data collection. A single EOG recording took 200s and contained 10 response traces.

4.1.3. EOG Equipment

For our heat stress experiments, we used the EOG method of electrophysiology for measurement of olfactory function. The EOG setup is composed of a perfusion chamber contained in a Faraday box, odorant delivery system utilizing micropipettes, measuring and recording electrodes, a desktop computer and monitor, and a video monitor for observation of microelectrode contact with the olfactory epithelial surface.

Images of our EOG set-up, perfusion chamber, and odorant delivery system are shown in **figure 17**. Odor-activated current clamped voltage responses are recorded as EOG with an integrating patch clamp amplifier (MultiClamp 700A Amplifier, Molecular Devices). The analog signal is filtered at 2-5 kHz and digitized using a digital converter. Data acquisition and subsequent storage and analysis of the data is carried out using pCLAMP software (Axon Instruments) and exported in ASCII format for analysis. EOG responses are analyzed to determine half-rise and half-decay times.

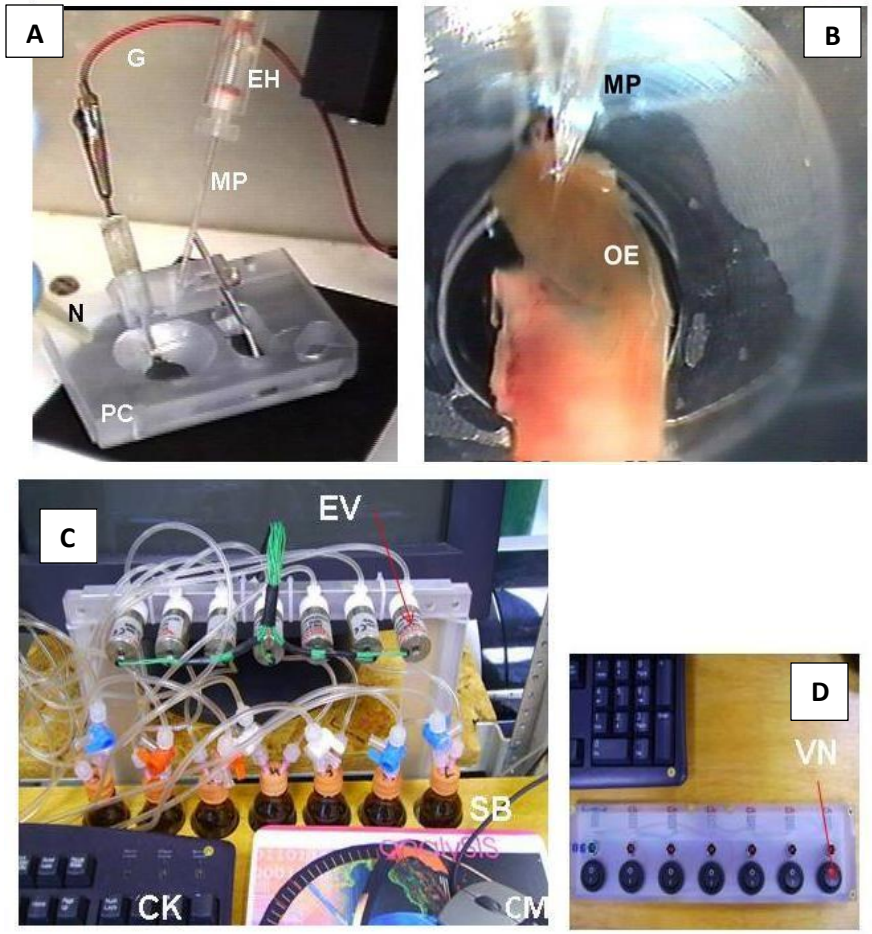

Figure 17. **EOG Measurement System.** ***(A)*** *Tissue perfusion chamber with specific instruments labeled: PC – perfusion chamber, EH – electrode holder, MP – glass micropipette with Ag/AgCl electrode, G – ground wire, N – nozzle for odorant delivery* ***(B)*** *Fragment of olfactory epithelium partially immersed in PBS. OE – the olfactory epithelium appears darker in comparison to respiratory epithelium.* ***(C)*** *Valve control system. EV – electric valves controlling stimuli delivery, SB – stimuli bottles containing odorant mixtures, CK – computer keyboard, CM – computer mouse* ***(D)*** *Control board with seven control buttons operating electric valves.*

4.1.4. Heat Stress Instruments

Environmental Chamber

An environmental chamber was purchased from Caron Products (Environmental Chamber 6020 – Caron, OH). The enclosures in which animals were housed were placed in the chamber for 25 minutes, at either 45°C (heat stress group) or 25°C (control group). Rectal temperature was measured with a thermometer before and after exposure.

Figure 18. Environmental Chamber. Rats within their housing enclosures were placed inside the environmental chamber at 45°C for 25 minutes and monitored for the duration of the heat stress exposure. Control animals were placed in the same location for the same duration, at 25°C.

Temperature Controlled EOG Perfusion Chamber

The normal EOG set consists of a stand-alone perfusion chamber, through which physiological buffer solution is circulated to maintain pressure consistency. The olfactory tissue is partially immersed in the buffer solution at all time throughout EOG experiments. A temperature controlling system was designed as a portion of the perfusion chamber. The temperature is set on a digital transmitter which alters the thermal properties of the perfusion chamber in which the epithelial tissue sits. Our temperature dependence experiments included a step-wise increase within the range of 16-34°C. Once

EOG signal stability was reached at a given temperature, the temperature would be raised a few degrees and the resulting recording was recorded.

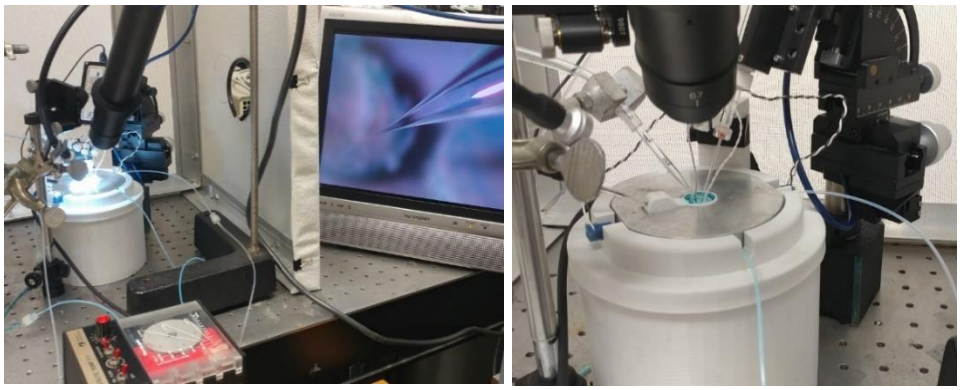

Figure 19. EOG Temperature Chamber. ***(A)*** *Temperature-controlled perfusion chamber connected to EOG apparatus.* ***(B)*** *Close up of perfusion chamber, showing recording electrode and glass micropipette in contact with olfactory epithelium and pressure controlling filtration system.*

Animal research treadmill

An exercise treadmill designed for biomedical and kinesiology research using rodent models was used for metabolic heat stress experiments. Animals were placed on an active treadmill for 25 minutes and rectal temperature was recorded before and after exposure. After 4 hours, olfactory epithelium was dissected for EOG analysis, and trunk blood was collected for biochemical analyses for concomitant work. The measured body temperatures coupled with EOG data were used for thermodynamic calculations.

Figure 20. Rodent Treadmill. *An exercise treadmill designed specifically for biomedical and kinesiology research using rodent models was used for metabolic heat stress experiments. In this forced exercise model, animals were placed on an active treadmill for 25 minutes. Rectal temperature was taken before and after exercise-induced stress, and biochemical parameters and EOG recordings were assessed after 4 hours.*

4.1.5. Probiotics

The *Bacillus subtilis* strain was selected for its wide spectrum antagonistic effects on pathogens and maintaining commensal microbes. *Bacillus subtilis* was cultured on Difco sporulation medium (DSM) at 37°C for 5 days. Bacteria were harvested by flooding the surface of the culture with sterile PBS and scraping with a sterile cell spreader. Obtained bacterial suspension was diluted to $1x10^8$ CFU/mL in PBS. Viability of bacteria is checked on DSM plates at 37°C for 24 hours.

4.2. Preparation of Epithelial Slice

Two to four rats were ordered weekly as needed for olfactory experiments. Within a ventilated fume hood, rats were placed in a sealed plastic container along with an anesthesia jar containing absorbent gauze soaked in 0.2ml isoflurane. Animals were exposed to the vapors of the anesthetic until anesthetized, determined by absence of response to toe and tail pinch techniques. After anesthesia, rats were rapidly decapitated with a laboratory guillotine.

To begin isolation of the nasal epithelial tissue, an incision was made along the dorsal midline of the head using a scalpel and scissors, while opening the tissue back on either side. The lower jaw was then removed using large scissors. The zygomatic arch and associated muscle tissue were removed along the eye. Rongeurs were used to remove bones along the dorsal end of the skull to provide access to the ethmoturbinates. The olfactory epithelium lining the nasal septum is fragile and easily torn. Care was taken to avoid damage. Fine scissors were used to cut through the ventral and dorsal portion of the mucosa. The same fine scissors were then used to cut through the septum and along the caudal aspect of the turbinates. The septum was then extracted using forceps and placed in a cell culture dish containing Hanks buffered saline solution (HBSS) with Ca^{2+} and Mg^{2+}. After surgical removal, the epithelial slice was placed in the EOG perfusion chamber.

To achieve maximum contact to the electrophysiological instruments, the specimen was partially immersed in the physiological buffer solution. The viability of the tissue and stability of responses were maintained for about 40-60 minutes when all EOG instrumentation were functioning properly, until steady and consistent EOG responses were achieved.

4.3. Experimental Groups and Design

Each method of heat stress followed by the respective olfactory analyses have been conducted throughout a series of experiments as animals, equipment, and personnel were available. We used three methods of heat stress. **1)** In the first method, animals were

exposed to a temperature of 45ºC in a climatic chamber for 25 minutes and rectal temperature was measured using an electronic thermometer before and after exposure. Olfactory function was assessed after 4 hours of acclimation, in order to allow time for potential biochemical responses and interactions to take place. **2)** The second method of heat stress included exercise-induced metabolic stress. Rats were placed on an exercise treadmill for 25 minutes, before and after which body temperature was measured. Olfactory function was assessed after 4 hours to again allow sufficient time for measurement of biochemical responses. Although these two forms of heat stress differed in method, the overall recorded body temperatures before and after exposure were the parameters used for thermodynamic calculations and evaluation. Future work will investigate more specific biochemical differences in blood serum from animals that were exposed to environmental heat stress and those that underwent metabolic stress. **3)** The third method of heat stress involved animals that did not undergo whole-body exposure to elevated temperatures prior to the isolation of epithelium. Dissected epithelia from these animals were then placed in a temperature controlled heat chamber specifically designed for attachment to the EOG, in which the temperature of the OE itself was manipulated during EOG between 16-34°C. All controls remained at room temperature (25°C).

The following **table 1** lists the experimental conditions presented in this dissertation, as well as some supplemental information regarding the exposure of control olfactory epithelium to probiotic treatment within the EOG perfusion chamber for the purpose of understanding whether pretreating rats with certain microbiota had any adverse effects on the tissue itself. This information is part of ongoing work that may later be incorporated in heat stress investigation. *Column one* "Animal No." lists the

animal number and *column two* "N traces" lists the number of EOG traces recorded from each respective olfactory tissue. Column three "Probiotic Pretreatment" indicates if animals were pretreated with probiotics, *column four* "Stress Environment" indicates environmental heat stress exposure, *column five* "Stress Metabolic" indicates metabolic stress exposure, and *column six* "Body Temp" contains the recorded animal temperature prior to epithelial extraction for EOG analyses. *Column seven* "Probiotic OE" indicates whether the olfactory epithelium itself was exposed to probiotic treatment within the perfusion chamber, and *column eight* "OE temp" lists the recorded epithelial temperatures within the temperature chamber.

Table 1. **Conditions of EOG Measurements**

[1]Animal No.	[2]EOG (N_{traces})	[3]Probiotic Pretreatment Rat	[4]Stress (Environment)	[5]Stress (Metabolic)	[6]Body Temp (°C)	[7]Probiotic OE [a]	[8]OE Temp (°C)
1	140	1 mL 10^8	+	-	39.8	-	25
2	140	1 mL 10^8	+	-	39.6	-	25
3	120	-	-	-	37.1	-	26-32
4	150	-	-	-	37.1	1-6 mL SBS/0	23
5	120	-	-	-	37.3	-	21-31
6	170	-	-	-	37.0	1-5 mL SBS/0	23
7	160	-	-	-	37.0	-	20-33
8	150	-	-	-	37.1	1-5 mL SBS/0	24
9	30	-	-	-	37.2	-	24-35
10	160	-	-	-	37	100-500 µL SBS/0	24-20
11	180	1 mL 10^8	-	+	39.4	-	23
12	180	1 mL 10^8	-	+	39.6	-	23
13	150	-	-	-	37.1	-	22
14	130	-	-	+	39.6	-	22
15	110	-	-	-	37.1	-	18-34
16	180	-	-	-	37.0	-	16-33
17	70	-	+	-	39.7	-	18-30
18	110	-	+		39.6	-	16-32

a. Probiotics added to the perfusion chamber at concentration of 10^9 1/mL

4.4. Methods of Heat Stress

In the first heat stress model (whole-body exposure + systemic acclimation) animals were exposed to 45°C for 25 minutes in a climatic chamber, with body temperatures recorded before and after this time. Control animals for this model experienced the same spatial environment, however they were kept at a room temperature of 25°C. Olfactory epithelia was dissected after 4 hours of acclimation at regular resting temperature, and responses were assessed using the EOG.

In the second heat stress model (exercise-induced metabolic stress) animals underwent 25 minutes of forced running on a specialized treadmill designed for metabolic research. Rectal temperature was measured before and after exercise. Olfactory epithelia were dissected after 4 hours of acclimation at regular resting temperature, and responses were assessed using the EOG.

The final heat stress model (direct tissue exposure) involved animals that did not undergo exposure to elevated temperatures prior to the isolation of olfactory epithelium (OE). Immediately following surgical dissection, the tissue was then placed in a temperature controlled heat chamber specifically designed for attachment to the EOG, in which the temperature of the OE itself was manipulated during assessment. The temperature within this perfusion chamber was regulated in a step-wise manner, within the 16– 34°C range. The physical nature of olfactory function temperature dependency was assessed in this model.

A part of our assessment of the physical effects of heat stress included histological analyses of olfactory epithelium following heat stress. Tissue included in this analysis were taken from animals that had either undergone heat stress in the form of

prolonged exercise or normal controls. The tissue was then placed in the EOG perfusion chamber while electrical responses were recorded at increasing temperatures. Following EOG analyses, the tissue was then prepared for immunohistochemistry, staining for olfactory marker protein (OMP) in order to analyze the distribution and morphology of olfactory sensory neurons.

4.5. Probiotic Administration

Bacillus subtilis BSB3 (10^8 CFU in 1 milliliter of PBS per rat) or 1 milliliter physiological buffer solution (PBS) control was administered to all animals by oral gavage. Probiotic or PBS pretreatments occurred twice a day for two days prior to heat stress, with 6 hours between doses.

4.6. Statistical Analysis

EOG data acquisition and subsequent storage and analysis was carried out using pCLAMP software (Axon Instruments) and exported in ASCII format for graphical representation. Data averaging, ANOVA, t-test, curve fitting, and graph plotting were carried out using Origin 2015 (Northampton, MA) and 2010 Microsoft Excel.

4.7. Thermodynamic Calculations of EOG Measured at Different Temperatures

The electroolfactogram (EOG) represents the sum of generator potentials of olfactory receptor neurons. EOG can be recorded by an electrode placed on the surface of the olfactory mucosa as the mucosa is subjected to an odorous stimulus (Scott and Scott-Johnson 2002). The odorant (O) interacts with the receptor-G-protein complex (RG_{olf}).

This interaction causes dissociation of G_{α}. One of the components of G_{olf} complex (the Gα subunit) activates an adenylyl cyclase (AC) that generate cAMP. Molecules of cAMP activate cyclic nucleotide gated (CNG) channels allowing influx of depolarizing Ca^{+2}-ions. In turn, Ca^{+2}-ions open $Cl_{channels}$ and allow efflux of Cl^{-}-ions that further contributes to depolarization of membrane. The ion currents $I^{Ca+2}+I^{Cl-}$ produce generator potential and the sum of generator potentials of olfactory sensory neurons represents EOG. We suggest that the time of the activation and deactivation during the initial events in olfaction can be characterized by half rise (τ_r) and half-decay (τ_d) times of EOG, shown in **figure 21**.

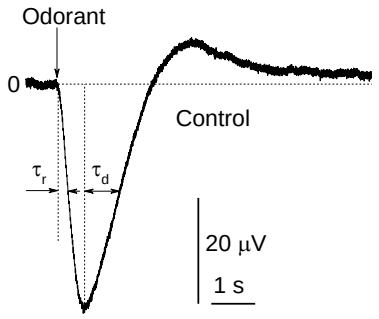

Figure 21. Representative EOG trace from dissected rat olfactory epithelium. *The EOG signal usually increases to attain a maximal level and decays to the original value. The half-rise time is defined as the time required to reach half of the maximal amplitude. The half-decay time is defined as the time needed for the EOG signal to decay from the maximum level to half of maximal amplitude.*

Therefore, the half-time of the total time of activation – deactivation:

Equation 1. Half of total time activation-deactivation

$$\tau = \tau r + \tau d \quad (1)$$

For simplicity, we interpret the inverse time, 1/τ, as the first-order rate constant, k, characterizing the overall process of activation-deactivation:

Equation 2. First-order rate constant

$$k = 1/\tau \tag{2}$$

A similar approach was taken for thermodynamic analysis of ion channels (Brauchi, Orio et al. 2004; Nache, Kusch et al. 2008; Gupta and Auerbach 2011). Plotting the right-hand side of **Equation 2** versus time yields an estimation "k" from the slope. The Arrhenius equation (Segel 1975) can be used to express the temperature dependence of the first-order activation kinetics.

The activation energy of the process can be estimated by using the Arrhenius equation (Segel 1975):

Equation 3. Arrhenius Equation

$$k = Ae^{-\frac{E_a}{RT}} \tag{3}$$

where R is the universal gas constant, E_a represents the apparent activation energy, and A -- the pre-exponential Arrhenius factor. Taking the logarithm of **Equation 3** yields:

Equation 4. Logarithm of Arrhenius Equation

$$\log k = -\frac{E_a}{2.303R} \times \frac{1}{T} + \log A \tag{4}$$

If the logarithm of k in **Equation 4** is plotted against the reciprocal of temperature, 1/T, then the slope of this graph yields the activation energy (E_a), the thermal activation of olfactory receptors. The rate constant depends on the thermodynamic activation

parameters of this transition state and can be described by the Eyring equation (Eyring, Lin et al. 1980):

Equation 5. Eyring Equation

$$k = \frac{k_b T}{h} e^{-\frac{\Delta G}{RT}} = \frac{k_b T}{h} e^{\frac{\Delta S}{R}} e^{-\frac{\Delta H}{RT}} \quad (5)$$

where *k* is the rate constant, ΔG is the standard Gibbs free energy of activation, h is Planck's constant, ΔS is the standard entropy of activation, ΔH is the standard enthalpy of activation, k_b is the Boltzmann constant, R is the gas constant, and *T* is the absolute temperature in Kelvin. Taking the logarithm of both sides of **Equation 5** one obtains:

Equation 6. Logarithm of Erying Equation

$$\log\left(\frac{k}{T}\right) = \log\left(\frac{k_b}{h}\right) + \frac{\Delta S}{2.303R} - \frac{\Delta H}{2.303R} \times \frac{1}{T} \quad (6)$$

If the plot of the left-hand side of **Equation 6** versus *1/T* is linear, one can compute the value of *ΔH* from the slope, *ΔS* from the ordinate intercept and the Gibbs free energy of activation by the relation:

Equation 7. Gibbs Free Energy of Activation

$$\Delta G = \Delta H - T\Delta S \quad (7)$$

From **Equation 3** we can define the energy of activation as:

Equation 8. Energy of Activation

$$E_a = -R \frac{\partial \ln k}{\partial\left(\frac{1}{T}\right)} \quad (8)$$

The substitution of *k* in **Equation 8** with the k equivalent relation in **Equation 5** and differentiation of this new expression with respect to *1/T* shows that the Arrhenius **Equation 3** and the Eyring **Equation 5** expressions can be related as:

Equation 9. Relation between Arrhenius and Eyring Equations

$$E_a = \Delta H + RT \tag{9}$$

Equation 10. Relation between Arrhenius and Eyring Equations

$$A = (\frac{ek_bT}{h})e^{\frac{\Delta S}{R}} \tag{10}$$

Taking the logarithm of both sides of **Equation 10**, one obtains:

Equation 11. Linear Relation between the Log of Arrhenius Frequency factory and Entropy of Activation

$$\log A = \log(\frac{ekT}{h}) + \frac{\Delta S}{2.303R} \tag{11}$$

suggesting a linear relation between the logarithm of the Arrhenius frequency factor and entropy of activation obtained from the Eyring equation for the transitional state.

The first-order kinetic model was used to determine the best fit for the data with the calculated rate constant *k*. The Arrhenius and Eyring equations were then applied to the data to determine E_a, *A*, ΔG, ΔH, and ΔS of the temperature-dependent viability transitions.

For two temperature points T_1 and T_2 it follows from **Equation 4** that:

Equation 12

$$E_a = \frac{2.303T_1T_2 log\frac{k_2}{k_1}}{T_2 - T_1} \tag{12}$$

Equation 13

$$logA = \log k_1 + \frac{E_a}{2.303R} \times \frac{1}{T_1} = \log k_2 + \frac{E_a}{2.303R} \times \frac{1}{T_2} \tag{13}$$

Substituting *logA* in **Equation 13** from **Equation 11** it follows that entropy:

Equation 14. Entropy

$$\Delta S = 2.303R\left[logA - log\frac{k_b}{h} - log(eT)\right] \quad (14)$$

Enthalpy ΔH is found from **Equation 5** as

Equation 15. Enthalpy

$$\Delta H = E_a - RT \quad (15)$$

Using ΔS from **Equation 14** and ΔH from **Equation 15**, the Gibbs free energy of activation is calculated from **Equation 7.**

It was shown that perceived odorant intensity to be proportional to the area under the EOG time curve (Lapid, Seo et al. 2009; Lapid and Hummel 2013). Significantly, EOG amplitude is linked to the percentage of reactive ORNs (Koce and Valentincic 2000). Therefore, we suggest that the relative change of the area under EOG time curve per second at different temperatures is proportional to the rate constant. The area under EOG time curve (s_i) is measured at the consecutive steady states at temperatures (T_i) at times (t_i):

Equation 16

$$si, sii, \ldots\ sn \quad (16)$$

Equation 17

$$Ti, Tii, \ldots\ Tn \quad (17)$$

Equation 18

$$ti, tii, \ldots\ tn \quad (18)$$

Then change of area, temperature, and time can be estimated as following:

Equation 19

$$\Delta si\ =\ sii - si, siii - sii, \ldots sn - sn - 1 \quad (19)$$

Equation 20

$$\Delta Ti = (T2 - T1)/2, (T3 - T2)/2 \ldots (Tn - Tn - 1)/2 \quad (20)$$

Equation 21

$$\Delta ti = t2 - t1, t3 - t2, \ldots tn - tn - 1 \quad (21)$$

The relative change of area per second at temperatures T_i can be estimated from **equations 19-21:**

Equation 22

$$(\Delta si/\Delta sn)/\Delta ti \approx ki \quad (22)$$

where k_i is the rate constant at the temperature T_i.

If values of log k_i calculated from experimental EOG data by using **Equation 22** are plotted as the function of $1/T_i$, we get the Arrhenius presentation of the rate constant **Equation 4.**

The EOG traces were recorded with isolated olfactory epithelia (Viswaprakash, Dennis et al. 2009) at the steady state temperature conditions and the transient conditions when temperature grows (or decreases) slowly from one to another level (**Figure 22**,**Table 1**).

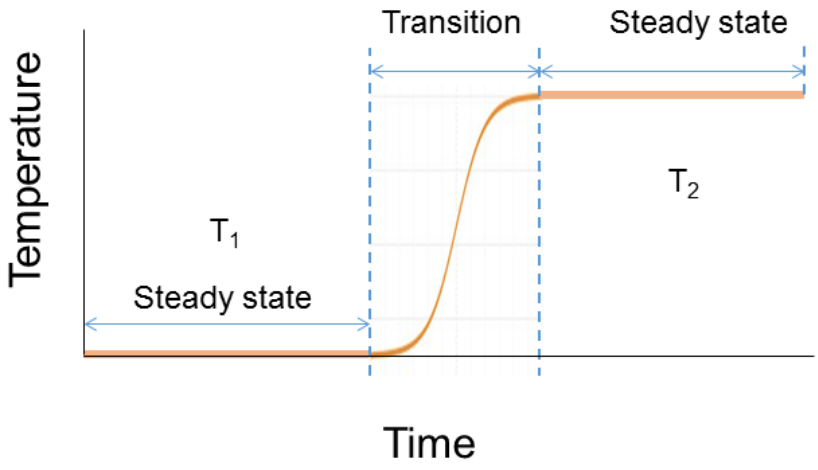

Figure 22. Schematic diagram of the environmental temperature change in experiments with olfactory epithelium in the temperature control chamber. *The OE is kept at constant temperature T_1 for ~15 minutes, then the temperatures are increased from T_1 to T_2 with rate of ~1.5 degree/minute, and next at the constant temperature (T_2) again for ~15 min. The OE is in the steady state at the stable temperature, or in the slow transition from the state 1 to state 2.*

The half-rise (τ_r) and half-decay time (τ_d) for a single EOG trace were measured as shown in **Figure 21**, and the rate constant was estimated using

Equation 1 and **Equation 2.** The mean values of half-rise and half-decay times at certain temperature were taken to represent kinetics activation and deactivation, respectively. The multiple values of half-rise and half-decay times at two steady state temperatures are better represented by EC50 values of the cumulative frequency distributions than the mean values alone. Similarly, the EC50 values of the cumulative frequency distributions of rate constant were used to characterize the overall activation-deactivation at two temperatures.

Chapter 5 – Results

5.1. Whole-Body Heat Stress Increased Kinetics of Olfactory EOG Responses

Exposure of rats to high temperatures resulted in a significant increase of body temperature. The mean body temperatures before and immediately after heat stress were 36.7±0.07 ^{o}C and 40.3 ±0.17 ^{o}C, respectively. Kinetic properties of electrical responses to odorants have been calculated on the isolated epithelia from rats undergoing our three heat stress models. Kinetics were significantly changed in animals subjected to environmental and metabolic heat stress. The mean half-rise (t_r) and half-decay times (t_d) of control OE were 328±11 and 660±20 ms, respectively. The rise and decay of EOG peak amplitude after heat stress were much faster. The t_r and t_d reduced by 175%, and 72%, respectively. Representative EOG recordings from heat stressed and control animals are shown in **figure 23** a and b, respectively. The cumulative distribution of receptor activation half-rise and half-decay times are shown in figure 21, c and d, respectively.

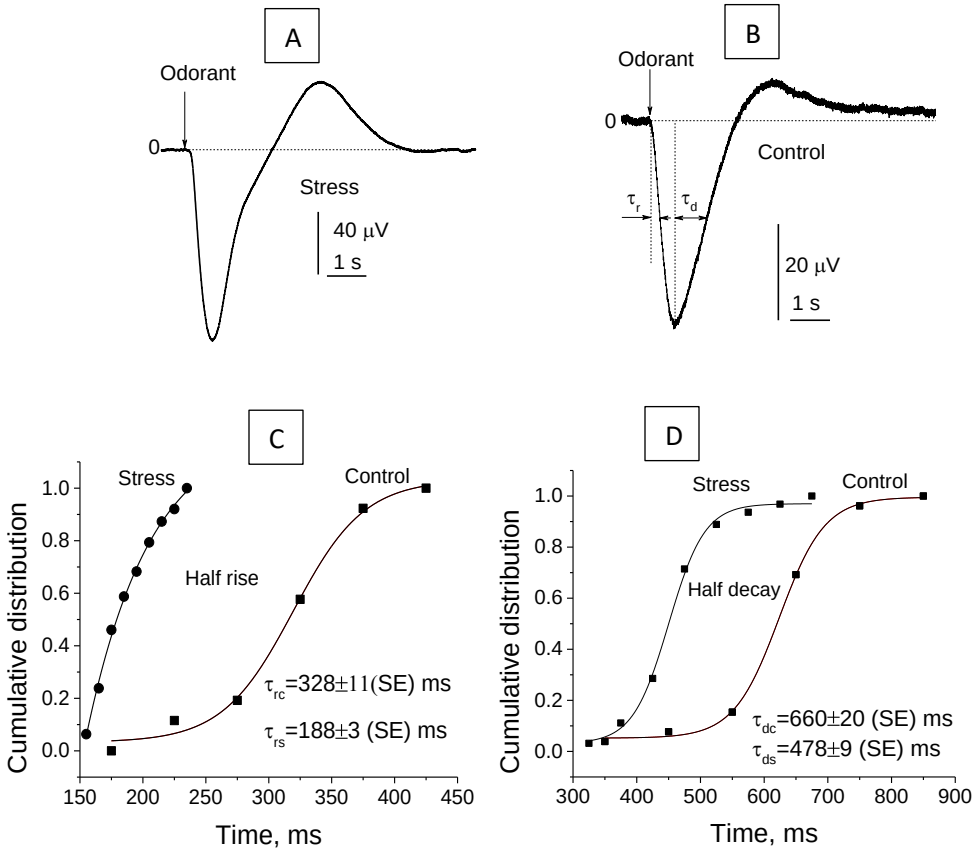

Figure 23. Representative EOG recordings and cumulative distribution of reactive olfactory sensory neurons in the epithelia of rats exposed to heat stress and control rats. ***A)*** *Representative EOG recording of control animal olfactory epithelia. Mean half-rise (T_r) is described as the time is takes for epithelium to reach half maximal EOG peak, and half-decay (T_d) the described as the time it takes for epithelium to return to half-maximal EOG peak towards baseline potential.* ***B)*** *Representative EOG recording of stressed animal olfactory epithelia. Tr and Td are calculated the same as previous figure.* ***C)*** *Cumulative distribution of activation time, calculated as half-rise time, of olfactory epithelia from stress and control animals.* ***D)*** *Cumulative distribution of deactivation time, calculated as half-decay time, olf epithelia from stress and control animals.*

5.2. Pre-treatment with Probiotics Reversed Response Kinetic Effects

Previous work has demonstrated the efficacy of probiotics, namely *Bacillus subtilis*, in the prevention of intestinal complications resulting from heat stress. The results from this work were presented in chapter 2, section 2.5.3. Animals that were pretreated with probiotics prior to exposure to temperature elevation showed significant reduction in adverse morphological changes and biochemical parameters in comparison to control animals that were pretreated with PBS. We assessed whether probiotic pretreatment could also affect olfactory function.

This experiment included three total groups. Animals subjected to heat stress were either pretreated by oral gavage with probiotic strain, *Bacillus subtilis*, or treated with control PBS prior to heat stress. Four hours following the exposure to heat stress, olfactory epithelia were dissected and electrical responses to odorant stimulation were evaluated by EOG. Both stress groups were compared to control animals that were not exposed to heat stress conditions. An EOG recording measures the summation of generator potentials of many olfactory sensory neurons at the epithelial surface. A typical EOG response curve shows an electronegative rise to a peak value, and then a decay to baseline membrane potential. We found that pretreatment with probiotics resulted in a kinetic shift of half-rise and half-decay times towards control animals. **Figure 24** shows the changes in cumulative distribution of olfactory sensory neuron activation and deactivation, described by half-rise (a) and half-decay (b) times.

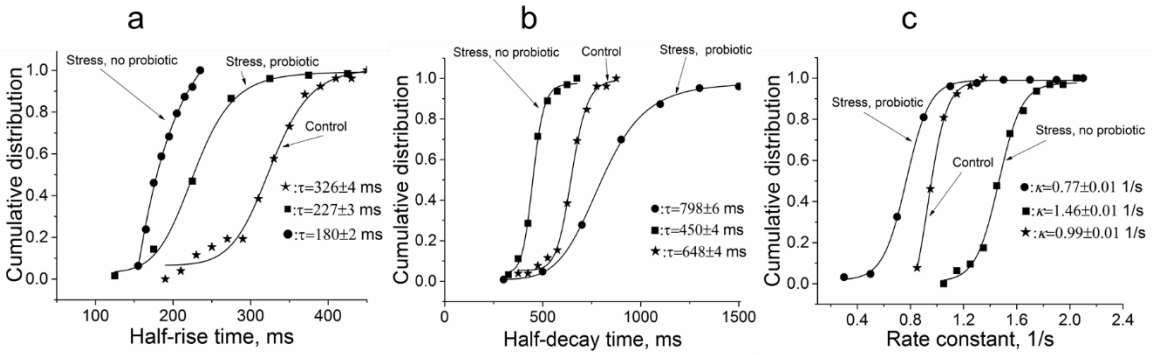

Figure 24. Kinetic shifts in cumulative distribution of olfactory neuron activation and deactivation. ***(A)*** *Mean half-rise times, representative of the time required to reach half maximal amplitude of EOG response.* ***(B)*** *Mean half-decay times, representative of the time required to return to half maximal amplitude.*

In **figure 24A**, the olfactory epithelia dissected from control animals showed a cumulative half-rise time of 326±4ms. Heat stressed animals that were not treated with probiotics demonstrated a kinetic shift in half-rise time of 180±2ms. Heat stressed animals that were pretreated with probiotics demonstrated a shift towards the kinetics of control animals, with a cumulative half-rise time of 227±3ms. **Figure 24B** represents the kinetics of half-decay times. Olfactory epithelia dissected from control animals showed a cumulative half-decay time of 648±4ms. Heat stressed animals that were not treated with probiotics demonstrated a kinetic shift in half-decay time of 450±4ms. Heat stressed animals that were pretreated with probiotics demonstrated a significant increase in decay time, exceeding that of controls, with a cumulative half-decay time of 798±6ms. **Figure 24C** represents the cumulative distribution of calculated rate constants of activation and deactivation between heat stressed animals pretreated with probiotics, heat stressed animals treated with PBS, and control animals that did not undergo. The cumulative

distribution of rate constants for olfactory epithelia dissected from control animals was 0.99 ± 0.01^{-s}. The cumulative distribution of rate constants for olfactory epithelia dissected from heat stressed animals treated with PBS was 1.46 ± 0.01^{-s}. A shift in rate constant was seen in the cumulative distribution of stressed animals that were pretreated with probiotics, exhibiting an average rate constant of 0.77 ± 0.01^{-1}.

The amplitude characteristics of relative EOG responses were also analyzed for comparison between these groups, shown in **figure 25**. Amplitude height is a measure from baseline voltage to peak voltage. **Figure 25A** shows the average amplitude heights, measured in μV, in heat stressed animals that were either treated with PBS (no probiotic) or *Bacillus subtilis* (probiotic). Heat stressed animals that were not treated with probiotics had EOG responses with an average amplitude of 3.2μV, while heat stressed animals that were pretreated with probiotics had a much higher average amplitude of 11μV. The area under an EOG curve is a representative measure of the number of activated olfactory sensory neurons within the vicinity of the point of contact. **Figure 25B** shows the average area under EOG curves for heat stressed animals pretreated with PBS (no probiotic) or *Bacillus subtilis* (probiotic). The no probiotic group had an average area under EOG curves of 5.4mV/ms, while the probiotic group had a significantly greater area under EOG curves of 13.8mV/ms. **Figure 25C** represents the cumulative distribution of calculated rate constants of activation and deactivation between heat stressed animals pretreated with probiotics and heat stressed animals treated with PBS.

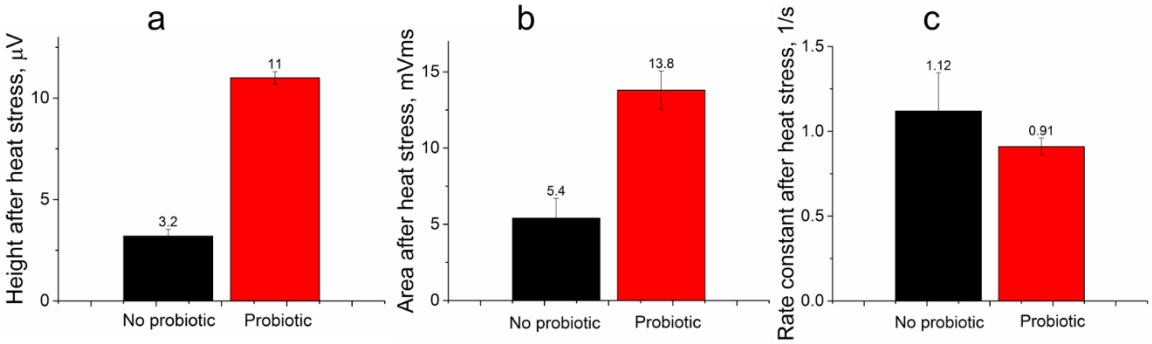

Figure 25. EOG Amplitude and Area Under Curve. *Amplitude height and, specifically, the area under the curve is a measure of the number of olfactory sensory neurons that are activated, and thus a measure of olfactory function. Black bars represent heat stressed animals that were treated with PBS (no probiotics). Red bars represent heat stressed animals that were treated with Bacillus subtilis (probiotics). A) Average height of EOG recordings from the animals without probiotic pretreatment was 3.2µV, while animals with probiotic pretreatment was 11 µV. B) Average area under EOG curves for animals without probiotic pretreatment was 5.4mVms, while animals with probiotic pretreatment was 13.8mVms. C) Average rate constant of activation and deactivation of olfactory receptors in OE taken from heat stressed animals without probiotic pretreatment was 1.12 1/s, and slightly slower in animals that were pretreated with probiotics, measured at 0.91 1/s.*

5.3. Temperature Dependence of Dissected Olfactory Epithelium

In this heat stress model, olfactory epithelium was dissected from rats that were kept under normal environmental conditions. The epithelial tissue was then placed in the EOG perfusion chamber specially designed for the function of controlling temperature of the buffer solution and tissue contents within it. OE within the temperature-controlled EOG chamber were exposed to increments ranging from 16-34ºC. Under stable conditions, olfactory epithelia responded to a 0.25-second pulse of odorant vapor by generating electronegative EOG responses that were synchronized with stimulus onset. Typical EOG responses at different temperatures (20ºC, 25ºC, 30°C, and 34ºC) are shown in **figure 26.**

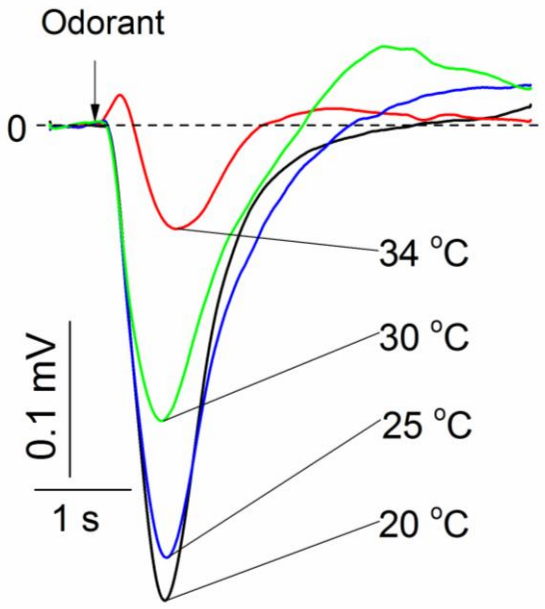

Figure 26. Representative EOG traces from dissected rat olfactory epithelium recorded at increasing temperatures. *Representative recording when perfusion chamber was at a steady state of 20°C (black), steady state of 25°C (blue), steady state at 30°C (green), and steady state at 34°C (red).*

5.4. Thermodynamic Analysis of EOG Recordings

5.4.1. Arrhenius Plot

Figure 27 shows an Arrhenius plot of experimental EOG recordings at steady state temperatures within a temperature range of 21-31ºC for the rate constant.

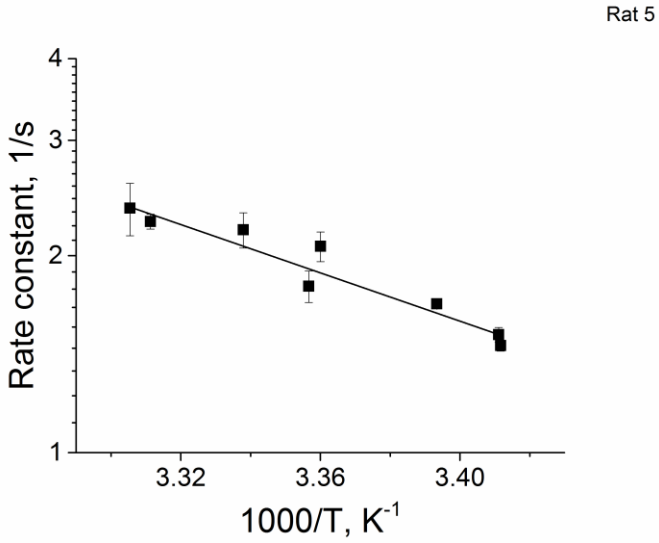

Figure 27. Arrhenius Plot. *The points are experimental data obtained at the temperature range 21-31 °C and plotted by using equation (5); the line is a linear regression: R-Square 0.93, Intercept 6.47±0.62; Slope -1.84±0.18. Data collected from one epithelium, 12 recordings, 120 EOG traces.*

The energy of activation E_a can be calculated directly from **Equation 4** using the value of the Arrhenius slope **(-1.84±0.18):**

$$E_a = -2.3R(\text{slope}\times 10^3) = -2.3\times 1.98(-1.84\times 10^{3)} = 8379 \text{ cal/mol}$$

$$E_a = 8.4\pm 0.8 \text{ kcal/mol}$$

The entropy change, ΔS, at 25°C, can be obtained from the value of the intercept of the Arrhenius plot **(6.47±0.62)** by using **Equation 11:**

$$\Delta S = 2.3R[\log A - \log(k_b/h) - \log(eT)] = 2.3\times 1.98(6.47-10.32-2.91)$$

$$\Delta S = -30.8\pm 2.0 \text{ calK}^{-1}\text{mol}^{-1}$$

The enthalpy, ΔH, at 25°C is calculated by **Equation 9:**

$$\Delta H = E_a - RT = 8379 - 590 = 7789 \text{ cal/mol}$$

$$\Delta H = 7.8\pm 0.7 \text{ kcal/mol}$$

The energy contribution due to the entropy change at 25°C is equal to:

$$T\Delta S = 298(-30.78) = -9172 \text{ cal/mol}$$

$$T\Delta S = -9.2 \pm 0.8 \text{ kcal/mol}$$

The Gibbs free energy change, ΔG, is calculated by **Equation 7:**

$$\Delta G = \Delta H - T\,\Delta S = 7789 + 9172 = 17962 \text{ cal/mol}$$

$$\Delta G = 16.9 \pm 1.2 \text{ kcal/mol}$$

The variables of E_a, ΔH, ΔS, $T\Delta S$, and ΔG for this epithelium and for three more epithelia representative of changing temperature conditions are shown in **Table 1**.

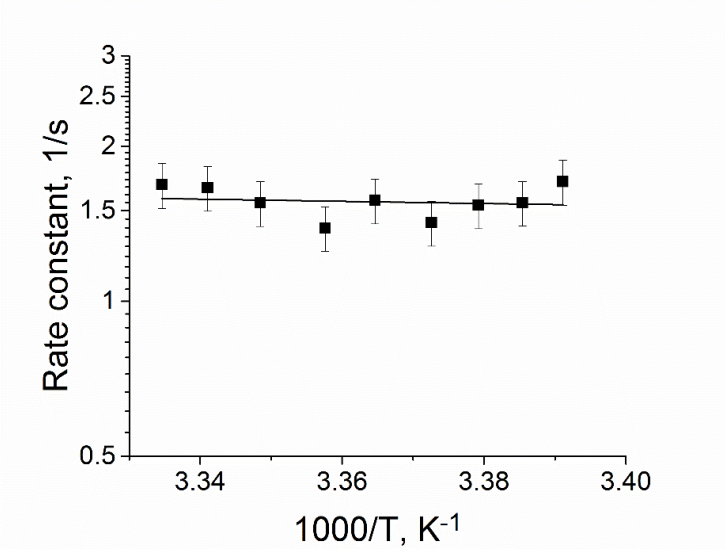

Figure 28. Arrhenius plot of experimental EOG recordings at the transient temperatures in a range of 22-28°C for the rate constant. *The temperatures that are increased from 22 oC to 28 oC 2 with rate of ~1.5 degree/minute. The line is a linear regression: R-Square -0.12, Intercept 0.9±2.0; Slope -0.2±0.6. Data collected from one epithelium, 1 recordings, 10 EOG traces.*

Figure 28 shows an Arrhenius plot **Equation 4** of experimental EOG recordings at the transient temperatures ranging from **22-28°C** for the rate constant. From the

Arrhenius equation the thermodynamic variables of this transient temperature transition can be calculated.

$$E_a = -2.3R(\text{slope}\times 10^3) = 2.3\times 1.98(-0.2\times 10^3) = 911 \text{ cal/mol}$$

$$E_a = 0.9\pm 2.0 \text{ kcal/mol}$$

$$\Delta S = 2.3R[\log A - \log(k_b/h) - \log(eT)] = 2.3\times 1.98(0.9-10.32-2.91)$$

$$\Delta S = -59.3\pm 140 \text{ calK}^{-1}\text{mol}^{-1}$$

$$\Delta H = E_a - RT = 911-590 = 321 \text{ cal/mol}$$

$$\Delta H = 0.3\pm 1.0 \text{ kcal/mol}$$

The energy contribution due to the entropy change at 25^{o}C is equal to:

$$T\Delta S = 298(-59.3) = -17671 \text{ cal/mol}$$

$$T\Delta S = -17.7\pm 30 \text{ kcal/mol}$$

The Gibbs free energy change, ΔG, is calculated by **Equation 7:**

$$\Delta G = \Delta H - T\,\Delta S = 321+17671 = 17992 \text{ cal/mol}$$

$$\Delta G = 18.0\pm 30 \text{ kcal/mol}$$

The variables of E_a, ΔH, ΔS, $T\,\Delta S$, and ΔG for this epithelium are shown in **table 2.**

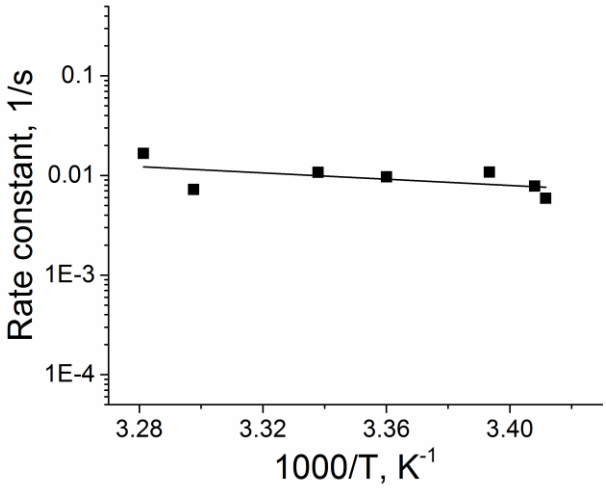

Figure 29. Arrhenius plot of experimental EOG recordings at the steady state temperatures in a range of 21-29oC for the rate constant. *The values of log k calculated from experimental EOG data by using Eq. (22) are plotted as the function of 1000/T. The line is a linear regression: R-Square 0.2, Intercept 3.25±3.5; Slope -1.6±1.0. Data collected from one epithelium, 12 recordings, 120 EOG traces.*

Figure 29 shows an Arrhenius plot of experimental EOG recordings at the steady state temperatures ranging from **21-29ºC** for the rate constant. The rate constants calculated are calculated using **Equation 22**:

$$E_a = -2.3R(\text{slope}\times 10^{3}) = 2.3\times 1.98(-1.6\times 10^{3)} = 7286 \text{ cal/mol}$$

$$E_a = 7.3\pm 3.0 \text{ kcal/mol}$$

$$\Delta S = 2.3R[\log A - \log(k_b/h) - \log(eT)] = 2.3\times 1.98(3.25-10.32-2.91)$$

$$\Delta S = -45.4\pm 5.0 \text{ calK}^{-1}\text{mol}^{-1}$$

$$\Delta H = E_a - RT = 7286-590 = 6696 \text{ cal/mol}$$

$$\Delta H = 6.7\pm 3.0 \text{ kcal/mol}$$

The energy contribution due to the entropy change at 25ºC is equal to:

$$T\Delta S = 298(-45.4) = -13529 \text{ cal/mol}$$

$$T\Delta S = -13.5 \pm 0.4 \text{ kcal/mol}$$

The Gibbs free energy change, ΔG, is calculated by **Equation 7:**

$$\Delta G = \Delta H - T\,\Delta S = 6696 + 13529 = 20225 \text{ cal/mol}$$

$$\Delta G = 20.2 \pm 9.0 \text{ kcal/mol}$$

These variables of E_a, ΔH, ΔS, TΔS, and ΔG are shown in **table 2.**

5.4.2. Cumulative frequency distributions of EOG rate constant at two temperatures

By using equations (1) and (2) the thermodynamic variables E_a, ΔH, ΔS, T ΔS, and ΔG for the activation–deactivation can be calculated from the experimental data. The half- rise and half-decay times of EOG at two steady state temperatures are also calculated.

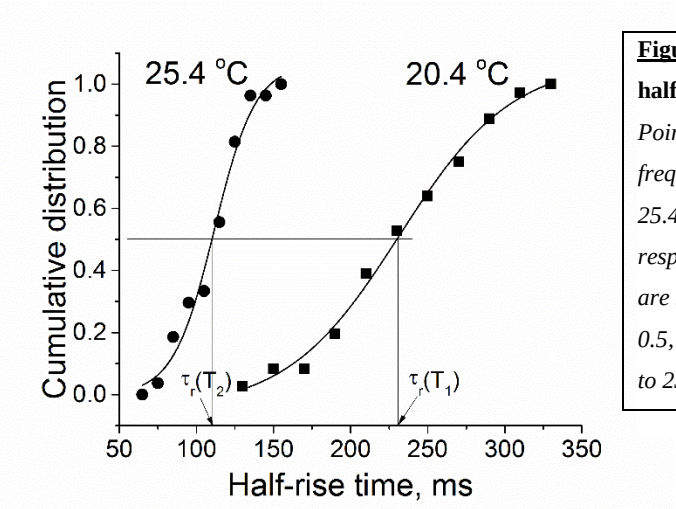

Figure 30. Cumulative distribution function of half-rise time at two steady state temperatures. *Points are the half-rise times obtained by using frequency distribution at temperatures 20.4 and 25.4°C. 60 and 40 experimental rise time points, respectively, were used in our calculations. Lines are sigmoidal fits. At the cumulative distribution of 0.5, the half-rise times ($\tau_r(T_1)$ and $\tau_r(T_2)$) are equal to 231.6 and 111.7ms, respectively.*

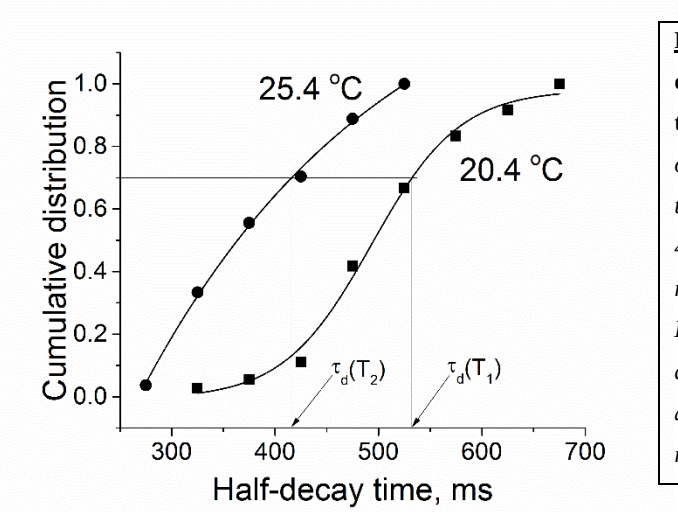

Figure 31. Cumulative distribution function of half-decay time at two steady state temperatures. *Points are the half-decay times obtained by using frequency distribution of times at temperatures 20.4 and 25.4°C. 60 and 40 experimental decay times points, respectively, were used in our calculations. Lines are sigmoidal fits. At the cumulative distribution of 0.5, the half-rise times ($\tau_d(T_1)$ and $\tau_d(T_2)$) are equal to 532.2 and 416.2 ms, respectively.*

Figure 30 shows cumulative distribution function of half-rise time at the steady state temperatures of 20.4±0.3 and 25.4±1.0^{o}C. At the cumulative distribution of 0.5, the half-rise times are equal to 231.6±4.6 and 111.7 ±3.0ms, respectively. The half-rise time at 25.4^{o}C is significantly faster than the half-rise time at 20.4^{o}C at the 0.05 level [t(26)=22.5, p=0.0; F(1, 61)=160, p=0.0]. The cumulative distribution functions of half-decay time at the steady state temperatures of 20.4±0.3 and 25.4±1.0^{o}C are shown in **figure 31.** At the cumulative distribution of 0.5, the half-decay times are equal to 532.2±5.6 and 416.2 ±4.5 ms, respectively. The half-decay time at 25.4^{o}C is significantly

faster than the half-decay time at 20.4°C at the 0.05 level [t(26)=8.25, p=0.0; F(1, 61)=38.7, p=0.0].

Figure 32 shows the cumulative distribution function of rate constant at two steady state temperatures. Points are the rate constant times obtained by using frequency distribution of rate constant at temperatures 20.4 and 25.4°C. Taken from the rate constant cumulative distributions we have the values of k_1=1.3 1/s and k_2=1.8 1/s at temperature T_1=293.4 K and T_2=298.4 K.

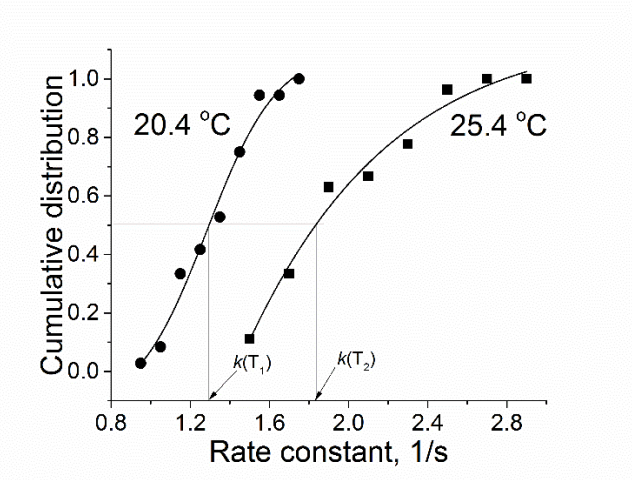

Figure 32. Cumulative distribution function of rate constant at two steady state temperatures. *Points are the rate constant times obtained by using frequency distribution of rate constant at temperatures 20.4 and 25.4°C. 60 and 40 experimental rate constant points, respectively were used in our calculations. Lines are sigmoidal fits. At the cumulative distribution of 0.5, the rate constant (*$k(T_1)$ *and* $k(T_2)$*) are equal to 1.3 and 1.8 1/s, respectively.*

Using **Equation 12** and values from **figure 32**, we can calculate the activation energy, E_a:

$$E_a = \log(1.8/1.3)\times(2.3\times293.4\times298.4)/5=6078 \text{ cal/mol}$$

$$E_a = 6.1\pm02 \text{ kcal/mol}$$

From **Equation 13** we have:

$$\log A_1 = \log 1.3 + 6078/2.3 \times 1.98 \times 293.4 = 4.7$$

$$\log A_2 = \log 1.8 + 6078/2.3 \times 1.98 \times 298.4 = 4.7$$

From **Equation 14** we have:

$$\Delta S = 2.3 \times 1.98(4.7-13.23) = -38.8 \pm 3.0 \text{ calK}^{-1}\text{mol}^{-1} \text{ (at T=24 }^{o}\text{C)}$$

$$T\Delta S = 298 \times (-38.8) = -11562 \text{ cal/mol}$$

$$T\Delta S = -11.6 \pm 0.8 \text{ kcal/mol}$$

According to **Equation 15:**

$$\Delta H = 6078-590 = 5488 \text{ cal/mol}$$

$$\Delta H = 5.5 \pm 0.4 \text{ kcal/mol}$$

From **Equation 7** we have:

$$\Delta G = 5488+11562 = 17050 \text{ cal/mol}$$

$$\Delta G = 17.1 \pm 1.1 \text{ kcal/mol}$$

The variables of E_a, ΔH, ΔS, $T\Delta S$, and ΔG for this epithelium and for five more epithelia are shown in **Table 2.**

5.4.3. Thermodynamic correlates of activation-deactivation of olfactory responses to odorants

Enthalpy changes (ΔH) were plotted as a function of entropy contribution (TΔS) and fitted to a single line that corresponds to the equation $\Delta H = \Delta G_o + T\,\Delta S$, where ΔG_o=17.6 ±1.4 kcal/mol and slope =1.01±0.08 **(figure 33).**

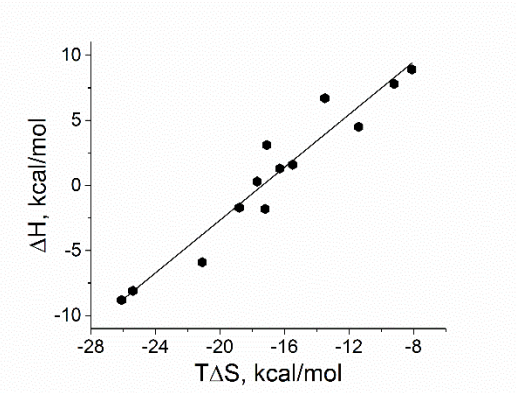

Figure 33. Thermodynamic correlation of enthalpy and entropy contribution for activation and deactivation of olfactory response. *TΔS values were taken from Table 2 (column "Entropy contribution TΔS, kcal mol^{-1}"), ΔH values were from the column "Enthalpy, ΔH, kcal mol^{-1}"). The points are experimental data from Table 2 while a line is a linear regression: R-Square=0.92; Intercept=17.6±1.4 kcal/mol; Slope=1.01±0.08.*

The averages of all thermodynamic variables from the presented experiments shown in **table 2** are as follows:

E_a = 1.7±1.4 (SE) kcal/mol

ΔH = 0.7±1.4 (SE) kcal/mol

ΔS = -54.9±4.4 (SE) cal mol^{-1}K^{-1}

TΔS = -16.7±1.2 (SE) kcal/mol

ΔG = 17.2±0.3 (SE) kcal/mol

Table 2. **Thermodynamic analysis of EOG of isolated olfactory epithelium at elevated temperatures**

Method	Rat # No	T, ^{o}C	Activation energy, E_a Kcal.mol^{-1}	Enthalpy ΔH, Kcal.mol^{-1}	Entropy ΔS, calK^{-1}mol^{-1} cal.mol^{-1} K^{-1}	Entropy contribution $T\Delta S$, Kcal.mol^{-1}	Free energy, ΔG Kcal.mol^{-1}
Arrhenius equation*[1]	5	21-31	8.4±0.8	7.8±0.7	-30.8±2.0	-9.2±0.8	16.9±1.2
Arrhenius equation*[1]	7	20-30	-1.1±0.2	-1.7±0.2	-63.1±4.0	-18.8±0.4	17.1±1.0
Arrhenius equation*[1]	16	16-31	5.1±0.3	4.5±0.3	-38.3±2.0	-11.4±0.6	15.9±1.0
Arrhenius equation*[1]	15	18-32	-7.6±1.9	-8.1±2.0	-85.2±6.0	-25.4±2.0	17.2±4.3
Arrhenius equation*[2]	7	22-28	0.9±2.0	0.3±1.0	-59.3±140	-17.7±30	17.0±30
Arrhenius equation*[3]	5	21-29	7.3±3.0	6.7±3.0	-45.4±5.0	-13.5±0.4	20.2±.0.9
Arrhenius equation**[4]	17	16-30	-8.2±2.1	-8.8±2.0	-87.8±5.0	-26.1±5.2	17.3±4.0
Arrhenius equation**[4]	18	18-23	9.5±4.0	8.9±3.0	-27.1±2.0	-8.1±1.0	17.0±1.0
Cumulative distribution[5]	5	20 & 25	6.1±0.2	5.5±0.4	-38.8±3.0	-11.6±0.8	17.1±1.1
Cumulative distribution[5]	7	20 & 30	-1.2±0.01	-1.8±0.01	-63.4±3.0	-17.2±0.7	17.5±0.6
Cumulative distribution[5]	16	16 & 22	3.7±0.4	3.1±0.3	-57.3±3.0	-17.1±0.8	17.4±0.6
Cumulative distribution[5]	9	25 & 30	2.2±0.3	1.6±0.2	-51.9±2.0	-15.5±0.7	17.1±0.8
Cumulative distribution[5]	15	21 &29	-5.4±0.4	-5.9±0.5	-70.8±4.2	-21.1±1.1	15.1±0.7
Cumulative distribution[5]	3	26 & 33	1.8±0.5	1.3±0.4	-54.6±4	-16.3±1.1	17.4±1.5

*Rats were not subjected to heat stress. **Rats were subjected to the environmental heat stress. 1) EOG rate constants measured at the steady state temperatures. 2) EOG rate constants measured at the transient temperature changed ~1.5 ^{o}C/min. 3) EOG rate constants measured by the relative area change under the EOG peak. 5) EOG rate constants measured by the cumulative frequency distributions of EOG rate constant at two temperatures.

5.5. Exposure of Epithelia from Heat Stressed Animals to Increasing Temperatures within Perfusion Chamber

In addition to understanding how electrical responses to odorant stimulation would differ between controls and our individual methods of heat stress, we were interested in possible contrasts in morphology and electrical activity when epithelia taken from already heat-stressed animals were then exposed to further increases in temperature within the EOG perfusion chamber. Throughout the time course of all experiments, some of the animals that had undergone exercise stress for biochemical assays in collaborating work were sacrificed and their epithelia removed for either immunofluorescence microscopy or EOG analyses.

5.5.1. Microscopic analysis of olfactory epithelial olfactory marker protein (OMP)

Immunofluorescence staining using an anti-olfactory marker protein antibody was performed using both epithelia from non-stressed animals and stressed animals. Olfactory marker protein was chosen for staining because it is a common indicator of mature olfactory sensory neurons. Presence of the marker should show the presence and morphology of the OSNs within the epithelium. **Figure 34** shows one of the clearest comparisons we found between stressed and non-stressed epithelia. Arrow heads indicate the ciliary knobs atop OSN dendrites, in which olfactory receptors are embedded. Full arrows indicate the dendrites of bipolar OSNS which extend apically towards the epithelial surface. Asterix indicate OSN cell bodies. Comparing these images shows that density of OSN appears to be reduced and dendrites appear damaged and in disarray within the stressed epithelium.

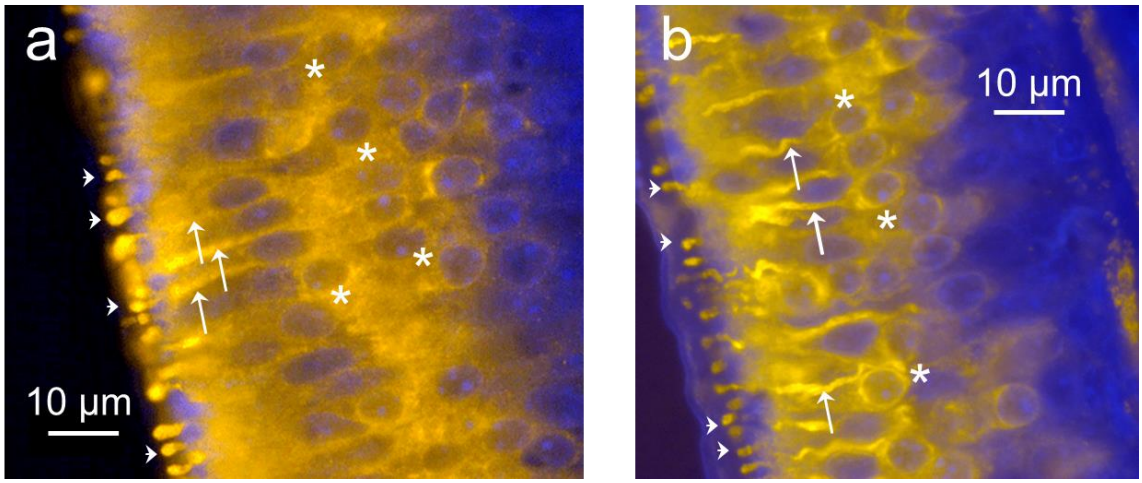

Figure 34. Immunofluorescence staining for olfactory marker protein within olfactory epithelia. *Arrow heads indicate ciliary knobs on the apical surface of olfactory sensory neurons. Full arrows indicate dendrites extending from olfactory neuron cell bodies. Asterix indicate olfactory neuron cell bodies. (A) Epithelia dissected from non-stressed control animals for EOG recordings and subsequent anti-OMP tagging. (B) Epithelia dissected from animals that had undergone metabolic heat stress and epithelia was subsequently exposed to increased temperature during EOG recordings.*

5.5.2. Changes in EOG amplitude, under-peak area, and rate constant

Olfactory epithelia from animals that had undergone metabolic heat stress were isolated and placed in the EOG temperature-controlled perfusion chamber. In the perfusion chamber, temperature was regulated at increasing intervals as long as stable EOG traces could be achieved, similar to previously presented results from non-stressed animals. When rats were subjected to heat stress, they demonstrated different EOG curve characteristics at increasing temperatures than rats that were not previously exposed to stress. EOG amplitude and area under the curve are directly associated with the number of activated olfactory sensory neurons. The rate constant of a reacting system is a measure of how quickly the activation and deactivation occurs. Figure 35 shows EOG height (μV), under-peak area (mVms), and rate constant (1/s) for olfactory epithelia from heat stressed rats (red bars) and non-stressed rats (black bars) at 16°C, 20°C, and 29°C. At all three temperatures, EOG peaks are significantly lower after the animals were subjected to heat stress. Similarly, the under-peak area is significantly lower at all three temperatures after heat stress. Rate constant measurements did not have as dramatic of an effect. While heat stressed epithelia showed an increased rate constant at 16°C, 1.82 1/s as compared to 1.45 1/s compared to controls, at 29°C, epithelium from stressed animals had about 30% slower rate constants.

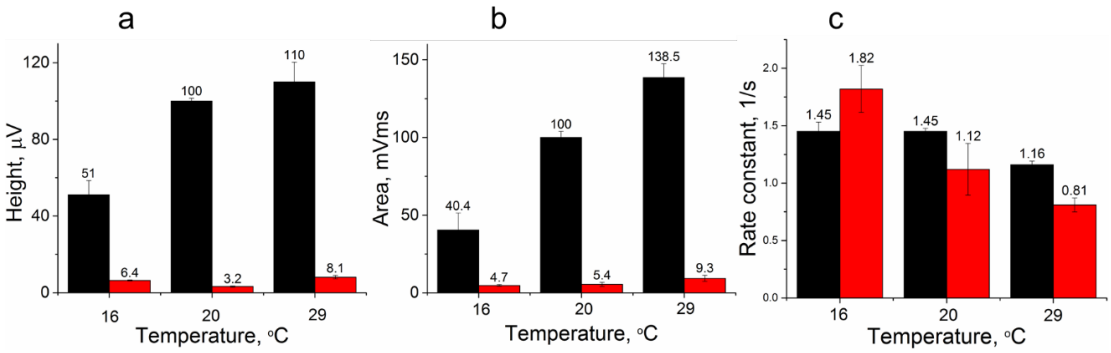

Figure 35. EOG Amplitude, Under-Peak Area, and Rate Constants. *The EOG amplitude (height), under-peak area, and rate constant, respectively, for olfactory epithelia for rats after heat stress (red bars) and control (black bars).* ***(A)*** *At temperatures 16, 20, and 29°C, the height of EOG peaks are significantly lower after the animals were subjected to heat stress.* ***(B)*** *At temperatures 16, 20, and 30°C, the area of EOG peaks are significantly lower after the animals were subjected to heat stress.* ***(C)*** *At temperatures 16, and 20°C, the rate constants of EOG peaks are not significantly lower after the animals were subjected to heat stress. At temperature 29°C the rate constants of EOG peak is about 30% lower after the animals were subjected to heat stress.*

5.6. Effects of Elevated Temperature and Oxidation on the Zinc Nanoparticles Participating in the Initial Events of Olfactory Transduction

5.6.1. After oxidation, zinc nanoparticles lose their ability to enhance olfactory responses to odorants

Samantha Hagerty[1], Yasmine Daniels[2], Melissa Singletary[1] Oleg Pustovyy[1], Ludmila Globa[1], William A MacCrehan[2], Shin Muramoto[2], Gheorghe Stan[2], June W. Lau[2], Edward E. Morrison[1], Iryna Sorokulova[1], and Vitaly Vodyanoy[1*]

[1] Department of Anatomy, Physiology and Pharmacology, Auburn University College of Veterinary Medicine, Auburn, Alabama, USA

[2] Material Measurement Laboratory, National Institute of Standards and Technology, Gaithersburg, Maryland, USA

*Corresponding Author: Vitaly Vodyanoy, 109 Greene Hall, Auburn University, Auburn, AL 36849, e-mail: vodyavi@auburn.edu; tel.; +1-334-844-5405.

I. Abstract

Electrical responses of olfactory sensory neurons to odorants were examined in the presence of zinc nanoparticles of various sizes and degrees of oxidation. The zinc nanoparticles were prepared by the underwater electrical discharge method and analyzed by atomic force microscopy and X-ray photoelectron spectroscopy. Small (1.2±0.3 nm) zinc nanoparticles significantly enhanced electrical responses of olfactory neurons to odorants. After oxidation, however, these small zinc nanoparticles were no longer capable of enhancing olfactory responses. Larger zinc oxide nanoparticles (15 nm and 70 nm) also did not modulate responses to odorants. Neither zinc nor zinc oxide nanoparticles produced olfactory responses when added without odorants. The enhancement of odorant responses by small zinc nanoparticles was explained by the creation of olfactory receptor dimers initiated by small zinc nanoparticles. The results of

this work will clarify the mechanisms for the initial events in olfaction, as well as to provide new ways to alleviate anosmia related to the loss of olfactory receptors.

II. Introduction

Previous studies have demonstrated that zinc metal nanoparticles, at low concentrations, can enhance electroolfactogram (EOG) or whole cell patch-clamp responses to odorants (Viswaprakash et al. 2006; Viswaprakash et al. 2009). Introducing these particles along with an odorant can increase responses by about 3-fold. Zinc nanoparticles, create no odor effects alone, but increase the odor response if mixed with an odor. In small concentrations, effects are dose-dependent and reversible. The particles are spontaneously eliminated from the olfactory mucosa; providing a specific, sensitive, and efficient way of olfactory response control. Some other metal nanoparticles such as copper, gold, and silver do not present the results observed for zinc. Gold and silver nanoparticles created a transient enhancement, while copper nanoparticles did not affect the relative EOG amplitude, but prolonged the overall stability of the signals (Viswaprakash et al. 2009). When zinc nanoparticles were replaced by Zn^{+2} ions at the same concentrations, a decrease in receptor neuron response was recorded. When the enzymatic decomposition of the second messenger cyclic adenosine monophosphate (cAMP) was eliminated by the membrane-permeable phosphodiesterase inhibitor 3-isobutyl-1-methylxanthine (IBMX), the increased cAMP produced EOG signals that were not enhanced by zinc nanoparticles (Moore et al. 2012). Based on these findings, we determined that zinc nanoparticles function at the olfactory receptor level and engage in the initial events of olfaction. A kinetic model of olfactory receptor/odorant/metal

interactions based upon experimental results described a stoichiometry of metal nanoparticles and receptors, and the mode of their action (Vodyanoy 2010). The kinetic olfactory model estimated that one metal nanoparticle binds two receptor molecules to make a dimer. Our canine functional magnetic resonance imaging (fMRI) results indicate that the addition of zinc nanoparticles results in a significant increase of brain excitation in response to odorants, consistent with the increase in excitation of olfactory sensory neurons observed in response to higher vs. lower concentrations of odorants (Jia et al. 2012; Jia et al. 2014). We also found that zinc nanoparticles enhanced sensitivity to odor intensity with no effect on odor valence perception. These results agree well with our *in vitro* electrophysiological results. We showed that most of the atoms of small zinc nanoparticles were not oxidized (Vodyanoy et al. 2016). In the present work, we will examine the effect of zinc nanoparticles oxidation on their ability to enhance odorant responses. Furthermore, we will determine if zinc oxide nanoparticles evoke significant responses in olfactory sensory neurons when delivered without odorants.

III. Methods

a. Metal Nanoparticles

Metal nanoparticles were produced by a modified method (Kruyt 1952; Tokushige et al. 2010). The system consists of a water container with a high-voltage generator connected to two metal electrodes submerged in water. By controlling the voltage and distance between electrodes, the plasma created under water produces a very fine dispersion of the metal into nanoparticles. Two metal electrodes (Alfa Aesar, 99.9999%) of 2 mm diameter are positioned in a large Pyrex jar ≈ 7 mm below the gas-

water interface at the distance between electrodes of ≈ 0.5 cm. 750 mL of LC-MS grade water (Omnisolv) are used in this procedure. Before the experiment, to remove dissolved oxygen, the water was heated up to boiling point and boiled until the large vapor bubbles appeared. The water then cooled to 298.15 K (25^{o}C) and for 20 minutes percolated with nitrogen gas produced by evaporation of liquid nitrogen. The jar filled with nitrogen gas was placed in the water bath with running water to prevent overheating. An alternating voltage of 15 kV and 60Hz, was applied to the electrodes, and the electric discharge was sustained for 1 h. The water suspension was collected in a 1 L glass beaker and placed in the refrigerator for 12 h to allow large metal particles to sediment. Suspended particles were separated from the sediment and subjected to centrifugation at 147,099.75 m/s^2 (15,000 g_n) for 2 h at 298.15 K (25 ^{o}C). After centrifugation, the pellet was discarded, and the supernatant was subjected to further centrifugations to produce fractions of nanoparticles enriched in particles of particular sizes. The centrifuge speed and time to separate nanoparticles by size was estimated with Stock's equation.

$$U=g_n d^2(D-\rho)/18\eta,$$

where U was the rate of sedimentation, g_n – acceleration, d – diameter of the nanoparticle, D and ρ are densities of metal and water, respectively, and η is the viscosity of water.

Zinc nanoparticles were size-selected for 1 nm to 2 nm diameters. These were prepared by the electrical discharge method as described above, a part of the small zinc nanoparticles was oxidized by percolating air through the suspension of nanoparticles for 20 min at 313.15 K (40^{o}C). The air for the oxidation procedure was obtained by evaporation of liquid air. Zinc oxide nanoparticles provided by NIST with nominal

diameters of 15 nm and 70 nm (Black et al. 2012; Cline et al. 2013) were also used in olfactory experiments.

The particle suspensions were analyzed similarly to methods described previously (Samoylov et al. 2005; Daniels et al. 2015; Vodyanoy et al. 2016). The total concentration of metal in suspension was measured by atomic absorption spectra (GTW Analytical Services), and the particle size and number determined by the atomic force microscopy (AFM). The crystallinity of small nanoparticles was analyzed by the Transmission Electron Microscopy (TEM). The degree of nanoparticle oxidation was obtained from the X-ray photon spectroscopy (XPS).

b. Zn^{2+} Ion Concentration in Suspensions of Nanoparticles

Zinc ion concentration was measured in the zinc and zinc oxide nanoparticle water suspension. The concentration of Zn^{2+} ions in suspensions of small zinc nanoparticles was measured before and after oxidation. Zn^{2+} measurements were carried out with duplicate samples. Zinc ion levels were measured using the Colorimetric Zinc Ion Quantitation Kit (AAT Bioquest, Sunnyvale, CA) according to the manufacturer's instructions. Optical density values were measured at 620 nm using a microplate reader (Bio-Tek, Winooski, VT). The zinc ion concentration of the sample was determined by comparison of experimental mean values with curves generated by standards, supplied with the assay. The minimum detectable concentration of the assay was 0.1 μmole/L.

c. Transition Electron Microscopy (TEM)

TEM was performed using an FEI Titan at 300 kV. A few microliters of air-dried droplets of the Zn NP suspension were spread onto a holey carbon substrate on copper TEM grids. Fringes widths were measured on different nanoparticles, and the Miller-Bravais indices of the crystalline structures were calculated using the Crystallography lab software (Gu et al. 2016).

d. Atomic Force Microscopy (AFM)

Images of metal nanoparticles were taken by Bruker MultiMode 8 (Santa Barbara, CA) atomic force microscope in Tapping® (intermittent-contact) mode, using PPP-SEIH Nanosensors (Neuchatel, Switzerland) AFM probes; the nominal values specified by the vendor for the force constant and the resonance frequency of these probes are 15 N/m and 130 kHz, respectively. The AFM calibration was verified before measurements on crystallographic 6H-SiC (0001) steps. From the topographical micrographs of these steps, the AFM calibration was found to be within 3% accuracy of the nominal height (0.75 nm) of SiC single half-monolayers. The AFM imaging was used to measure the size distribution of particles. Monolayers of zinc nanoparticles were prepared on a mica substrate for all measurements by depositing and evaporating a small amount of 0.01% nanoparticles water suspension on freshly cleaved mica surfaces.

e. X-Ray Photoelectron Spectroscopy (XPS)

XPS was used to make quantitative spectroscopic measurements of the elemental composition of the nanoparticles' surfaces. The Kratos Axis Ultra delay-line detector (DLD) instrument in the hybrid mode used a monochromatic Al Kα1, 2 x-ray source (hυ

= 1486.6 eV). The stoichiometry of the Zn and ZnO components were determined from the high-resolution spectra of Zn 2p (1017 eV to 1057 eV) and were acquired using a pass energy of 40 eV with an energy resolution of 0.1 eV. A Gaussian distribution was used for peak fitting, with a full width at half maximum (FWHM) constraint of 1.7 eV, which was obtained from the C 1s peak located at 285 eV (BE). Water suspensions containing zinc and zinc oxide nanoparticles were deposited separately on silicon wafers and allowed to evaporate during pump down to minimize oxidation. To examine the stability of zinc metal nanoparticles, the particles were stored at 278 K (5^{o}C) for 317 days and XPS were measured at the beginning and the end of the storage.

f. Animals

Animals used in this project were cared for by the Division of Laboratory Animal Health of Auburn University assuring compliance with all applicable regulations. The primary regulations governing the care and use of animals utilized in research and teaching include the following: the Animal Welfare Act, the NIH-PHS Policy, the Guide for the Care and Use of Laboratory Animals, and the Guide for the Care and Use of Agricultural Animals in Agricultural Research and Teaching. The protocol was approved by the Auburn University Institutional Animal Care and Use Committee (AU IACUC) committee. Strong efforts were made to avoid exposing animals to discomfort, pain, or injury. Adult male Sprague–Dawley rats (Envigo, Dublin, VA) weighing 250 g to 300 g were used.

g. Odorants

Odorants were purchased from Sigma-Aldrich. An odorant mixture containing 1.6 mmole/L each of ethyl butyrate, eugenol, and (+) and (–) carvone in water was mixed with a vortex and stored in a dark glass bottle until the experiment.

h. Delivery of Odorants and Metal Nanoparticles

For stimulation, a 0.25 s pulse of the odorant mixture at 55158 N/m^2 (8 psi) was formed by a computer-controlled Pneumatic PicoPump PV800 (World Precision Instruments, Sarasota, FL). A pulse of positive pressure drove the odorant into a glass nozzle directed at the olfactory epithelium. The residual odorant was cleared by air between each stimulus application. The odorant pulse patterns were initiated manually at predetermined time intervals or automatically by a computer. The automatic computer routine was composed of 0.25 s pulses at 20 s and 60 s intervals for EOG recording. One series of 10 pulses at 20 s intervals constituted one ‘‘EOG recording’’. Thus, in the automatic regime, the single EOG recording had a duration of 200 s and could correspond to 10 response traces. These recordings were repeated as many times as needed to cover a desirable number of pulses and duration for a single experiment. A nanoparticle suspension was mixed with odorant solutions to make final nanoparticle concentrations of 0.02 nmole/L. During the puff, the odorant vapor containing metal nanoparticles was delivered to the OE surface. We showed that delivery of metal nanoparticles by the water vapor and the liquid suspension produced an efficient transfer of particles to the olfactory epithelium (Viswaprakash et al. 2009). The odorants and

nanoparticles delivered by the water vapors were perceived by live animals (Jia et al. 2014; Jia et al. 2016).

i. Electrophysiology

Our measurements are based on Electroolfactography (EOG) (Viswaprakash et al. 2009). The method utilizes Axon Instrument MultiClamp 700A amplifier and 1322A DigiData acquisition system. Rat septal olfactory mucosa was dissected out and placed in a perfusion chamber such that the basal portions were immersed in physiological buffer (containing 137 mmole/L NaCl, 5.3 mmole/L KCl, 4.2 mmole/L $NaHCO_3$, 0.4 mmole/L KH_2PO_4, 3.4 mmole/L Na_2HPO_4, 1.3 mmole/L $CaCl_2$, 0.2 mmole/L $MgSO_4$, and 5.6 mmole/L D-glucose at pH 7.4), while the epithelial surface with olfactory cilia was exposed to air. Patch electrodes of approximately 24 μm tip opening areas filled with the same physiological buffer were connected to a patch-clamp amplifier to detect responses from the olfactory epithelium. Once contact between the electrode and the surface of the olfactory epithelium was formed, air puffs of the odorant mixture were applied. Zinc metal or metal oxide particles were added to the odorant mixture. Odor responses over the time course of several minutes were recorded after being amplified by a patch-clamp amplifier and filtered at 2 kHz to 5 kHz. The stimuli were given by 3 sequences. The sequence I was composed of the pulses (1) odorant mixture, (2) odorant mixture +small zinc nanoparticles, (3) odorant mixture + 15-nm ZnO nanoparticles, (4) odorant mixture + 70-nm ZnO nanoparticles, (5) 15-nm ZnO nanoparticles, (6) 70-nm ZnO nanoparticles, and (7) water vapors. The sequence II contained pulses of (1) odorant mixture, (2) odorant mixture +small zinc nanoparticles, (3) odorant + small ZnO nanoparticles, (4, 5)

water vapor. The sequence pulses III was applied to the olfactory and respiratory epithelia and composed of (1) odorant mixture, (2) odorant mixture + small zinc nanoparticles. At one contact, 3 to 5 repetitions of the EOG recording of 10 traces each were collected. After completion of EOG recording in the first contact, the electrode was moved to another area of the olfactory epithelium and a new contact was made to generate 3-5 repetitions of EOG recording. EOG was collected from 3 to 5 areas of the epithelium and experiments were replicated with 2-3 epithelia for each sequence of pulses.

IV. Results

a. AFM and XPS

Figure 36 exhibits the physical properties of zinc nanoparticles prepared by high-voltage discharge. AFM showed the size distributions of Zn nanoparticles, with average diameters of 1.2±0.3 nm (Figure 31 a). A histogram (Figure 31 b) shows a distribution with a relatively high peak around the average value (the standard deviation [SD] was calculated from the bell distribution around the peak) and the tail up to 6 nm. Figure 31 c displays the XPS of freshly prepared (3 days old) 1.2 nm zinc nanoparticles. The XPS analysis of the Zn $2p_{3/2}$ core line revealed that metallic zinc nanoparticles were oxidized to a very small extent, where the relative atomic concentrations of Zn and ZnO species were determined to be (93.9±3.4 (SD)) % and (6.1±3.4 (SD)) %, respectively. These data reveal that about 94% of metal atoms were not oxidized. In contrast, the 1.2 nm zinc oxide nanoparticles were found to contain smaller concentrations of metallic zinc (88.5±2.1 (SD)) % and a higher concentration of oxidized zinc (11.5±2.1 (SD)) %,

respectively. As expected, the 15 nm and 70 nm zinc oxide nanoparticles contained (98.2±0.2 (SD)) % and (99.3±0.4 (SD)) % of ZnO, respectively. After 317 days of storage of 1.2 nm zinc nanoparticles at 278 K (5^{o}C), the XPS showed the relative atomic concentrations of Zn and ZnO species to be (96.0±0.5 (SD)) % and (4.0±0.5 (SD)) %, respectively. The relative atomic concentrations at the beginning and the end of storage are not significantly different (n=6, p<0.01).

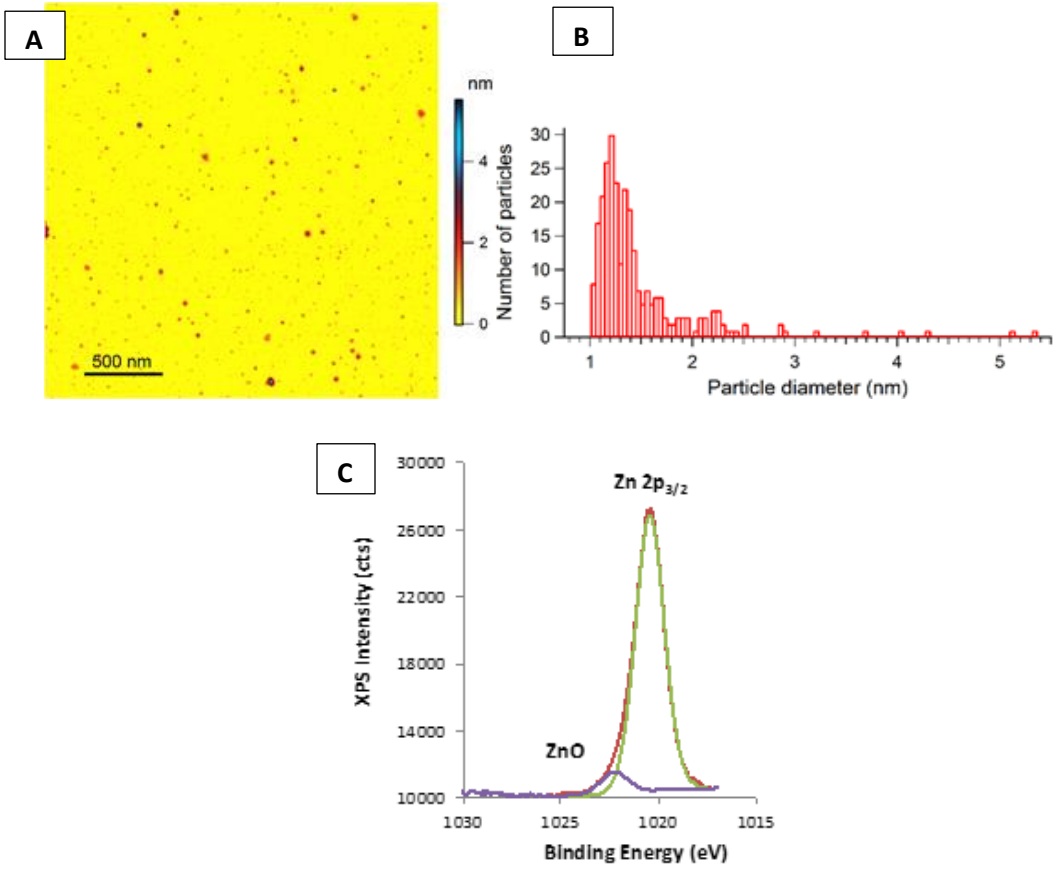

Figure 36. Physical characterization of small zinc nanoparticles. ***(A)*** *AFM image, 0.01% zinc NPs on mica. 270 NPs with height above 1nm were detected over a 2.5um2 area.* ***(B)*** *The size distribution of the particles imaged in A.* ***(C)*** *High resolution XPS analysis is showing the Zn2p1/2 core line, with the Zn peak occurring at a binding energy of 1020.9 eV and the ZnO peak occurring at 1022.5 eV. (Permission from Dovepress #11575629)*

b. TEM

Zinc metal nanoparticles are shown in **figure 37** as TEM micrographs. The TEM micrographs reveal nanoparticles with diameters of approximately 2 nm to 5 nm in size showing crystal lattice fringes.

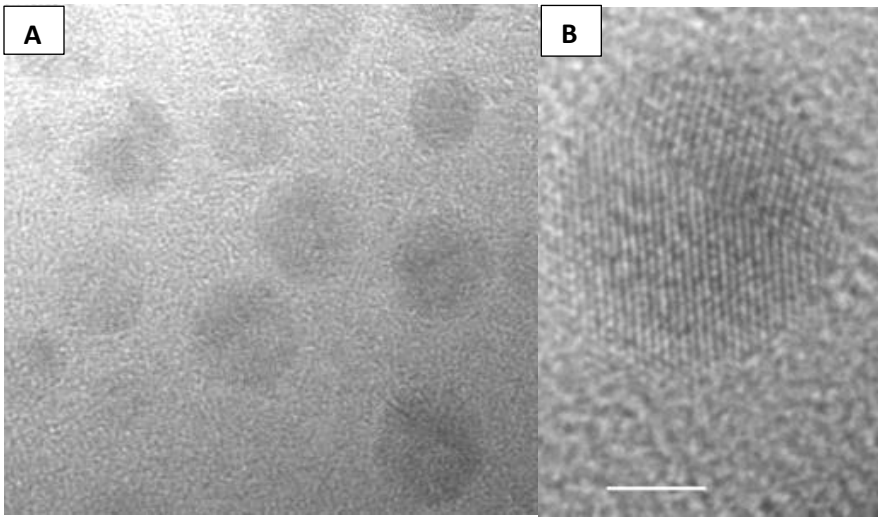

Figure 37. Transmission electron microscopy of zinc metal nanoparticles*. A) Bar 5nm, B) Bar 2nm*

c. Responses

Representative EOG recordings in **figure 38** show odorant responses modified by 1.2 nm zinc nanoparticles as well as small and large zinc oxide nanoparticles. The relative peak amplitudes are given in Table 3. Only non-oxidized zinc nanoparticles enhance odorant responses. The oxidized nanoparticles manifested a slight decrease of the EOG amplitude when they were mixed with odorants. The EOG signals evoked by ZnO nanoparticles with water vapor (no odorants) were minuscule and not much different from the EOG responses to water vapor (**table 3, figure 38, traces 5-7**). The control experiments with respiratory epithelium show no response to the odorant and a mixture of odorant with zinc metal nanoparticles (**figure 39**).

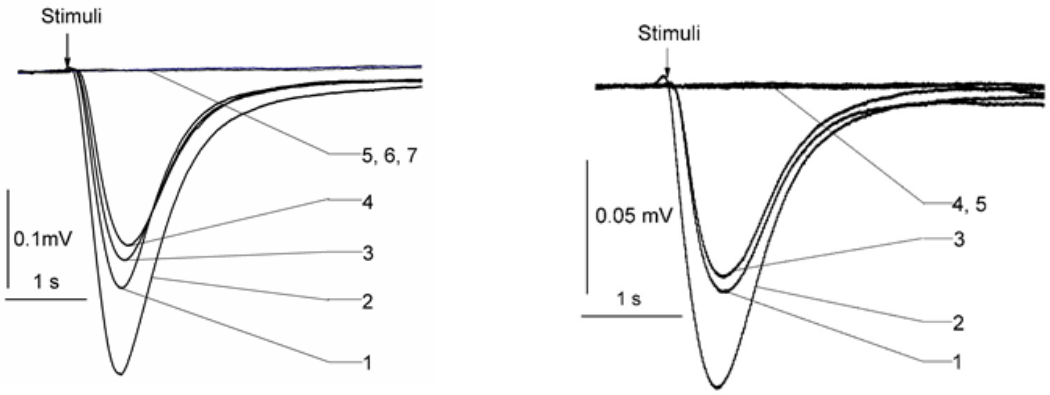

Figure 38. Representative EOG recordings from rat olfactory epithelium. ***(A)*** *The stimuli were of 0.25s pulses of (1) odorant mixture, (2) odorant mixture + 1.2nm ZnNPs, (3) odorant mixture + 15nm ZnO NPs, (4) odorant mixture + 70nm ZnO NPs, (4) odorant mixture + 70nm ZnO NPs, (5) 15nm ZnO NPs, (6) 70nm NPs, and (7) water vapor. The representative set of traces was obtained from 200 EOG traces.* ***(B)*** *The stimuli were of 0.25s pulses of (1) odorant mixture, (2) odorant mixture + 1.2nm ZnNP, (3) odorant + 1.2nm ZnO NPs, (4,5) water vapor. This is a typical representation of 300 traces.*

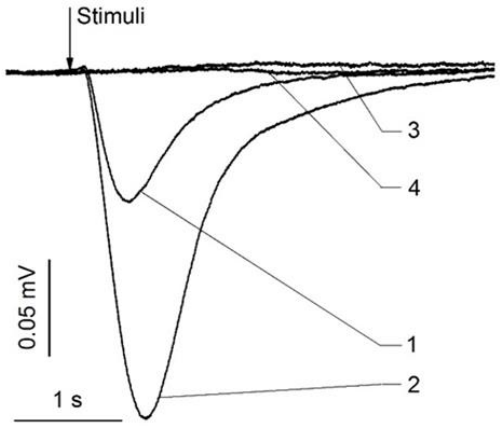

Figure 39. Representative EOG recordings from rat olfactory and respiratory epithelia. *The stimuli were of 0.25s pulses of odorant with or without nanoparticles. (1) olfactory epithelium, odorant mixture, (2) olfactory epithelium, odorant mixture + 1.2nm ZnNP, (3) respiratory epithelium, odorant mixture, (4) respiratory epithelium, odorant mixture + 1.2nm ZnNP. 200 EOG traces.*

d. Zn^{2+} Ion Concentration in Suspensions of Nanoparticles

The Zn^{2+} ion levels are given in Table 1. The Zn^{2+} ion concentrations are presented as mean values ± standard deviation (SD). The zinc ion concentration in the suspension of 1.2 nm zinc nanoparticles is more than 4 times greater than that of 1.2 nm zinc oxide. The zinc ion concentration in all ZnO suspensions varies between 1 μmole/L and 13 μmole/L, while the relative amplitude of EOG evoked by the odorant + suspensions changes only by 0.1%.

Table 3. Effect of nanoparticles on odorant responses. *1) Excitation of EOG by 1. 6 mM odorant vapor + 0.02 nmole/L of nanoparticles, 2) Relative amplitude of the EOG peak evoked by the stimuli to the EOG peak evoked by odorant alone (mean value ± SD). 3) Concentration of Zn^{2+}ions in the stimuli suspension before application to olfactory epithelium (mean value ± SD)*

[1]Stimuli suspension	Nanoparticle Size, nm	[2]Relative amplitude	[[3]Zn^{2+}ion] μmole/L
Zn + odorant	1.2	1.46±0.032	4.8±0.5
ZnO + odorant	1.2	0.82±0.017	1.0±0.20
ZnO + odorant	15	0.88±0.014	7.7±0.8
ZnO + odorant	70	0.85±0.019	13.0±2.0
ZnO with water vapor	15	0.0153±0.004	7.7±0.8
ZnO with water vapor	70	0.0226±0.006	13.0±2.0
Water vapor	NA	0.0360±0.007	NA

V. Conclusions

1. Transmission Electron Microscopy showed a crystalline structure of zinc metal nanoparticles.
2. Atomic Force Microscopy and X-ray Photoelectron Spectroscopy revealed that the majority of the zinc atoms of 1.2 nm zinc nanoparticles were not oxidized.
3. 1.2 nm zinc nanoparticles are suggested to serve as donors of electrons in Turin's vibrational model of olfaction.
4. After oxidation zinc, nanoparticles lose the ability to enhance responses to the odorant.
5. Zinc and zinc oxide nanoparticles do not evoke considerable responses in olfactory sensory neurons when delivered without odorants.

5.6.2. Dependence of PEGylated zinc nanoparticles on temperature and storage time

Work discussed in this subsection is a description of temperature related effects on zinc nanoparticle preservation and function, reported in our recent publication:

PEGylation of zinc nanoparticles amplifies their ability to enhance olfactory responses to odorant

Melissa Singletary[1], Samantha Hagerty[1], Shin Muramoto[2], Yasmine Daniels[2], William A MacCrehan[2], Gheorghe Stan[2], June W. Lau[2], Oleg Pustovyy[1], Ludmila Globa[1], Edward E. Morrison[1], Iryna Sorokulova[1], and Vitaly Vodyanoy[1*]

[1] Department of Anatomy, Physiology and Pharmacology, Auburn University College of Veterinary Medicine, Auburn, Alabama, USA

[2] Material Measurement Laboratory, National Institute of Standards and Technology, Gaithersburg, Maryland, USA

*Corresponding Author: Vitaly Vodyanoy, 109 Greene Hall, Auburn University, Auburn, AL 36849, USA, e-mail: vodyavi@auburn.edu; tel.; +1-334-844-5405.

I. Overview of Research Goal

The discovery of metallic nanoparticles in mammalian blood led to the investigations regarding their physiological role (Samoylov, Samoylova et al. 2005). Zinc nanoparticles, specifically, engineered using a high-voltage electrical discharge method, demonstrated the ability to significantly enhance olfactory responses to odorant stimulation (Viswaprakash, Dennis et al. 2009; Vodyanoy 2010). In a comparison of engineered zinc nanoparticles of various sizes and states of oxidation, the highest olfactory enhancement was noted for nanoparticles measuring approximately 1-2 nm in diameter and in the primarily elemental state, while oxidation inhibited the enhancement (Hagerty, Daniels et al. 2016). However, the enhancement declined over time and with

increasing temperature conditions. Therefore, improvement of the nanoparticles for long-term storage was necessary.

In our most recent work, we tested the hypothesis that zinc nanoparticles coated in 1000 g/mol or 400 g/mol molecular weight polyethylene glycol (PEG) would afford retention of the olfactory enhancement even under long-storage and thermal challenge. The PEGylation is a chemical process involving the passivation of the surface of nanoparticles by PEG, a coiled polymer with multiple ethylene ether units that are soluble in water (Jokerst, Lobovkina et al. 2011). PEGylation is thought to decrease the rate of oxidation. It can provide an increased affinity to the target protein and reduced cytotoxicity of nanoparticles (Jokerst, Lobovkina et al. 2011). The PEGylation is broadly used for protection of nanoparticles against aggregation in biological and pharmaceutical applications (Otsuka, Nagasaki et al. 2003; Suk, Xu et al. 2016). Although there are many publications on the PEGylated zinc oxide nanoparticles (Karakoti, Das et al. 2011), this referenced work of ours is the first study of PEGylated elemental zinc nanoparticles.

Small metal and metal composite nanoparticles have certain advantages compared to other particles due to their capability to specifically interact with proteins, peptides, and nucleic acids (Hassan and Singh 2014) and serve as important players in nanoparticle-based drugs, (Chem & Eng News, 2012) as metal electrocatalysts (McKone 2013), in immune quantum dots (Hoshino 2009), by crossing biological barriers (Gidwani 2014), and many other applications in nanomedicine (Kogan 2007).

The protection of metal nanoparticles from rapid oxidation and improvement of their biophysical and biochemical properties for better interactions with receptors, compatibility of the particle-cell interface, and reduced toxicity, is important for their

potential clinical outcome (Hassan and Singh 2014; Anand, Prasad et al. 2017). The PEGylated nanoparticles discussed have been characterized using scanning electron microscopy (SEM), transmission electron microscopy (TEM), atomic force microscopy (AFM), X-ray photoelectron spectroscopy (XPS), and laser Doppler velocimetry (LDV).

The overall goal of this work was to protect zinc nanoparticles from oxidation and preserve their physiological properties to enhance olfactory responses to odorants over the long storage and elevated temperatures. Olfactory responses are enhanced with the addition of endogenous and engineered primarily-elemental small zinc nanoparticles. With aging and elevated storage temperatures, oxidation of these Zn nanoparticles eliminated the observed enhancement. The design of a polyethylene glycol coating to meet storage requirements of engineered zinc nanoparticles is evaluated to achieve maximal olfactory benefit. The zinc nanoparticles were covered with 1000 g/mol or 400 g/mol molecular weight polyethylene glycol (PEG). Non-PEGylated and PEGylated zinc nanoparticles were tested by EOG with isolated rat olfactory epithelium and odorant responses evoked by the mixture of eugenol, ethyl butyrate and (±) carvone after storage at 278 K (5^{o}C), 303 K (30^{o}C) and 323 K (50^{o}C). The particles were analyzed by atomic force microscopy, transmission electron microscopy, X-ray photoelectron spectroscopy, and laser Doppler velocimetry. Our data indicate that stored ZnPEG400 nanoparticles maintain physiologically-consistent olfactory enhancement for over 300 days even under thermally challenging conditions. These engineered nanoparticles support future applications in olfactory research, enhancing detection sensitivity, and medicine.

II. Materials and Methods

To characterize the properties of zinc nanoparticles under varying conditions, two sets of experimental settings were utilized: (1) Non-PEGylated and PEGylated zinc nanoparticles were stored at 283 K (5^{o}C) and then employed, along with a standard odorant mixture in EOG olfactory experiments over a storage period of 317 days. (2) Non-PEGylated and PEGylated zinc nanoparticles were subjected to accelerated aging at temperatures of 303 K (30^{o}C) and 323 K (50^{o}C) for 2 days before the EOG experiments that followed directly after storage.

a. Preparation of PEGylated Zn Nanoparticles

Zinc nanoparticles of ~1.2 nm in size were prepared by a high-voltage electrical discharge method (Kruyt 1952). The of polyethylene glycol solutions of molecular weight 1000 g/mol or 400 g/mol (Sigma-Aldrich), PEG1000 or PEG400, respectively, were added to the nanoparticle suspension. The suspensions were heated to 40^{o}C, purged with N_2 obtained from liquid nitrogen, and maintained at these conditions for 20 minutes. The suspension was sonicated at 19 Watts, 40 kHz for 20 minutes.

b. Nanoparticle Characterization (TEM, AFM, XPS Analyses)

Physical characterization of nanoparticle preparations using transmission electron microscopy (TEM), atomic force microscopy (AFM), and x-ray photoelectron spectroscopy (XPS) methods were carried out as described in the previous article, section 5.6.1 (Hagerty, Daniels et al. 2016).

III. Results

a. Properties of PEG on the Surface of Zinc Nanoparticles

Zinc nanoparticles were engineered from metal bars by an electrolysis method and were PEGylated with 400 g/mol or 1000 g/mol molecular weight polyethylene glycol (referred hereafter as ZnPEG400 and ZnPEG1000) respectively. The properties of the PEG molecules on the nanoparticle surface are shown in **Table 4.** PEG400, with 14 fewer monomers than PEG1000, was predicted to form a thinner coating on the surface of zinc nanoparticles.

Table 4. Properties of PEG on the surface of Zinc Nanoparticles

Property	**ZnPEG400**	**ZnPEG1000**	**Reference**
Area per PEG single chain, nm2	1.3	2.91	[27]
Number of monomers in PEG	9	23	S1 Supporting Info
Thickness of PEG layer, nm	1.3	2.3	S1 Supporting Info

b. XPS

The non-PEGylated and PEGylated zinc nanoparticles were subjected to four experimental conditions: 1. Freshly prepared nanoparticles stored for 1 day at of 278 K (5^{o}C); 2. Particles stored for 317 days at 278 K (5^{o}C); 3. Particles stored for 2 days at the temperature of 303 K (30^{o}C); and 4. Particles stored for 2 days at 323 K (50^{o}C). Physical analyses of all the samples were performed immediately after the end of each of the exposure conditions to minimize any changes in chemistry. **Figure 40** shows the representative XPS spectra obtained for freshly prepared zinc and PEGylated zinc

nanoparticles stored 1 day at 278 K (5^{o}C). A summary of the XPS data for non-PEGylated and PEGylated zinc nanoparticles for all four experimental conditions is shown in **Table 5.** The spectra were calibrated using the carbon C 1s peak at a binding energy of 284.6 eV, which allowed the identification of the following chemical species at their respective binding energies: hydrocarbon (C-C≈285 eV), ether (C-O, ≈286.1), carboxyl (C=(OH), ≈288.1) [28], zinc (Zn $2p_{3/2}$, ≈1021.8 eV) (Naumkin 2012; Deroubaix 1992) and ZnO (Zn $2p_{3/2}$, ≈1024 eV) (Mai 2013). The rise in the amplitude of C-O peak and the reduction in the binding energy of Zn $2p_{3/2}$ peaks in the ZnPEG400 and PEG1000 samples confirmed the successful PEGylation of zinc nanoparticles. The Zn $2p_{3/2}$ band shown that metallic zinc nanoparticles were oxidized only slightly, where the concentrations of Zn and ZnO were found to be 97.0 ± 0.8 (SD) % and 3.0 ± 0.8 (SD) %, respectively (278 K, 1 day). Interestingly, the PEGylation process caused a significant increase in the concentration of oxidized zinc atoms, where the interaction with PEG400 (278 K, 1 day) resulted in an increase of ZnO concentration from 3.0±0.8 (SD) % to 10.5±4.0 % ($t(5)=4.93$, $p=0.004$), while in the case of PEG1000, the ZnO concentration increased to 12.0±3.8 % ($t(5)=6.47$, $p=0.001$).

Table 5. **XPS properties of bare and PEGylated zinc nanoparticles, stored at various durations and temperatures**

Sample	T (K)	Time days	Survey			High Resolution Zn 2p			
			O1s %	C 1s %	Zn2p %	BE eV	Zn %	BE eV	ZnO %
Zn	278	1	27.8 ± 2.3	70.5 ± 1.7	1.8 ± 0.1	1021.8	97.0 ± 0.8	1024.6	3.0 ± 0.8
ZnPEG400	278	1	32.3 ± 0.5	67.4 ±0.7	0.3 ± 0.1	1022.0	89.5 ± 4.0	1023.8	10.5 ± 4.0
ZnPEG1000	278	1	30.3 ± 0.9	69.6 ± 2.1	0.1 ± 0.0	1021.9	88.0 ± 3.8	1023.5	12.0 ± 3.8
Zn	278	317	38.4 ± 1.0	60.2 ± 1.5	1.4 ± 0.1	1021.9	96.0 ± 1.0	1023.7	4.0 ± 1.0
ZnPEG400	278	317	31.5 ± 0.1	68.4 ± 0.1	0.1 ± 0.0	1022.2	75.9 ± 8.2	1023.9	24.1 ± 8.2
ZnPEG1000	278	317	31.1 ± 0.3	68.0 ± 0.4	0.9 ± 0.2	1021.9	86.1 ± 0.5	1024.2	13.9 ± 0.5
Zn	303	2	24.5 ± 4.1	75.1 ± 0.6	0.4 ± 0.1	1021.7	92.2 ± 3.5	1024.1	7.8 ± 3.5
ZnPEG400	303	2	23.2 ± 4.4	76.6 ± 3.0	0.2 ± 0.0	1022.0	93.0 ± 2.8	1023.7	7.0 ± 2.8
ZnPEG1000	303	2	24.6 ± 5.4	75.2 ± 5.2	0.2 ± 0.1	1021.8	94.2 ± 5.6	1023.4	5.8 ± 5.6
Zn	323	2	38.3 ± 5.3	60.8 ± 3.5	0.9 ± 0.3	1021.0	92.9 ± 3.3	1023.3	7.1 ± 3.3
ZnPEG400	323	2	27.7 ± 4.6	72.1 ± 6.8	0.2 ± 0.1	1021.9	88.6 ± 2.6	1023.7	11.4 ± 2.6
ZnPEG1000	323	2	21.8 ± 3.5	77.9 ± 2.7	0.3 ± 0.1	1021.7	92.7±1.6	1024.0	7.3±1.6

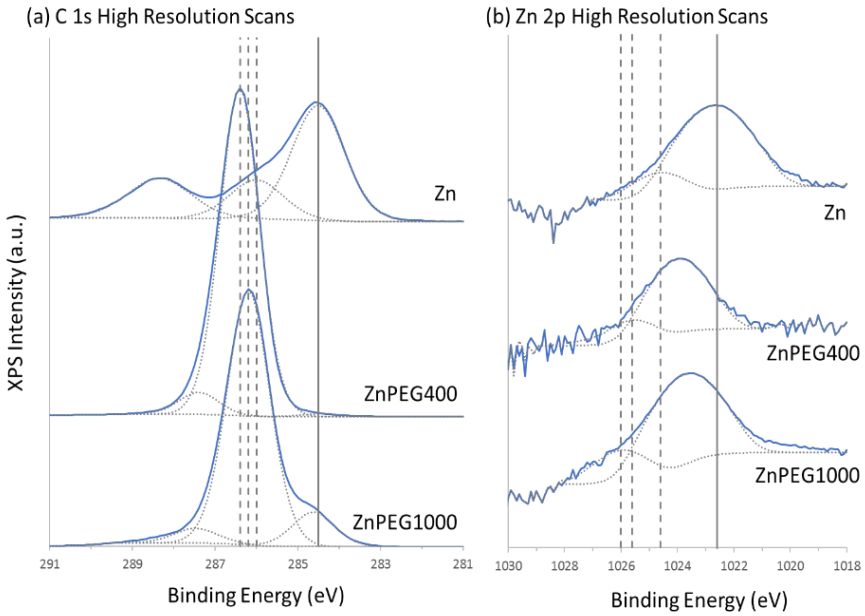

Figure 40. XPS Spectra. *Representative high resolution XPS spectra showing the* **(A)** *C 1s and* **(B)** *Zn 2p3/2 core lines for the freshly prepared bare zinc and PEGylated zinc nanoparticles stored 1 day at 278 K (5°C), with the spectra offset to facilitate viewing. The Zn 2p spectra are shown in log-scale. The solid curves indicate the experimentally obtained spectra, with the dotted curves underneath indicating their best-fit chemical components. For the C 1s spectra, from lower to higher binding energy, the components are C-C, C-O, and C=O. For the Zn 2p spectra, the components are Zn and ZnO. For the* **(A)** *C 1s plots, the solid vertical line represents the position of the C-C peaks, to which all spectra were calibrated to, with the dotted lines showing the spectral shift of the C-O peaks, which were 286 eV, 286.4 eV, and 286.2 eV for the Zn, ZnPEG400, and ZnPEG1000 systems, respectively. For* **(B)** *Zn 2p plots, the solid line represents the position of the Zn peak for the bare Zn system, while the dotted lines show the spectral shift of the ZnO peaks, which were 1024.6 eV, 1025.6 eV, and 1026.0 eV for the Zn, ZnPEG400, and ZnPEG1000 systems, respectively. Each spectrum represents an average of six spectral runs.*

The XPS survey scan of the freshly prepared non-PEGylated and PEGylated zinc nanoparticles (Table 5, 278 K, 1 day) showed the concentration of the O 1s and C 1s species to be 27.8±2.3 % and 70.5±1.7 % , respectively, which significantly changed to 32.3±0.5 %(t(5)=4.28, p=0.003) and 67.4±0.7 % (t(5)=3.77, p=0.005) for ZnPEG400, respectively. The values of O 1s and C 1s for ZnPEG1000 were 30.3±0.9 % (t(5)=2.26, p=0.0053) and 69.6±2.1 % (t(5)=0.74, p=0.48), respectively (there were no statistically

significant changes for ZnPEG1000). ZnPEG400 after 317 days of storage, showed the higher level of ZnO of 24.1±8.2% ZnO compared to 10.5±4.0% ($t(5)=3.45$, $p=0.008$) for the freshly prepared ZnPEG400, as shown in table 5.

Very different XPS results were observed for ZnPEG1000 after storage. The concentration C-O group showed a modest decrease from 94.5±0.6 % to 83.5±1.9 % ($t(5)=12.3$, $p=0.0001$), but a sensible increase in the C-C concentration from 3.0±0.6 % to 11.5±2.4 % ($t(5)=7.68$, $p=0.0001$). The concentration of ZnO for this condition were 12.0±3.8 % and 13.9±0.5 % ($t(5)=1.11$, $p=0.3$) showed no significant difference. These data suggest no significant changes in the electronic structure of both Zn and PEG1000 after the initial PEGylation.

c. Activation Energies of Oxidation

Oxidation of the zinc nanoparticles was observed under storage at different temperatures and duration, as evidenced by the increase of ZnO components in **table 6.** Using an apparent concentration of primarily-elemental zinc as a function of time and storage temperature, the Arrhenius activation energies of oxidation were estimated (Segel 1975) and shown in **table 6.**

Table 6. **Thermodynamic analysis of oxidation of Zn, ZnPEG400, and ZnPEG1000 Nanoparticles**

Particle	T (°C)	Estimated activation energy, (E_a) kJ.mol^{-1}	Reference
Zn, 1.2 nm	5-50	113	Present work
Zn foil, 0.126 mm	300-400	119	[33]
ZnO powder, oxygen desorption	86-97	96	[34]
Molten Zn	600-700	104	[35]
ZnPEG400, 1.4 nm	5-50	15.5	Present work
ZnPEG1000, 1.4 nm	5-50	34.9	Present work
Pd/Fe nanoparticles, 60-100 nm	20-35	39.47	[36]
Pd/FePEG200	20-35	38.66	[36]

.

d. Enhancement of Odorant Response by PEGylated Nanoparticles

The initial experiments were carried out with the freshly prepared non-PEGylated and PEGylated zinc nanoparticles. The EOG responses evoked by PEG400 and PEG1000 without odorant mixture are very small and hardly distinguished from the EOG signal of water. This result is consistent with odorless polyethylene glycol in other work (Gomes 2003). EOG evoked by odorant mixture with zinc nanoparticles (trace 2) shows a strong enhancement compared to the signal induced by the odorant mixture alone (trace 1). Combining odorants with ZnPEG400 and ZnPEG1000 results in the lower signals depicted by the traces 3 and 4, respectively. The mean values of seven measurements of

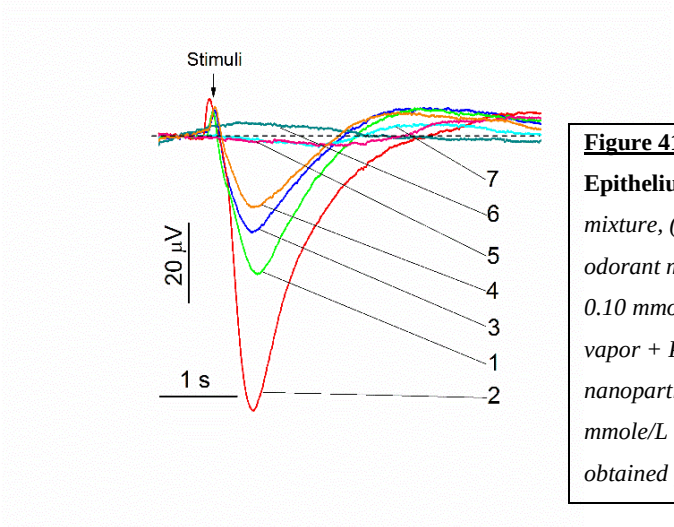

Figure 41. **Representative EOG Recordings from Rat Olfactory Epithelium.** *a The stimuli were of 0.25 s pulses of (1) odorant mixture, (2) odorant mixture +1.2 nm zinc nanoparticles, (3) odorant mixture + 0.25 mmole/L PEG400, (4) odorant mixture + 0.10 mmole/L PEG1000, (5) water vapor + PEG400, (6) water vapor + PEG1000, and (7) water vapor. The concentration of zinc nanoparticles and odorant mixture were 0.02 nmole/L and 1.6 mmole/L , respectively. The representative set of traces was obtained from 50 EOG traces.*

the relative responses to the odorant mixtures with Zn, ZnPEG400, and ZnPEG1000 were 2.69±0.11, 0.821±0.05, and 0.310±0.04, respectively. An analysis of variance showed that at the 0.05 level, the means were significantly different, $F(2, 18)=1900$, $p=0.000$, indicating that the freshly prepared zinc nanoparticles were superior to ZnPEG400 and ZnPEG1000, and ZnPEG400 with odorant produced larger relative responses than ZnPEG1000 with odorant.

The olfactory responses to odorant mixed with PEG400 or PEG1000 were tested systematically over the period of 317 days. As evidenced by the foregoing data, the freshly prepared Zn nanoparticles outperformed both ZnPEG400 and ZnPEG1000. However, as analysis of variance showed, at the level of 0.05, there was no significant difference between the relative olfactory responses to Zn, ZnPEG400, and ZnPEG1000 nanoparticles ranging from 3 days to 64 days of storage ($F_{3\ days}(2, 25)=0.64$, $p=0.54$; $F_{5\ days}(2, 69)=2.53$, $p=0.087$; $F_{18\ days}(2, 30)=0.92$, $p=0.41$); $F_{58\ days}(2, 12)=1.14$, $p=0.35$; and $F_{64\ days}=(2, 21)=3.12$, $p=0.065$). Only after 280 days and 317 days of storage we observed the significant difference between the relative olfactory responses to Zn, ZnPEG400, and ZnPEG1000 nanoparticles ($F_{280\ days}(2, 48)=90$, $p=0.000$; $F_{317\ days}(2, 36)=149$, $p=0.000$). Following 280 days of storage, ZnPEG400 provided the highest enhancement followed by Zn and then ZnPEG1000. Near the end of the storage time, the mixture odorant and

ZnPEG1000 caused a decrease of the EOG signal compared to the signal generated by the odorant alone **(figure 42).**

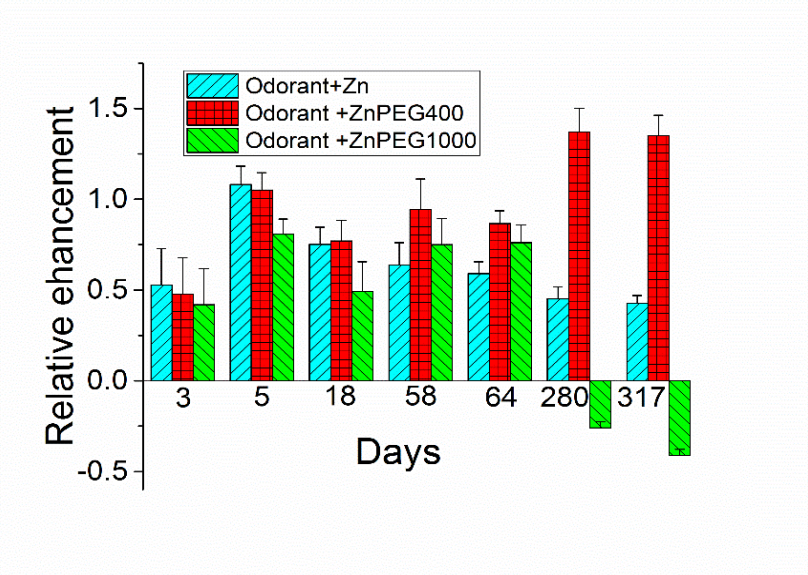

Figure 42. The relative EOG signals as a function of time of storage of zinc nanoparticles. *a The stimuli were of 0.25 s pulses of (1) odorant mixture, (2) odorant mixture +1.2 nm zinc nanoparticles, (3) odorant mixture + 0.25 mmole/L PEG400, (4) odorant mixture + 0.10 mmole/L PEG1000, (5) water vapor + PEG400, (6) water vapor + PEG1000, and (7) water vapor. The concentration of zinc nanoparticles and odorant mixture were 0.02 nmole/L and 1.6 mmole/L , respectively. The representative set of traces was obtained from 50 EOG traces.*

To characterize effects of thermally-enhanced formation of ZnO on the odorant responses, we analyzed the effects of non-PEGylated and PEGylated zinc nanoparticles stored for two days at an elevated temperature. **Figure 43** shows the relative enhancement of responses to odorants as the function ZnO concentration determined by XPS and temperature. The relative olfactory enhancement by the zinc nanoparticles declined sharply from 55% to -7 %, when the ZnO concentration increased from 3.0% to 11.5 % **(figure 43a).** The enhancement with ZnPEG1000 did not show dependence on the ZnO concentration but it strongly declined with the temperature **(figure 43c).** It

appeared that enhancement with ZnPEG400 **(Fig 43 b)** was not sensitive to zinc oxidation and temperature.

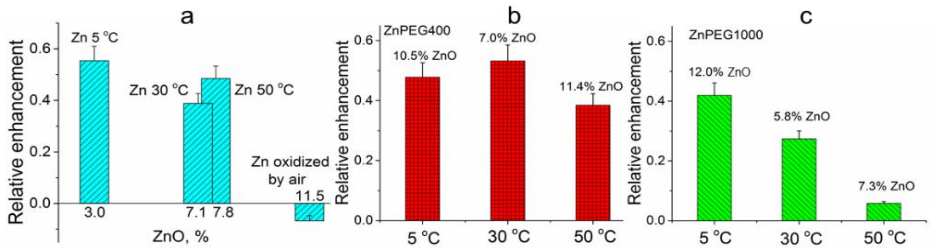

Figure 43. Relative EOG signals evoked by non-PEGylated and PEGylated zinc nanoparticles. ***(A)*** *The relative enhancement by non-PEGylated zinc nanoparticles as a function of ZnO concentration. The difference between peak values of EOG evoked by odorant and by zinc nanoparticles was normalized by the EOG peak evoked by an odorant alone as a function of ZnO concentration that was determined by XPS. The first bar at 3% of ZnO, corresponds to zinc nanoparticles stored one day at 278 K (5°C). The second and third bars reflect zinc nanoparticles stored for two days at 303 K (30°C) and 323 K (50°C), at 7.1% and 7.8%, respectively. The fourth bar at 11.5% of ZnO corresponds to the inhibition that was observed with zinc nanoparticles oxidized by percolating air.* ***(B)*** *The relative EOG enhancement produced by ZnPEG400 nanoparticles after they were stored for one day at 278 K (5°C), two days at 303 K (30°C) and 323 K (50°C), respectively.* ***(C)*** *The relative EOG enhancement produced by ZnPEG1000 nanoparticles after they were stored for one day at 278 K (5°C), two days at 303 K (30°C) and 323 K (50°C), respectively.*

IV. Supplementary Materials

a. Striking Image

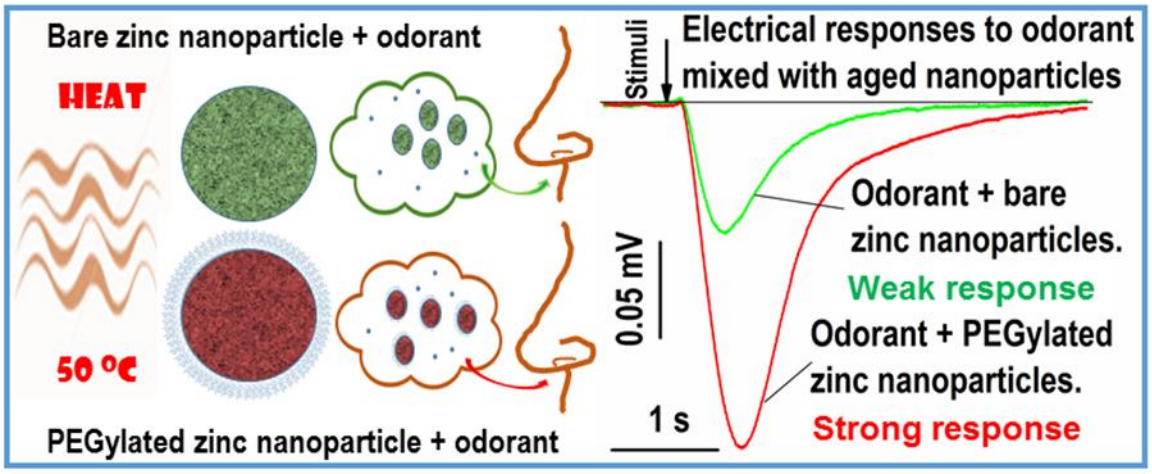

b. Number of monomers in poly-ethylene glycols (PEGs)

The structural molecular formula of PEG is:

$$H\text{-}(O\text{-}CH_2\text{-}CH_2)_n\text{-}OH$$

The molecular mass of the polymer is a sum of masses of H, OH and N×(mass of the monomer) =18 + N×44.

Therefore, the number of monomers in the PEG with a molecular mass of M equals:

$$N=(M-18)/44.$$

Consequently, the number of monomers in PEG400 = (400-18)/44≈9 and in PEG1000=(1000-18)/44≈23.

c. Thickness of the PEG layer on the surface of nanoparticle

Using the area per PEG single chain of a surface of a nanoparticle (Illum, Church et al. 2001) the estimate of the PEG layer thickness (L) can be done by the following equations (Perry, Reuter et al. 2012):

$$L = \frac{Na^{5/3}}{D^{2/3}}, \quad \text{(S1)}$$

Where a=0.35 nm is a length of a single PEG monomer, D – the distance between the PEG's chains defined by the equation:

$$D = 2\sqrt{\frac{A}{\pi}} \quad \text{(S2)}$$

Where A=1.28 nm^2 for the PEG400, and A=2.91 nm^2 for the PEG1000.

From equations (S1) and (S2) follows that L_{400}=1.32 nm and L_{1000}=2.28 nm.

d. The transmission probability of electron transfer through the PEG layer

The transmission probability T of electron with energy E, mass m through the potential barrier of height U_o and thickness L can be approximated by the equations (Griffiths 1995):

$$T = \frac{16E(U_o - E)}{U_o^2}\exp(-2\alpha L) \quad \text{(S3)}$$

$$\alpha = \sqrt{\frac{2m(U_o - E\}}{h^2}} \quad \text{(S4)}$$

Where h is Plank's constant.

For zinc nanoparticles of 1.2 nm in diameter, the electron energy (E) was estimated to be 79.6 meV (Hagerty, Daniels et al. 2016). The potential barrier of PEG layer (U_o) varies depending of method between 0.1 and 0.2 eV(Kabra, Sonkamble et al. 2015; Sannaningannavar, Navati et al. 2016; Smolne, Weber et al. 2016). The transmission probability (T) of electron through PEG400 layer of L=1.32 nm and U_o=0.101 eV (Kabra, Sonkamble et al. 2015) is calculated by equations S3 and S4.

$$\frac{16E(U_o-E)}{U_o^2}=\frac{16(0.0796eV)(0.101eV-0.0796eV)}{(0101\ eV)^2}=2.6718$$

$$\alpha L=(1.32\times10^{-9}m)\times\sqrt{\frac{2(9.11\times10^{-31}kg)(0.101eV-0.0796eV)(1.6\times10^{-19}J/eV)}{(1.055\times10^{-34}J.s)^2}}=0.99295$$

The transmission probability then for PEG400 layer:

$$T_{400}=2.6718\exp[-2(0.99295)]=0.36673.$$

Similar calculations for 1.2 nm zinc nanoparticle covered with PEG1000 layer give

$$T_{1000}=0.08652$$

The transmission probability is a strong function of the potential barrier (U_o). For example, when U_o=0.2eV(Sannaningannavar, Navati et al. 2016; Smolne, Weber et al. 2016) , T400 and T1000 are 0.0345 and 0.00112, respectively.

e. Energy of activation of zinc nanoparticle oxidation

The Arrhenius equation (Segel 1976) can be used to express the temperature dependence of the first-order activation kinetics:

$$k = Ae^{-\frac{E_a}{RT}} \tag{S5}$$

where R is the universal gas constant, E_a represents the apparent activation energy, and A -- the pre-exponential Arrhenius factor. Taking the logarithm of Eq. (S5) yields:

$$\log k = -\frac{E_a}{2.303R} \times \frac{1}{T} + \log A \tag{S6}$$

If the logarithm of k in Eq. (S5) is plotted against the reciprocal of temperature, 1/T, then the slope of this graph yields the activation energy (E_a), the thermal activation level of transitions from not-oxidized to oxidized atoms.

Chapter 6 – Discussion

6.1. Kinetic Effects on Electrical Responses – Systemic Interactions vs. Direct Physical Changes

The differences between whole-body stress exposure and stress to isolated epithelia must be considered. In one method, animals undergo environmental or metabolic heat stress and responses are analyzed after 4 hours, during which many systemic interactions may take place that could influence results. In the other method, viable epithelium isolated from the body is exposed to increasing temperatures, so the electrical changes observed must be directly related to the odor ligand-receptor-channel interactions at the cellular membrane. One major difference between the two concepts is the temperature at which EOG responses remain stable. In whole-body experiments, the environmental chamber was set at 45°C, but the measured body temperatures ranged from 39.4-39.8°C. In contrast, dissected olfactory epithelia were exposed to temperatures of 16-34°C. Temperatures exceeding the higher end of this range resulted in unstable EOG responses and reduced tissue viability. This is expected, as the body exhibits protective functions in response to stressful conditions. Isolated tissue does not have any barrier or interactive mechanisms that serve as homeostatic buffers.

While this work focused on how kinetic properties of EOG responses were affected by the recorded body and epithelial temperatures alone, blood was also collected from environmental or metabolic heat stressed animals for biochemical analyses in simultaneous work not included in the realm of this dissertation. Coupling that information with any observed differences in EOG recordings will be the focus of subsequent work. With respect to olfactory response kinetics, we saw that increased body

temperature was associated with faster activation of olfactory sensory neurons and return to baseline voltage potential.

Odorant composition within the mucus layer lining the epithelium, ligand binding affinity, receptor conformation, CNG channel opening and closing rates, and the presence of olfactory marker protein (OMP) are all potential influential factors on the speed at which olfactory sensory neuron signals activate and deactivate. There are other methods to facilitate olfactory responses. Down-regulation of any step in the olfactory signal transduction cascade could contribute to termination of odorant-evoked responses. The receptor phosphorylation (Boekhoff and Breer 1992), inactivation of G-protein (Simon et al. 1991), reduction of adenylyl cyclase activity (Sklar et al. 1986), and activation of phosphodiesterase (Borisy et al. 1992) could cause a decrease in intracellular cAMP concentrations, and consecutively would reduce the olfactory response. Therefore, inhibition of this down-regulation would cause the enhancement of an olfactory response. Indeed, the existence of inhibitory $G_{\alpha i}$-subunits in olfactory cilia and the adenylyl cyclase enhancement in the presence of $G_{\alpha i}$-antibody were demonstrated (Sinnarajah et al. 1998). Similarly, the inhibition of RGS2 proteins downregulates signal transduction in olfactory neurons by inhibiting activation of adenylyl cyclase. The whole cell patch-clamp experiments demonstrated the enhancement of odorant responses by inhibition of RGS2 proteins by RGS2 antibodies (Sinnarajah et al. 2001). Also, the deactivation of the phosphodiesterase by the IBMX increased cAMP levels in olfactory cilia (Moore et al. 2012). The above enhancement methods are based upon the biochemical intervention that could potentially influence the speed at which transduction cascades are activated, terminated, and open for reactivation. The temperature dependence of neuromuscular

nicotinic acetylcholine receptors (AChRs) was previously investigated (Gupta and Auerbach 2011). While this study did not consider olfactory receptors specifically, it did observe similar changes to the speed of ion channel opening and depolarization with increased temperatures.

6.2. Implications of Probiotic Pre-Treatment

Previous work has demonstrated the efficacy of *bacillus subtilis* in the prevention of intestinal complications resulting from heat stress. The results from this work were presented in chapter 2, section 2.5.3. Animals that were pretreated with probiotics prior to exposure to temperature elevation showed significant reduction in adverse morphological changes and biochemical parameters in comparison to control animals that were pretreated with PBS. We assessed whether probiotic pretreatment could also have an effect on olfactory function.

Animals were subjected to heat stress, and body temperatures were recorded before and after **(Table 1).** Animals subjected to heat stress were either pretreated by oral gavage with *Bacillus subtilis* or pretreated with control PBS. Four hours following the exposure to heat stress, olfactory epithelia were dissected and electrical responses to odorant stimulation were evaluated by EOG. Both stress groups were compared to control animals that were not exposed to heat stress conditions. We found that pretreatment with probiotics resulted in a kinetic shift of half-rise and half-decay times towards control animals. Though it is not known whether the kinetic shift of olfactory responses at the epithelial level translates to a different perception of odor, the fact that probiotics brings the electrical recordings back towards the control is consistent with the

way probiotics have shown the ability to reverse adverse morphological and biochemical parameters in the intestines.

6.3. Temperature Dependence of Dissected Epithelia – Merging Kinetics with Thermodynamics

Under stable EOG conditions, olfactory epithelia responded to 0.25-second long puffs of odorant vapor by generating electronegative responses simultaneously with the onset of stimulus delivery. Typical EOG responses are shown in **Figure 21.** As temperature increases the amplitude and kinetics of EOG changes. The mean time of half-rise (τ_r) significantly decreased from 225.4±6.2 (SE) ms to 184.1±1.3 (SE) ms when temperature increased from 16 to 20^{o}C [F(1, 70)=354, p=0.0]. Similarly, the mean decay time (τ_d) significantly decreased from 529.1±20 (SE) ms to 416.4±3.6 (SE) ms at the same elevation of temperature [F(1, 66)=89, p=0.0]. In this work the thermodynamic variables were found using changes of the EOG kinetic properties as a function of temperature. We found that energy of activation, E_a, is 10 times smaller than free energy. The reactions exhibiting these small, near negative activation energies are termed "activation-less" reactions and were found in electrochemical reactions that depended on molecular binding event within a well-like receptor structure (Lev 1965; Krishtalik 1969; Krishtalik 2016). Raising the temperature of these reactions was shown to lower the probability of molecular collision and decrease capture in the binding sites (Levine 2001). The olfactory receptor binding pocket could play a similar role to the well-like pocket described here. The free binding energy of a specific odorant, helional, to olfactory receptor OR 17-40 (relative to the rat olfactory receptor OR 17) was estimated

to be ~10 kcal/mol (Anselmi, Buonocore et al. 2011). This value is of the same order of magnitude as the free energy found in our work (near the 15-17 kcal/mol) shown in table 2.

The thermodynamic variables given in **Table 2** and plotted figure 24-30 were obtained using four different methods: 1. Arrhenius plot for steady state temperatures; 2. Arrhenius plot for transient temperatures, meaning a slow transition from one temperature to another one rather than a large step increase; 3. Arrhenius plot for change in the relative area under EOG peak; and 4. From the cumulative frequency distribution at two temperatures.

When ΔH values in table 2 were plotted as a function of entropy contribution $T\Delta S$, the data were fitted to the equation $\Delta H = \Delta G_0 + T\Delta S$ where $\Delta G_0 = 18.1 \pm 2.0$ kcal/mol; Slope=1.04±0.12. The energy associated with change of entropy, $T\Delta S$, correlates with the change in enthalpy, ΔH, keeping the free energy $\Delta G = \Delta H - T\Delta S$. This thermodynamic phenomenon is known as *enthalpy-entropy compensation*. In previous work investigating the temperature dependence of ligand-gated neuromuscular nicotinic acetylcholine receptors, the rate and equilibrium constants associated with temperature change were studied (Gupta and Auerbach 2011). An activation enthalpy of 13-24 kcal/mol was calculated. Our calculated results are consistent with enthalpy-entropy compensation observed in the binding of odorants to odorant binding proteins (Portman, Long et al. 2014).

The large contribution of entropy into free energy for EOG related energetics indicates that activation-deactivation processes are entropy driven. The negative value of entropy suggests an increase in order, or decrease of disorder, associated with the EOG

phenomena. Negative entropy ($\Delta S < 0$) has conventionally been associated with decreases in molecular rotational and translational degrees of freedom. $\Delta S < 0$ in processes involving aqueous solvents often involves dehydration forming the interface between molecular contact and ion release (Dragan, Klass et al. 2003). Zanello et al. proposed that the temperature dependence of gating and conductance is influenced by the physical state of the membrane, which is influenced by temperature (Zanello, Aztiria et al. 1996; Gupta and Auerbach 2011).

6.4. Effect of elevated temperature on oxidation and stability of zinc nanoparticles participating in initial events of olfaction

Small endogenous zinc nanoparticles are found in human and animal blood (Samoylov, Samoylova et al. 2005) and these naturally occurring nanoparticles, as well as laboratory engineered zinc nanoparticles, enhance olfactory responses (Viswaprakash, Dennis et al. 2009; Vodyanoy 2010). Because zinc nanoparticle enhancement was seen in awake animals (Jia, Pustovyy et al. 2016) and both young and mature cell cultures (Viswaprakash et al. 2010), as well as in the dissected olfactory epithelium, this enhancement is significant for the initial events in olfaction.

The enhancement of EOG responses to odorants by zinc metal nanoparticles and inability of oxidized zinc to facilitate the same effects may be due to their physical composition and the possibility that oxidation could transition into the ionic state. The oxidation of zinc nanoparticles may change the physical state of the metal, or potentially result in the production of zinc ions (Wöll 2007) which has shown inhibitory effects on olfactory responses. The inhibition by zinc ions may occur due to blocking cyclic-

nucleotide-gated-channels (Kramer and Molokanova 2001), activation of cAMP-specific phosphodiesterase (Percival et al. 1997), inhibition of adenylyl cyclase (Klein et al. 2004) and $G_{\alpha s}$-protein (Gao et al. 2005). Our results, however, show no correlation between the relative amplitude of the EOG peak and the concentration of Zn^{2+}-ions. 1.2 nm zinc nanoparticles increase responses to odorant by a factor of 1.46. When these zinc nanoparticles were oxidized, they were not able to enhance responses to the odorant. This inability to enhance response to odorant is difficult to attribute to the inhibitory actions of zinc ions. The concentration of Zn^{2+} ions that go together with oxidized zinc nanoparticles is five times smaller than that accompanied non-oxidized zinc when the strong enhancement observed. Additionally, the Zn^{2+}ion concentration in all ZnO suspensions changes by 13-fold, while the relative amplitude of EOG evoked by the odorant+ZnO suspensions vary only by 0.1%. These data suggest that after oxidation, the changed physical state of zinc rather than the changed valence state is the main contributing factor to ZnO nanoparticles failure to enhance olfactory odorant responses.

The TEM images reveal round nanoparticles of various diameters. The high-resolution images of zinc metal nanoparticles show lattice fringes which indicate that zinc nanoparticles are crystals. Within the uncertainty of our measurements, we found that the typical fringes of 0.21 nm and 0.17 nm correspond to [01$\underline{1}$1] and [01$\underline{1}$2] directions for the hexagonal close-packed crystal lattice of metal zinc. The results are consistent with those obtained for zinc nanowires and nanorod (Chen et al. 2007; Lu et al. 2016).

The AFM and XPS spectra of small zinc nanoparticle reveal that they are 1.2 nm in diameter and consisted of more than 94 % of non-oxidized zinc atoms. The production of nanometer-sized metallic particles suggests the assembly of a significant number of

metal atoms. The crystal structure of metallic zinc has a hexagonal close-packed lattice with a constant a=b=0.266 nm and c=0.495 nm. The unit cell contains 6 atoms and has a volume of 0.0912 nm^3 (Yoo and Wei 1967). The total volume of the 1.2-nm particle is

$$V_{tot} = \frac{4}{3}\pi(0.6)^3 = 0.904\ nm^3$$

Then, the total number of atoms in the 1.2-nm zinc nanoparticle is estimated to be

$$N_{tot} = \frac{0.904 \times 6}{0.0912} = 59\ atoms$$

One of the remarkable properties of small metal nanoparticles is their stability in water and blood plasma (Samoylov et al. 2005). It was discovered that metal nanoparticles with 13, 55, 147, 309, 561, and 923 atoms, so-called ‘‘magic number’’ of atoms, have added stability. These nanoparticles were designated as full-shell nanoparticles that are constructed by successively packed layers of metal atoms around a single metal atom (Aiken and Finke 1999; Khanna et al. 2002). The percolation of air through the suspension of 1.2 nm zinc nanoparticles for 20 min at 313.15 K caused a modest reduction of non-oxidized zinc atoms to 88% showing a substantial resistance to oxidation. After 317 days of storage of 1.2 nm zinc nanoparticles at 278 K (5^{o}C), the relative atomic concentrations at the beginning and the end of storage did not change. A similar resistance to atmospheric oxidation was observed in the chemically synthesized metallic zinc nanocrystals explained in part by the unique crystalline surface properties of the anisotropic nanoparticles (Mai et al. 2013).

To estimate the number of atoms in the shell of 1.2 nm zinc nanoparticles we find the volume of the shell as a difference between V_{tot} and V_{core}, where

$$V_{core} = \frac{4}{3}\pi(0.6 - \frac{0.495}{2})^3 = 0.183\ nm^3$$

$$V_{shell} = 0.904 - 0.183 = 0.721\ nm^3$$

Then the number of atoms in the shell,

$$N_{shell} = \frac{0.721 \times 6}{0.0912} = 47\ atoms$$

The number of atoms in the core

$$N_{core} = \frac{0.183 \times 6}{0.0912} = 12\ atoms$$

The estimated 12 atoms of the core and the total 59 atoms of the 1.2 nm zinc nanoparticle are in close agreement with the "magic number" full-shell nanoparticles with 13 and 55 atoms. Each metal atom has the maximum number of nearest neighbors, which imparts some degree of extra stability to full-shell clusters (Jena et al. 1996; Aiken and Finke 1999).

The crystal structure of ZnO also has a hexagonal close-packed lattice with constants a=b=0.325 nm and c=0.520 nm. If we assumed the more prevalent form of ZnO with the urzite structure, than it has 2 Zn and 2 O atoms per unit cell, making a total of 4 atoms per cell and a volume of 0.0475 nm^3 (Morkoç and Özgur 2009). The fractions of surface atoms in ZnO nanoparticles are given in Table 2. It is clearly seen from the table, the smaller the size of the particle, the larger the fraction of atoms on the surface. The high surface to volume ratio in some nanoparticles is known to provide high chemical reactivity (Kruyt 1952; Thomas 1988; Matijevic and Goia 2007). The surface atoms of the 1.2 nm zinc nanoparticle account for 80% of all atoms, while the surface of the 15 nm zinc oxide nanoparticle contains only 10% of all atoms (Table 5).

The high surface-volume ratio and fraction surface atoms are important to give a zinc nanoparticle the ability to bind olfactory receptor proteins and create dimers

necessary for the active olfactory receptor-G-protein dimers (Vodyanoy 2010; Moore et al. 2012; Jia et al. 2016). Endogenous zinc nanoparticles supply functional receptor dimers that can be activated by the odorant and take part in the generation of the olfactory signal. The remainder of the monomeric receptors remains largely inactive and do not contribute to the odorant-induced olfactory response. When the olfactory epithelium is exposed to a mixture of zinc nanoparticles and the same odorant, additional receptor dimers are made by joining pairs of previously unbound receptors. The appearance of new receptor dimers will then result in an increase of the odorant-induced olfactory response.

Olfactory receptors belong to the 7-transmembrane receptor superfamily of proteins that have seven domains spanning the plasma membrane seven times and coupled with G-proteins (Buck and Axel 1991). The thickness of the plasma membrane that structurally houses the receptor-G-protein complex is about 5 nm (Mitra et al. 2004). It is speculated that zinc nanoparticles (< 5 nm) bind two of these complexes. The high surface-to-volume ratio of the 1.2 nm zinc nanoparticles should efficiently render coupling between the 2 receptors.

Presently, the most accepted theories of olfaction are either based on molecular shape (Moncrieff 1954; Amoore 1963) or on vibrational properties of molecules (Dyson 1938; Wright 1977; Turin 1996). The first approach, a so-called lock-and-key mechanism, assumes the shape of the molecule determines the characteristic odor. The other suggested that molecular vibrations are the basis for odor specificity in different molecules. In 2011 Franco et al. (Franco et al. 2011) demonstrated that fruit flies (Drosophila melanogaster) can differentiate between regular odorants and their

deuterated isotopes. Two years later, Gane et al. (Gane et al. 2013) reported that humans also are capable of discriminating musk molecules from their deuterated isotopes. As deuteration does not change the shape of a molecule, the lock-and-key model is insufficient to explain those findings. The shape and vibration modes are highly debated and require new experimental and theoretical data (Block et al. 2015; Turin et al. 2015). The enhancement of the olfactory response by zinc nanoparticles is significant in consideration of the Luca Turin's vibrational model that suggests an inelastic electron tunneling spectroscopy mechanism for discriminating odors (Turin 1996). In the inelastic electron tunneling model, the odorant evokes inelastic tunneling of an electron between donor D and acceptor A inside of the receptor. The points D and A differ in energy by $\hbar\omega_o$ (phonon energy), to ensure that tunneling of an electron takes place only if the energy is absorbed by an odorant's phonon. Electron tunneling may result in the G-protein dissociation, which triggers the olfactory signal cascade. The model requires the existence of an active donor of electrons, and it is plausible to propose that zinc nanoparticles act as electron donors (Vodyanoy 2010; Brookes et al. 2012; Jia et al. 2016).

It had been predicted that nanoparticles within the diameter range 1 nm to 10 nm would likely exhibit quantum-mechanical properties (Alivisatos 1996). The arising physical properties are not those of bulk metal nor those of molecular compounds. However, these properties are highly determined by the particle size, interparticle distance, and shape of the nanoparticles (Brust and Kiely 2002). The quantum size effect is manifested if the de Broglie wavelength of the valence electrons is of the same order as the size of the particle itself. Subsequently, the particles act electronically as zero-

dimensional quantum dots (or quantum boxes) highly relevant to quantum-mechanical principles. In nanoparticles, there is a gap between the valence band and the conduction band, in contrast to bulk metals. Single-electron tunnel transitions occur between a donor and acceptor, if the electrostatic energy, $E_{el} = e^2/2C$, is larger than the thermal energy, $E_T = kT$, where C is electric capacitance, e – elementary charge, k – Boltzmann coefficient, T – absolute temperature (Daniel and Astruc, 2004). The capacitance of 2 nm metal particle, $C=4\pi\varepsilon\varepsilon_o r$, where ε is the relative dielectric constant of the receptor protein, (Simonson and Brooks 1996), the ε_o is the vacuum dielectric constant 8.85×10^{-12}, and r=1 nm. $C=4\pi\times9\times8.85\times10^{-12}\times10^{-9}=1.0\times10^{-18}$ F. $E_{el}=(1.6\times10^{-19})^2/(2\times1.0\times10^{-18})=1.15\times10^{-19}$ CV=79.6 meV, that is considerably higher than the thermal energy at 25 ^oC, $E_T = 1.38\times10^{-23}\times298=4.11\times10^{-21}$ J=25.6 meV. Therefore, metal nanoparticles with a diameter smaller than 6 nm satisfy the condition of the single-electron transfer. The single-electron tunnel transition was experimentally observed with ~1 nm quantum dot at room temperature (Barreiro et al. 2012). The above considerations make the hypothesis of small zinc nanoparticles play a role of electron donors in Turin's model (Turin 1996) to be quite feasible.

Discontinuous size effects were experimentally observed in physics of small metal particles studied by the surface plasmon resonance, in the chemistry of supramolecular structures and molecular recognition, and in the biology of DNA-metal nanoparticle assemblies and sensors (reviewed in (Daniel and Astruc 2004). Based on this theoretical and known experimental evidence of the discontinuous size effects, we believe that our experimental results confirm the size influence and surface composition of zinc metal nanoparticles on the enhancement of olfactory odorant responses. We found

that zinc nanoparticles are involved in the initial event of olfaction – interaction with olfactory sensory receptors. However, the signal enhancement at this level is perceived by a central nervous system.

An evaluation of concentration dependency of odorant-stimulated olfactory sensory neuron shows that one zinc nanoparticle binds two receptor molecules to produce a dimer (Vodyanoy 2010). Additionally, there is useful information provided by immunoprecipitation, fluorescence resonance energy transfer, and bioluminescence resonance energy transfer (BRET) that's certainly a fraction of cilia olfactory receptors makes homodimers (Bush 2008; Hall 2009; Wade et al. 2011; Sanz and Pajot-Augy 2013) the same as the rhodopsin homodimerization in optic disc membranes discovered by atomic force microscopy (Fotiadis et al. 2003b; Fotiadis et al. 2003a). We hypothesize that a single receptor cannot be stimulated by the odorant. Instead, only if it is coupled with another receptor with the assistance of a zinc nanoparticle, it can take part in signal transduction. It has been shown by immunogold electron microscopy that only a fraction of the olfactory receptors produces dimers, while all of those other receptors happen to be in the monomer state (Fukutani et al. 2012). Therefore, the enhancement of the olfactory signal by zinc nanoparticles could have a simple explanation. If the olfactory epithelium is challenged with a mixture of zinc nanoparticles and the same odorant, new receptor dimers are made by connecting pairs of formerly unbound receptors. The input of new receptor dimers will then cause a rise of the odorant-evoked olfactory response.

Recently, zinc nanoparticles were shown to enhance rat olfactory odorant responses used in the bio-electronic nose (Zhang et al. 2016). Zinc nanoparticles are not only metal particles that are capable enhancing olfactory odorant response. Exposure to

0.45 μg/L nanosilver suspension led to increased Crucian carp EOG responses, whereas exposure to 45 μg/L silver nanoparticle suspension and silver ion solution resulted in suppressing EOG signals (Bilberg et al. 2011). Other studies confirm toxicity of silver nanoparticles and silver ions (Bilberg et al. 2010; Farmen et al. 2012). Intranasal zinc sulfate irrigation in mmol/L concentrations in rodents was shown to destroy olfactory receptors (Matulionis 1975; Burd 1993). In contrast, zinc nanoparticles did not manifest toxicity at the fractions of nmol/L concentrations are not toxic to astrocytes (Vodyanoy et al. 2016).

6.4.1. Characterization and temperature-resistance of PEGylated nanoparticles

The crystalline structure of zinc nanoparticles revealed in this work is consistent with those obtained for zinc nanowires and nanorods (Chen 2007, Lu 2016). The equivalence of the zinc lattices and core lattices of PEGylated zinc nanoparticles indicates that PEGylating maintains the crystalline nature of the metal particles. To further analyze physical properties of the non-PEGylated and PEGylated zinc nanoparticles, XPS was utilized for study of nanoparticles in the variety of temperatures and storage periods.

The decrease in the binding energy of Zn $2p_{3/2}$ peaks in the ZnPEG400 and PEG1000 nanoparticles and the rise in the amplitude of the XPS C-O peak validated that PEGylation of zinc nanoparticles was successful. The Zn $2p_{3/2}$ band shows that metallic zinc nanoparticles were oxidized only slightly, where the concentrations of Zn and ZnO were found to be 97.0 ± 0.8 (SD) % and 3.0 ± 0.8 (SD) %, respectively (Table 2, 278 K, 1 day). The interaction of the PEG molecules and zinc nanoparticles had a remarkable

effect on the binding energies of carbon and zinc. Bonding of the molecules onto the nanoparticles was associated with an increase in the binding energy of the C-O bond, and a corresponding decrease in the ZnO binding energy.

For the nanoparticles held at 278 K for 1 day, the C-O binding energy increased from 286.2 eV to 286.9 eV (by roughly 0.7 eV) while the ZnO binding energy decreased by 0.9 eV when the nanoparticles were covered by PEG400. A similar shift in binding energies were observed for the nanoparticles covered in PEG1000. We speculate that the PEG molecules are interacting with the zinc atoms in such a way that the electronic structure of the nanoparticles is affected, and a conjugated electron system is produced (Mason 1983). It is likely that long polymer chains increase the withdrawal of electron charge and electronic stability, which subsequently increases the binding energy of the C and O elements within the chain (Duan 2016). Conversely, the polymer chains may act as a passivation layer that leads to a reduction in binding energy because the zinc nanoparticles are acting as electron donors, which has been observed for platinum nanoparticles below 7 nm in size (Qiu & Liu 2006).

The highest shift in binding energy was observed for ZnPEG400 nanoparticles stored at 278 K for 317 days. The binding energy of the C-O component increased by 0.9 eV relative to the control value of 286.2 eV, and a corresponding decrease in binding energy of 0.7 eV was seen for ZnO. Similar shifts in binding energy were also observed for PEGylated zinc nanoparticles exposed to elevated temperatures of 303 K (30 ^{o}C) and 323 K (50 ^{o}C). These observations point to the covalent binding of PEG to the engineered zinc nanoparticles, with similar binding energy shifts observed after PEGylation of MoS_2

nanoflakes (Wang 2015, Feng 2015), gadolinium oxide thin film and nanoparticles (Guay-Begin 2012), and gold nanorods (Thierry 2009).

The activation energy calculated for the oxidation of zinc nanoparticles is consistent with that obtained by the oxidation of zinc foil (Moore 1951), the oxygen desorption from ZnO powder, and the oxidation of molten zinc (Cope 1961). After PEGylation, zinc nanoparticles showed reduction of oxidation when exposed to increased temperatures, with the binding of PEG400 inducing more stability compared to PEG1000. No literature was available for comparison of the activation energy of the PEGylated zinc nanoparticles. However, a decrease in the activation energy was reported when 60-100 nm Pd/Fe nanoparticles underwent PEGylation (Wang 2015). The reduction of the nanoparticle surface charge after PEGylation may explain an increased affinity to target proteins (Jokerst, Lobovkina et al. 2011).

Previously, we showed that primarily-elemental zinc nanoparticles strongly enhanced responses to odorants, while oxidized zinc nanoparticles did not enhance but rather slightly inhibited the responses (11.5% ZnO compared to 3.0% for the primarily-elemental nanoparticle) (Hagerty, Daniels et al. 2016). The olfactory enhancement of approximately 140% using ZnPEG400 after 317 days of storage was not an anticipated result. Although no significant change in the C-O concentration was observed, the C-C concentration decreased from 3.7% to 0.9%. The increase in the observed level of ZnO in this case does not imply a high level of oxidized zinc atoms, but rather seems to reveal that there is a formation of a unique conjugated electron system between the zinc nanoparticles and PEG400 molecules that may be responsible for the increase in olfactory response.

The addition of the ZnPEG400 nanoparticles to odorant at the end of 317 days of storage at 278 K (5^{o}C) resulted in the highest relative EOG enhancement that was larger than enhancement by the un-PEGylated zinc nanoparticles. This amplified enhancement can be explained by the increased binding affinity to olfactory receptors in part due to the reduction of the surface charge as it was manifested by the reduction of zeta potential and because of the increase of hydrophobicity (Mu, Jiang et al. 2014). Additionally, XPS data indicate covalent binding between PEG400 and zinc nanoparticles that may cause oxidative coupling between the PEG molecules and zinc atoms on the surface of zinc nanoparticles. The combined electron system may be more efficient in donating electrons than non-PEGylated zinc nanoparticles and therefore contributed to the amplified olfactory enhancement. The signal amplification effects for combined electron system was reported for PEGylated electrodes (Doneux 2016, Hotchen 2015, Nekoueian 2015). All the above properties of ZnPEG400 (increased binding affinity, combined zinc-PEG electron system, and favorable electron transmission probability) provide an explanation for the amplified olfactory enhancement compared to non-PEGylated zinc nanoparticles.

The XPS analysis of the ZnPEG1000 after long storage indicated that they did not produce a conjugated electron system, and therefore they do not have the advantage of facile electron donation compared to non-PEGylated zinc. This observation may be explained by the length, viscosity, and rigidity of PEGs. PEG400 with ~9 monomer repeats (as opposed to ~23 repeats in PEG1000) has a lower viscosity and rigidity than those of PEG1000 (Wang 2009). With the lower viscosity and rigidity, the PEG 400 can enable a more intimate interaction with the olfactory sensory receptors. Moreover, being a shorter

molecule the PEG400 produced a thinner layer around the zinc nanoparticle. The estimated transmission probability of electron transfer through the PEG400 layer was approximately 4 times higher than that of the PEG1000. The PEG400 layer, therefore, can provide the sufficient electron transfer for the olfactory transaction, while PEG1000 is much less efficient. ZnPEG1000 nanoparticles showed negative relative EOG signals post 280 days incubation because they compete with the endogenous zinc nanoparticles for binding sites in the olfactory receptors. The ZnPEG1000 nanoparticles occupied the receptor binding sites that were intended for endogenous zinc nanoparticles. This binding resulted in the receptor dimers that were not capable of triggering the signal transaction because zinc nanoparticles could not transfer electrons through the PEG1000 layers.

The relative enhancement of zinc nanoparticles had a non-monotonic dependence on the time of storage. The freshly prepared particles had the highest enhancement. The enhancement declined on day 3 and then increased again on day 5. This non-monotonic behavior cannot be explained through the animal to animal variability. The amplitude of the electrical signals varies from cell to cell and from animal to animal (Firestein, Picco et al. 1993). The EOG measured at the different contact points of OE may have a different amplitude. However, the earlier measurements showed that the correctly normalized relative values of the epithelial electrical signals were conserved amongst the single animal and different animals of the same age and breed (Ottoson 1955; Scott and Scott-Johnson 2002). This fact allowed the use of different animals to quantitatively characterize initial olfactory events. We previously used this approach to characterize the effects of different odorants at various concentrations and evaluate the effects of zinc nanoparticles (Viswaprakash, Dennis et al. 2009). We further showed that the cultured

olfactory neurons initially obtained from different mouse pups also conserved the EOG kinetic properties of the neurons at the same age. For these cultured neurons, zinc nanoparticles enhanced EOG responses of both younger and older cultures (Viswaprakash, Josephson et al. 2010).

We speculate that non-monotonic dependence of an olfactory enhancement by zinc nanoparticles can be attributed to the time-dependent changes in the electronic structure of the nanoparticles related to the relaxation and diffusion of atoms. Indeed, taking into the account that the self-diffusion coefficient of zinc in the single zinc crystal at 278 K is 7.7×10^{-22} m^2/s (Banks 1941), it would take ~31 h to move a zinc atom the distance of 1.2 nm. This time is consistent with the time of the initial decline in the relative olfactory enhancement. Zinc nanoparticles of 1.2 nm in diameter contain ~59 zinc atoms (47 atoms in the shell and 12 atoms in core) (Hagerty, Daniels et al. 2016). The freshly prepared zinc nanoparticles may be all in the non-oxidized state and produce the maximal olfactory enhancement. The present XPS data showed that in one day, 3% of zinc atoms of the primarily-elemental zinc nanoparticles, or ≈2 atoms are ZnO. Being in the shell of nanoparticles, ZnO may cause an initial decline in the olfactory enhancement. After a further storage, zinc atoms diffused from the shell to the core and no longer interacted with olfactory receptors. The detrimental effect of ZnO on olfactory enhancement could be similar to that reported for cancer cells treated with the non-thermal atmospheric-pressure plasma particles that caused cell death by alteration of antioxidant activity (Kaushik 2014). Likewise, the polymeric membrane with ZnO particles is described to offer antibacterial activity (Nasaipour and Ansari). The non-monotonic dependence on particle size, shape, support, composition, and oxidation state

was found in the catalytic properties of metal nanoparticles (Cuenya 2010) and the effects of metal nanoparticles on biological systems (Boldvreva 2014).

The mechanism of the amplified enhancement by PEG400 coating of zinc nanoparticles exposed to elevated temperatures is similar to that of the enhancement by ZnPEG400 nanoparticles subjected to long-term storage at 278 K (5^{o}C). The XPS spectra of ZnPEG400 subjected to elevated temperature showed similar features to the nanoparticles stored for longer times. These observations provide evidence for the large number of covalently bound species and production of a conjugated electron system of zinc nanoparticles and PEG400 molecules. The mechanism of the amplified enhancement produced by the ZnPEG400 after heating are similar to those described for these particles after prolonged storage. Although PEG reduces oxidation of elemental zinc both for 400 g/mol and 1000 g/mol molecules, the PEG1000 coating causes a considerable increase in the coating thickness which consequently reduces the enhancement of the odorant response.

We can conclude that small ~1.2 nm diameter non-oxidized primarily-elemental zinc nanoparticles produced enhancement of responses to odorants, as verified by physiological experiments, whereas air-oxidized zinc nanoparticles inhibit olfaction. When the zinc nanoparticles were covered with thin layers of polyethylene glycol of molecular weight 400 g/mol and 1000 g/mol (ZnPEG400 and ZnPEG1000), the PEGylation preserved the nanoparticles from oxidation while conserving their crystalline structure. PEGylation maintains the ability of the zinc nanoparticles to enhance the olfactory response to the odorant. The polyethylene glycol molecules by themselves produced a small olfactory response inhibition when delivered with the odorant and did

not produce a noticeable effect when applied without odorant. The ZnPEG400 nanoparticles continued to manifest the amplified enhancement of odorant response even after a 300-days storage at 278 K (5^{o}C), while ZnPEG1000 nanoparticles produced an inhibition under the same conditions. ZnPEG400 withstood two-day storage at 303 K (30^{o}C) and 323 K (50^{o}C) and evoked the adequate enhancement of olfaction, but ZnPEG1000 showed a reduced enhancement at the same conditions. The PEG400 appeared to be far better for preservation of properties of zinc nanoparticles for long term storage and elevated temperatures. The enhancement and inhibition of olfaction by zinc nanoparticles preserved by PEGylation were consistent with Turin's model of olfaction. The novelty of this work is that biocompatible and safe PEG400 coat of zinc nanoparticles provides both preservation of particles and amplification of olfactory enhancement.

6.5. Future Directions

Overall, this work has contributed to the knowledge that one of the many physiological systems affected by heat stress is the olfactory system. We have focused directly on the olfactory epithelium, including evaluation of electrical responses and histological analysis. Additionally, we found that thermal stress also has detrimental oxidative consequences on zinc nanoparticles, which are thought to be closely involved at the receptor site during the initial events of olfaction. This work demonstrated consistent kinetic shifts toward faster cellular signal activation-deactivation when animals were exposed to environmental and exertional heat stress. While we cannot determine at this point whether temperature exposure is altering the binding event during receptor activation, or altering the odorant release during signal termination, we have demonstrated that the overall depolarization and repolarization process is occurring at a faster rate when body temperature is higher.

We also demonstrated that similar shifts in EOG kinetics occur even when olfactory epithelia isolated from non-stressed rats was exposed to higher temperatures. This suggests that the observed kinetic shifts may not only be the result of systemic interactions involving the immune secretions or microbiota. Exposing OE isolated from non-stressed rats to various temperatures resulted in changes in EOG trace stability, amplitude, and kinetics.

Relating kinetic and thermodynamic parameters resulted in quantitative information suggesting potential molecular conformational changes occurring between the odorant and receptor. The second law of thermodynamics states that energy of all

kinds (potential, kinetic, thermal, electrical, etc.) disperses if it is not hindered. Important quantitative measures of this law, including reaction rate, activation energy, entropy, enthalpy, entropy contribution, and free energy were calculated for every temperature shift in our EOG data. The averages we obtained, most notably the large entropy values, very small activation energy, and moderate-low free energy, suggest a few things about the energetic shifts when thermal energy is applied to the system. First, the large entropy values indicate a decrease in molecular rotational degrees of freedom of the OR binding pocket and suggest that the binding/deactivation events at the receptor level are entropy-driven. The very miniscule activation energies suggest a reduced transition state barrier, also referred to as "barrierless" or "activationless" reaction, which may indicate easier access to the binding site for odorants and fast activation and adaptation with higher frequencies of odorants about the epithelial surface.

Histological analysis of the epithelial tissue showed structural changes and reduced density of mature olfactory sensory neurons. Using immunofluorescence to tag OMP, we saw slight changes in morphology, including a damaged appearance as OSNs were out of place and in disarray in contrast to the non-stressed epithelia.

This work also contributed preliminary evidence that probiotics may exert biochemical changes, either systemically or directly within the nasal cavity, that facilitate slower activation-deactivation of olfactory sensory neurons. This information does not necessarily suggest any type of protective effect, as the increased kinetics does not show that olfactory function is dampened in any way. However, it merely demonstrates a shift back towards normal function under non-stressed conditions.

Taken together, the results reported here have contributed to this underdeveloped research question, but there is still a great deal of work that must be done to repeat and supplement these experiments. Some specific areas that should be addressed in future work include investigating specific molecular activity at the receptor level during heat stress by manipulating the GPCR cascade. Molecular characterizations of this sort should be carried out for each method of heat stress and compared, so that a more thorough understanding of what specific mechanisms are altering kinetics of EOG responses for each heat stress event can be reached.

Some limitations of our experiments could be addressed and improved in further work. For example, while our experiments have been carried out over a four-year period and often included a collaboration of projects at one time, controls in some experiments were not as thoroughly specific as they could have been. This could be improved in future work. For the purposes of these preliminary experiments, it was important to follow IACUC protocol guidelines to limit the number of animals used just enough to meet statistical standards, as our surgeries are terminal and hundreds of thousands of data points can be gathered from one EOG recording.

Chapter 7 – Conclusions

1. Exposing rats to heat stress conditions resulted in a kinetic shift of electrical activity (EOG), showing faster rise and decay response times.
2. Exposing olfactory epithelia isolated from non-stressed rats to various temperatures resulted in a change in EOG response stability, amplitude, and calculated thermodynamic parameters with increasing temperatures.
3. The thermodynamic processes associated with EOG responses are entropy driven, and the large entropy values calculated from these experiments indicate a decrease in molecular rotational and translational degrees of freedom of the olfactory receptor binding pocket – potentially allowing easier access for ligand binding.
4. The activation energy and enthalpy are small compared to the entropy contribution and free energy, suggesting reduced transitional barrier of olfactory receptor for odorant binding.
6. 1.2 nm zinc nanoparticles are suggested to serve as donors of electrons in Turin's vibrational model of olfaction. Temperature stress increased the oxidation of zinc nanoparticle preparations, after which they lost the ability to enhance responses to odorant stimulation.
7. When zinc nanoparticles are covered with thin layers of polyethylene glycol of molecular weight 400 g/mol and 1000 g/mol (ZnPEG400 and ZnPEG1000), the PEGylation preserved the nanoparticles from oxidation due to storage time and temperature exposure, while conserving their crystalline structure. PEGylation

maintains the ability of the zinc nanoparticles to enhance the olfactory response to the odorant. ZnPEG400 withstood two-day storage at 303 K (30^{o}C) and 323 K (50^{o}C) and evoked the adequate enhancement of olfaction. The PEG400 appeared to be far better for preservation of properties of zinc nanoparticles for long term storage and elevated temperatures.

References

Abolmaali, N., T. Hummel, et al. (2009). "[Two- and three-dimensional, morphologic and functional MR-imaging in smelling disorders]." Laryngorhinootologie **88**(1): 10-6.

Abruzzo, P. M., F. Esposito, et al. (2013). "Moderate exercise training induces ROS-related adaptations to skeletal muscles." Int J Sports Med **34**(8): 676-87.

Aggett, P. J. (1985). "Physiology and metabolism of essential trace elements: an outline." Clin Endocrinol Metab **14**(3): 513-43.

Ait-Belgnaoui, A., A. Colom, et al. (2014). "Probiotic gut effect prevents the chronic psychological stress-induced brain activity abnormality in mice." Neurogastroenterol Motil **26**(4): 510-20.

Anand, A. S., D. N. Prasad, et al. (2017). "Chronic exposure of zinc oxide nanoparticles causes deviant phenotype in Drosophila melanogaster." J Hazard Mater **327**: 180-186.

Anderson, A. K., K. Christoff, et al. (2003). "Dissociated neural representations of intensity and valence in human olfaction." Nat Neurosci **6**(2): 196-202.

Anselmi, C., A. Buonocore, et al. (2011). "The human olfactory receptor 17-40: Requisites for fitting into the binding pocket." Computational Biology and Chemistry **35**(3): 159-168.

Balasubramanian, S., J. W. Lynch, et al. (1996). "Calcium-dependent Modulation of the Agonist Affinity of the Mammalian Olfactory Cyclic Nucleotide-gated Channel by Calmodulin and a Novel Endogenous Factor." The Journal of Membrane Biology **152**(1): 13-23.

Banci, L. and I. Bertini (2013). "Metallomics and the cell: some definitions and general comments." Met Ions Life Sci **12**: 1-13.

Baumann, H., T. G. Urmantscheeva, et al. (1977). "Evaluation of central nervous adaptability to low stress and high stress categories in rhesus monkeys by multivariate evoked potential analyses [proceedings]." Act Nerv Super (Praha) **19**(4): 315-7.

Berstad, K. and J. E. R. Berstad (2017). "Parkinson's disease; the hibernating spore hypothesis." Med Hypotheses **104**: 48-53.

Bharwani, A., M. F. Mian, et al. (2017). "Oral treatment with Lactobacillus rhamnosus attenuates behavioural deficits and immune changes in chronic social stress." BMC Med **15**(1): 7.

Bienenstock, J., W. Kunze, et al. (2015). "Microbiota and the gut-brain axis." Nutr Rev **73 Suppl 1**: 28-31.

Bienenstock, J., W. A. Kunze, et al. (2017). "Disruptive physiology: olfaction and the microbiome-gut-brain axis." Biol Rev Camb Philos Soc **93**(1): 390-403.

Blechinger, S. R., R. C. Kusch, et al. (2007). "Brief embryonic cadmium exposure induces a stress response and cell death in the developing olfactory system followed by long-term olfactory deficits in juvenile zebrafish." Toxicol Appl Pharmacol **224**(1): 72-80.

Boccaccio, A., L. Lagostena, et al. (2006). "Fast adaptation in mouse olfactory sensory neurons does not require the activity of phosphodiesterase." J Gen Physiol **128**(2): 171-84.

Boekhoff, I. and H. Breer (1992). "Termination of second messenger signaling in olfaction." Proc Natl Acad Sci U S A **89**(2): 471-4.

Boekhoff, I., E. Tareilus, et al. (1990). "Rapid activation of alternative second messenger pathways in olfactory cilia from rats by different odorants." EMBO J **9**(8): 2453-8.

Borisy, F., G. Ronnett, et al. (1992). "Calcium/calmodulin-activated phosphodiesterase expressed in olfactory receptor neurons." J Neurosci **12**(3): 915-923.

Bradley, J. R., Johannes; Frings, Stephan (2005). "Regulation of cyclic nucleotide-gated channels." Current Opinion in Neurobiology **15**(3): 343-349.

Brauchi, S., P. Orio, et al. (2004). "Clues to understanding cold sensation: Thermodynamics and electrophysiological analysis of the cold receptor TRPM8." Proceedings of the National Academy of Sciences of the United States of America **101**(43): 15494-15499.

Bravo, J. A., M. Julio-Pieper, et al. (2012). "Communication between gastrointestinal bacteria and the nervous system." Curr Opin Pharmacol **12**(6): 667-72.

Breer, H. (2003). "Olfactory receptors: molecular basis for recognition and discrimination of odors." Anal Bioanal Chem **377**(3): 427-433.

Breer, H. (2003). "Sense of smell: recognition and transduction of olfactory signals." Biochem Soc Trans **31**: 113-116.

Bruchim, Y., I. Aroch, et al. (1985). "Two years of combined high-intensity physical training and heat acclimatization affect lymphocyte and serum HSP70 in purebred military working dogs." J Appl Physiol (1985) **117**(2): 112-8.

Buck, L. and R. Axel (1991). "A novel multigene family may encode odorant receptors: a molecular basis for odor recognition." Cell **65**(1): 175-87.

Buck, L. and R. Axel (1991). "A novel multigene family may encode odorant receptors: a molecular basis for odor recognition." Cell **65**(1): 175-87.

Buck, L. B. (1992). "The olfactory multigene family." Curr Opin Genet Dev **2**(3): 467-73.

Buck, L. B. (1993). "Receptor diversity and spatial patterning in the mammalian olfactory system." Ciba Found Symp **179**: 51-64; discussion 64-7, 88-96.

Buck, L. B. (1996). "Information coding in the vertebrate olfactory system." Annu Rev Neurosci **19**: 517-44.

Buiakova, O. I., H. Baker, et al. (1996). "Olfactory marker protein (OMP) gene deletion causes altered physiological activity of olfactory sensory neurons." Proc Natl Acad Sci U S A **93**(18): 9858-63.

Burokas, A., R. D. Moloney, et al. (2015). "Microbiota regulation of the Mammalian gut-brain axis." Adv Appl Microbiol **91**: 1-62.

Busse, D., P. Kudella, et al. (2014). "A synthetic sandalwood odorant induces wound-healing processes in human keratinocytes via the olfactory receptor OR2AT4." J Invest Dermatol **134**(11): 2823-2832.

Chapuis, J., Y. Cohen, et al. (2013). "Lateral entorhinal modulation of piriform cortical activity and fine odor discrimination." J Neurosci **33**(33): 13449-59.

Chen, J., Y. Li, et al. (2015). "Interaction between Microbes and Host Intestinal Health: Modulation by Dietary Nutrients and Gut-Brain-Endocrine-Immune Axis." Curr Protein Pept Sci **16**(7): 592-603.

Chen, T. Y. and K. W. Yau (1994). "Direct modulation by Ca(2+)-calmodulin of cyclic nucleotide-activated channel of rat olfactory receptor neurons." Nature **368**(6471): 545-8.

Cui, T., A. V. Tsolakis, et al. (2013). "Olfactory receptor 51E1 protein as a potential novel tissue biomarker for small intestine neuroendocrine carcinomas." Eur J Endocrinol **168**(2): 253-61.

Dalpiaz, A., A. Scatturin, et al. (2000). "Binding thermodynamics and intrinsic activity of adenosine A1 receptor ligands." Life Sci **67**(12): 1517-24.

Delgado, R., C. Vergara, et al. (2006). "Divalent cations as modulators of neuronal excitability: emphasis on copper and zinc." Biol Res **39**(1): 173-82.

Dibattista, M. and J. Reisert (2016). "The Odorant Receptor-Dependent Role of Olfactory Marker Protein in Olfactory Receptor Neurons." J Neurosci **36**(10): 2995-3006.

Dillon, R. J., C. T. Vennard, et al. (2002). "A note: gut bacteria produce components of a locust cohesion pheromone." J Appl Microbiol **92**(4): 759-63.

Diverio, S., G. Guelfi, et al. (2015). "Non-invasive assessment of animal exercise stress: real-time PCR of GLUT4, COX2, SOD1 and HSP70 in avalanche military dog saliva." Animal **9**(1): 104-9.

Dragan, A. I., J. Klass, et al. (2003). "DNA Binding of a Non-sequence-specific HMG-D Protein is Entropy Driven with a Substantial Non-electrostatic Contribution." Journal of Molecular Biology **331**(4): 795-813.

Eyring, H., S. Lin, et al. (1980). Basic chemical kinetics. . New York, John Wiley & Sons.

Feldmesser, E., T. Olender, et al. (2006). "Widespread ectopic expression of olfactory receptor genes." Bmc Genomics **7**: 121.

Firestein, S. (2001). "How the olfactory system makes sense of scents." Nature **413**(6852): 211-8.

Firestein, S., C. Picco, et al. (1993). "The relation between stimulus and response in olfactory receptor cells of the tiger salamander." J Physiol **468**: 1-10.

Firestein, S. and F. Zufall (1993). "Membrane currents and mechanisms of olfactory transduction." Ciba Found Symp **179**: 115-26; discussion 126-30, 147-9.

Fleischer, J., K. Mamasuew, et al. (2009). "Expression of cGMP signaling elements in the Grueneberg ganglion." Histochem Cell Biol **131**(1): 75-88.

Fletcher, M. L., A. V. Masurkar, et al. (2009). "Optical imaging of postsynaptic odor representation in the glomerular layer of the mouse olfactory bulb." J Neurophysiol **102**(2): 817-30.

Forsythe, P., J. Bienenstock, et al. (2014). "Vagal pathways for microbiome-brain-gut axis communication." Adv Exp Med Biol **817**: 115-33.

Forsythe, P., W. A. Kunze, et al. (2012). "On communication between gut microbes and the brain." Curr Opin Gastroenterol **28**(6): 557-62.

Francois, A., D. Grebert, et al. (2016). "Olfactory epithelium changes in germfree mice." Sci Rep **6**: 24687.

Frederick, K. K., M. S. Marlow, et al. (2007). "Conformational entropy in molecular recognition by proteins." Nature **448**(7151): 325-9.

Fukuda, N., K. Yomogida, et al. (2004). "Functional characterization of a mouse testicular olfactory receptor and its role in chemosensing and in regulation of sperm motility." J Cell Sci **117**(Pt 24): 5835-45.

Gerlach, L. O., J. S. Jakobsen, et al. (2003). "Metal ion enhanced binding of AMD3100 to Asp262 in the CXCR4 receptor." Biochemistry **42**(3): 710-7.

Getz, W. M. (1999). "A kinetic model of the transient phase in the response of olfactory receptor neurons." Chem Senses **24**(5): 497-508.

Giblot Ducray, H. A., L. Globa, et al. (2016). "Mitigation of heat stress-related complications by a yeast fermentate product." J Therm Biol **60**: 26-32.

Gold, G. H. (1999). "Controversial issues in vertebrate olfactory transduction." Annu Rev Physiol **61**: 857-71.

Griffin, C. A., K. A. Kafadar, et al. (2009). "MOR23 promotes muscle regeneration and regulates cell adhesion and migration." Dev Cell **17**(5): 649-61.

Griffiths, D. J. (1995). Introduction to Quantum Mechanics. Upper Saddle River, New Jersey, Prentice Hall.

Gupta, S. and A. Auerbach (2011). "Temperature dependence of acetylcholine receptor channels activated by different agonists." Biophys J **100**(4): 895-903.

Gupta, S. and A. Auerbach (2011). "Temperature Dependence of Acetylcholine Receptor Channels Activated by Different Agonists." Biophysical Journal **100**(4): 895-903.

Haberly, L. B. (2001). "Parallel-distributed processing in olfactory cortex: new insights from morphological and physiological analysis of neuronal circuitry." Chem Senses **26**(5): 551-76.

Hagerty, S., Y. Daniels, et al. (2016). "After oxidation, zinc nanoparticles lose their ability to enhance responses to odorants." Biometals **29**(6): 1005-1018.

Hagerty, S., Y. Daniels, et al. (2016). "After oxidation, zinc nanoparticles lose their ability to enhance responses to odorants." Biometals **29**(6): 1005-1018.

Hanada, T., M. Kashiwayanagi, et al. (1994). "Temperature increase abolishes ability of turtle olfactory receptors to discriminate similar odorant." Am J Physiol **266**(6 Pt 2): R1816-23.

Hassan, S. and A. V. Singh (2014). "Biophysicochemical perspective of nanoparticle compatibility: a critically ignored parameter in nanomedicine." J Nanosci Nanotechnol **14**(1): 402-14.

Henkin, R. I., B. M. Patten, et al. (1975). "A syndrome of acute zinc loss. Cerebellar dysfunction, mental changes, anorexia, and taste and smell dysfunction." Arch Neurol **32**(11): 745-51.

Herbert, R. P., J. Harris, et al. (2012). "Cytokines and olfactory bulb microglia in response to bacterial challenge in the compromised primary olfactory pathway." J Neuroinflammation **9**: 109.

Hildebrand, J. G. and G. M. Shepherd (1997). "Mechanisms of olfactory discrimination: converging evidence for common principles across phyla." Annu Rev Neurosci **20**: 595-631.

Holst, B., C. E. Elling, et al. (2002). "Metal ion-mediated agonism and agonist enhancement in melanocortin MC1 and MC4 receptors." J Biol Chem **277**(49): 47662-70.

Horowitz, L. F., L. R. Saraiva, et al. (2014). "Olfactory receptor patterning in a higher primate." J Neurosci **34**(37): 12241-52.

Horowitz, M. and E. Kodesh (2010). "Molecular signals that shape the integrative responses of the heat-acclimated phenotype." Med Sci Sports Exerc **42**(12): 2164-72.

Hummel, T., M. Knecht, et al. (1996). "Peripherally obtained electrophysiological responses to olfactory stimulation in man: electro-olfactograms exhibit a smaller degree of desensitization compared with subjective intensity estimates." Brain Res **717**(1-2): 160-4.

Ichimura, A., T. Kadowaki, et al. (2008). "In silico approach to identify the expression of the undiscovered molecules from microarray public database: identification of odorant receptors expressed in non-olfactory tissues." Naunyn Schmiedebergs Arch Pharmacol **377**(2): 159-65.

Illum, L., A. E. Church, et al. (2001). "Development of systems for targeting the regional lymph nodes for diagnostic imaging: in vivo behaviour of colloidal PEG-coated magnetite nanospheres in the rat following interstitial administration." Pharm Res **18**(5): 640-5.

Jaworsky, D. E., O. Matsuzaki, et al. (1995). "Calcium modulates the rapid kinetics of the odorant-induced cyclic AMP signal in rat olfactory cilia." J Neurosci **15**(1 Pt 1): 310-8.

Jia, H., O. M. Pustovyy, et al. (2014). "Functional MRI of the olfactory system in conscious dogs." PLoS One **9**(1): e86362.

Jia, H., O. M. Pustovyy, et al. (2016). "Enhancement of Odor-Induced Activity in the Canine Brain by Zinc Nanoparticles: A Functional MRI Study in Fully Unrestrained Conscious Dogs." Chem Senses **41**(1): 53-67.

Jokerst, J. V., T. Lobovkina, et al. (2011). "Nanoparticle PEGylation for imaging and therapy." Nanomedicine (Lond) **6**(4): 715-28.

Jones, D. T., S. B. Masters, et al. (1990). "Biochemical characterization of three stimulatory GTP-binding proteins. The large and small forms of Gs and the olfactory-specific G-protein, Golf." J Biol Chem **265**(5): 2671-6.

Kabra, K., A. A. Sonkamble, et al. (2015). "Dynamics of polymer matrix in non-polar solvent Using TDR Technique." BIONANO FRONTIER Vol. 8 (3) December 2015 **8**(3): 378-380.

Kadohisa, M. and D. A. Wilson (2006). "Separate encoding of identity and similarity of complex familiar odors in piriform cortex." Proc Natl Acad Sci U S A **103**(41): 15206-11.

Kang, N., Y. Y. Bahk, et al. (2015). "Olfactory receptor Olfr544 responding to azelaic acid regulates glucagon secretion in alpha-cells of mouse pancreatic islets." Biochem Biophys Res Commun **460**(3): 616-21.

Kang, N. and J. Koo (2012). "Olfactory receptors in non-chemosensory tissues." BMB Rep **45**(11): 612-22.

Karakoti, A. S., S. Das, et al. (2011). "PEGylated inorganic nanoparticles." Angew Chem Int Ed Engl **50**(9): 1980-94.

Kim, S. H., Y. C. Yoon, et al. (2015). "Expression of human olfactory receptor 10J5 in heart aorta, coronary artery, and endothelial cells and its functional role in angiogenesis." Biochem Biophys Res Commun **460**(2): 404-8.

Kleene, S. J. (2008). "The Electrochemical Basis of Odor Transduction in Vertebrate Olfactory Cilia." Chem. Senses **33**: 839-859.

Kludt, E., C. Okom, et al. (2015). "Integrating temperature with odor processing in the olfactory bulb." J Neurosci **35**(20): 7892-902.

Koce, A. and T. Valentincic (2000). "The amplitude of the electroolfactogram in catfish correlates with the proportion of responding ORNs." Pflugers Archiv-European Journal of Physiology **439**(3): R171-R172.

Konturek, P. C., S. J. Konturek, et al. (2004). "Neuroendocrinology of gastric H+ and duodenal HCO3- secretion: the role of brain-gut axis." Eur J Pharmacol **499**(1-2): 15-27.

Koskinen, K., J. L. Reichert, et al. (2018). "The nasal microbiome mirrors and potentially shapes olfactory function." Sci Rep **8**(1): 1296.

Krishtalik, L. I. (1969). "On the conditions favourable to the detection of barrierless electrode processes." Journal of Electroanalytical Chemistry and Interfacial Electrochemistry **21**(3): 421-424.

Krishtalik, L. I. (2016). "The hydrogen overpotential-hydrogen adsorption energy relationship. A new approach to the problem." Electrochimica Acta **218**: 125-132.

Kyathanahally, S. P., H. Jia, et al. (2015). "Anterior-posterior dissociation of the default mode network in dogs." Brain Struct Funct **220**(2): 1063-76.

Lamb, T. D. and E. N. Pugh, Jr. (1992). "G-protein cascades: gain and kinetics." Trends Neurosci **15**(8): 291-8.

Lancet, D. and U. Pace (1987). "The Molecular-Basis of Odor Recognition." Trends Biochem Sci **12**(2): 63-66.

Lapid, H. and T. Hummel (2013). "Recording odor-evoked response potentials at the human olfactory epithelium." Chem Senses **38**(1): 3-17.

Lapid, H. and T. Hummel (2013). "Recording Odor-Evoked Response Potentials at the Human Olfactory Epithelium." Chemical Senses **38**(1): 3-17.

Lapid, H., H. S. Seo, et al. (2009). "Odorant Concentration Dependence in Electroolfactograms Recorded From the Human Olfactory Epithelium." Journal of Neurophysiology **102**(4): 2121-2130.

Lee, A. C., J. He, et al. (2011). "Olfactory marker protein is critical for functional maturation of olfactory sensory neurons and development of mother preference." J Neurosci **31**(8): 2974-82.

Leon, L. R., C. J. Gordon, et al. (2010). "Thermoregulatory, behavioral, and metabolic responses to heatstroke in a conscious mouse model." Am J Physiol Regul Integr Comp Physiol **299**(1): R241-8.

Leon, L. R. and B. G. Helwig (2010). "Heat stroke: role of the systemic inflammatory response." J Appl Physiol (1985) **109**(6): 1980-8.

Leon, L. R. and B. G. Helwig (2010). "Role of endotoxin and cytokines in the systemic inflammatory response to heat injury." Front Biosci (Schol Ed) **2**: 916-38.

Lev, I. K. (1965). "BARRIERLESS ELECTRODE PROCESSES." Russian Chemical Reviews **34**(10): 785.

Levine, R. D. (2001). "On the capture cross-section for charge neutralization, recombination, photoassociation and other barrierless reactions." Chemical Physics **270**(1): 129-132.

Mackay-Sim, A., L. Grant, et al. (2004). "Australian norms for a quantitative olfactory function test." J Clin Neurosci **11**(8): 874-9.

Mamasuew, K., H. Breer, et al. (2008). "Grueneberg ganglion neurons respond to cool ambient temperatures." Eur J Neurosci **28**(9): 1775-85.

Mamasuew, K., N. Hofmann, et al. "Chemo- and thermosensory responsiveness of Grueneberg ganglion neurons relies on cyclic guanosine monophosphate signaling elements." Neurosignals **19**(4): 198-209.

Matthews, H. R. and J. Reisert (2003). "Calcium, the two-faced messenger of olfactory transduction and adaptation." Current Opinion in Neurobiology **13**(4): 469-475.

Mizutani, T., M. Sahara, et al. (2000). "[Intracellular calcium kinetics after odorant stimulus in olfactory receptor cells isolated from mice]." Nihon Jibiinkoka Gakkai Kaiho **103**(12): 1292-9.

Mombaerts, P. (2004). "Love at first smell--the 2004 Nobel Prize in Physiology or Medicine." N Engl J Med **351**(25): 2579-80.

Mombaerts, P., F. Wang, et al. (1996). "Visualizing an olfactory sensory map." Cell **87**(4): 675-86.

Moore, C. H., O. Pustovyy, et al. (2011). "Olfactory responses to explosives associated odorants are enhanced by zinc nanoparticles." Talanta **88**: 730-3.

Moore, T., L. Globa, et al. (2014). "Oral administration of Bacillus subtilis strain BSB3 can prevent heat stress-related adverse effects in rats." J Appl Microbiol **117**(5): 1463-71.

Morrison, E. E. and R. M. Costanzo (1989). "Scanning electron microscopic study of degeneration and regeneration in the olfactory epithelium after axotomy." J Neurocytol **18**(3): 393-405.

Morrison, E. E. and R. M. Costanzo (1990). "Morphology of the human olfactory epithelium." J Comp Neurol **297**(1): 1-13.

Mu, Q., G. Jiang, et al. (2014). "Chemical basis of interactions between engineered nanoparticles and biological systems." Chem Rev **114**(15): 7740-81.

Nache, V., J. Kusch, et al. (2008). "Thermodynamics of activation gating in olfactory-type cyclic nucleotide-gated (CNGA2) channels." Biophysical Journal **95**(6): 2750-2758.

Nache, V., J. Kusch, et al. (2008). "Thermodynamics of activation gating in olfactory-type cyclic nucleotide-gated (CNGA2) channels." Biophys J **95**(6): 2750-8.

Nagappan, P. G., S. Subramaniam, et al. (2017). "Olfaction as a soldier-- a review of the physiology and its present and future use in the military." Mil Med Res **4**: 9.

O'Malley, D. (2015). "Immunomodulation of enteric neural function in irritable bowel syndrome." World J Gastroenterol **21**(24): 7362-6.

Otsuka, H., Y. Nagasaki, et al. (2003). "PEGylated nanoparticles for biological and pharmaceutical applications." Adv Drug Deliv Rev **55**(3): 403-19.

Ottoson, D. (1955). "Analysis of the electrical activity of the olfactory epithelium." Acta Physiol Scand Suppl **35**(122): 1-83.

Paysan, J. and H. Breer (2001). "Molecular physiology of odor detection: current views." Pflugers Arch **441**(5): 579-86.

Pearce, J. A. (2015). "Improving Accuracy in Arrhenius Models of Cell Death: Adding a Temperature-Dependent Time Delay." J Biomech Eng **137**(12): 121006.

Perry, J. L., K. G. Reuter, et al. (2012). "PEGylated PRINT Nanoparticles: The Impact of PEG Density on Protein Binding, Macrophage Association, Biodistribution, and Pharmacokinetics." Nano letters **12**(10): 5304-5310.

Petra, A. I., S. Panagiotidou, et al. (2015). "Gut-Microbiota-Brain Axis and Its Effect on Neuropsychiatric Disorders With Suspected Immune Dysregulation." Clin Ther **37**(5): 984-95.

Pifferi, S., A. Boccaccio, et al. (2006). "Cyclic nucleotide-gated ion channels in sensory transduction." FEBS Letters **580**(12): 2853-2859.

Pontiggia, F., D. V. Pachov, et al. (2015). "Free energy landscape of activation in a signalling protein at atomic resolution." Nat Commun **6**: 7284.

Portman, K. L., J. Long, et al. (2014). "Enthalpy/Entropy Compensation Effects from Cavity Desolvation Underpin Broad Ligand Binding Selectivity for Rat Odorant Binding Protein 3." Biochemistry **53**(14): 2371-2379.

Reisert, J. and H. Zhao (2011). "Perspectives on: information and coding in mammalian sensory physiology: response kinetics of olfactory receptor neurons and the implications in olfactory coding." J Gen Physiol **138**(3): 303-10.

Ressler, K. J., S. L. Sullivan, et al. (1994). "Information coding in the olfactory system: evidence for a stereotyped and highly organized epitope map in the olfactory bulb." Cell **79**(7): 1245-55.

Restrepo, D., J. H. Teeter, et al. (1996). "Second messenger signaling in olfactory transduction." J Neurobiol **30**(1): 37-48.

Samoylov, A. M., T. I. Samoylova, et al. (2005). "Novel metal clusters isolated from blood are lethal to cancer cells." Cells Tissues Organs **179**(3): 115-24.

Sannaningannavar, F. M., B. S. Navati, et al. (2016). "Activation energy (ΔG*), enthalpy (ΔH*), and entropy (ΔS*) of poly(ethylene glycol) using Higasi method." Polymer Bulletin **73**(6): 1689-1700.

Schele, E., L. Grahnemo, et al. (2015). "Regulation of body fat mass by the gut microbiota: Possible mediation by the brain." Peptides **77**: 54-9.

Scott, J. W. and P. E. Scott-Johnson (2002). "The electroolfactogram: A review of its history and uses." Microscopy Research and Technique **58**(3): 152-160.

Scott, J. W. and P. E. Scott-Johnson (2002). "The electroolfactogram: a review of its history and uses." Microsc Res Tech **58**(3): 152-60.

Segel, I. (1975). Biochemical Calculations. New York, john Wiley & Sons.

Segel, I. H. (1976). Biochemical calculations. New-York, John Wiley & Sons.

Sharon, G., D. Segal, et al. (2010). "Commensal bacteria play a role in mating preference of Drosophila melanogaster." Proc Natl Acad Sci U S A **107**(46): 20051-6.

Shepard, B. D. and J. L. Pluznick (2016). "How does your kidney smell? Emerging roles for olfactory receptors in renal function." Pediatr Nephrol **31**(5): 715-23.

Shepherd, G. M. (1994). "Discrimination of molecular signals by the olfactory receptor neuron." Neuron **13**(4): 771-90.

Singletary, M., S. Hagerty, et al. (2017). "PEGylation of zinc nanoparticles amplifies their ability to enhance olfactory responses to odorant." PLoS One **12**(12): e0189273.

Smolne, S., S. Weber, et al. (2016). "Propagation and Termination Kinetics of Poly(Ethylene Glycol) Methyl Ether Methacrylate in Aqueous Solution." Macromolecular Chemistry and Physics **217**(21): 2391-2401.

Sorokulova, I., L. Globa, et al. (2016). "Prevention of Heat Stress Adverse Effects in Rats by Bacillus subtilis Strain." J Vis Exp(113).

Spehr, M., G. Gisselmann, et al. (2003). "Identification of a testicular odorant receptor mediating human sperm chemotaxis." Science **299**(5615): 2054-8.

Standifer, K. M., L. R. Murthy, et al. (1991). "Affinity labeling of mu and kappa receptors with naloxone benzoylhydrazone." Mol Pharmacol **39**(3): 290-8.

Staton, J. M., J. E. Dench, et al. (1995). "Expression and immune recognition of stress proteins in sarcoidosis and other chronic interstitial lung diseases." Immunol Cell Biol **73**(1): 23-32.

Suk, J. S., Q. Xu, et al. (2016). "PEGylation as a strategy for improving nanoparticle-based drug and gene delivery." Adv Drug Deliv Rev **99**(Pt A): 28-51.

Toffoli, C. A. and D. S. Rolfe (2006). "Challenges to military working dog management and care in the Kuwait theater of operation." Mil Med **171**(10): 1002-5.

Villanueva-Millan, M. J., P. Perez-Matute, et al. (2015). "Gut microbiota: a key player in health and disease. A review focused on obesity." J Physiol Biochem **71**(3): 509-25.

Viswaprakash, N., J. C. Dennis, et al. (2009). "Enhancement of Odorant-Induced Response in Olfactory Receptor Neurons by Zinc Nanoparticles." Chem. Senses **34**: 547-557.

Viswaprakash, N., J. C. Dennis, et al. (2009). "Enhancement of odorant-induced responses in olfactory receptor neurons by zinc nanoparticles." Chem Senses **34**(7): 547-57.

Viswaprakash, N., E. M. Josephson, et al. (2010). "Odorant response kinetics from cultured mouse olfactory epithelium at different ages in vitro." Cells Tissues Organs **192**(6): 361-73.

Vodyanoy, V. (2010). "Zinc nanoparticles interact with olfactory receptor neurons." Biometals **23**(6): 1097-103.

Wada-Katsumata, A., L. Zurek, et al. (2015). "Gut bacteria mediate aggregation in the German cockroach." Proc Natl Acad Sci U S A **112**(51): 15678-83.

Wu, C., Y. Jia, et al. (2015). "Activation of OR1A1 suppresses PPAR-gamma expression by inducing HES-1 in cultured hepatocytes." Int J Biochem Cell Biol **64**: 75-80.

Yang, N. J. and I. M. Chiu (2017). "Bacterial Signaling to the Nervous System through Toxins and Metabolites." J Mol Biol **429**(5): 587-605.

Yang, Y. D., H. Cho, et al. (2008). "TMEM16A confers receptor-activated calcium-dependent chloride conductance." Nature **455**(7217): 1210-5.

Yao, J., B. Liu, et al. (2010). "Kinetic and energetic analysis of thermally activated TRPV1 channels." Biophys J **99**(6): 1743-53.

Yokota, M., L. G. Berglund, et al. (2014). "Thermoregulatory modeling use and application in the military workforce." Appl Ergon **45**(3): 663-70.

Youngentob, S. L., F. L. Margolis, et al. (2001). "OMP gene deletion results in an alteration in odorant quality perception." Behav Neurosci **115**(3): 626-31.

Yu, J., P. Yin, et al. (2010). "Effect of heat stress on the porcine small intestine: a morphological and gene expression study." Comp Biochem Physiol A Mol Integr Physiol **156**(1): 119-28.

Zanello, L. P., E. Aztiria, et al. (1996). "Nicotinic acetylcholine receptor channels are influenced by the physical state of their membrane environment." Biophys J **70**(5): 2155-64.

Zufall, F., S. Firestein, et al. (1991). "Analysis of Single Cyclic-Nucleotide Gated Channels in Olfactory Receptor-Cells." J Neurosci **11**(11): 3573-3580.

Zufall, F., H. Hatt, et al. (1993). "Rapid application and removal of second messengers to cyclic nucleotide-gated channels from olfactory epithelium." Proc Natl Acad Sci U S A **90**(20): 9335-9.